12-2016

Selective Resistive Sintering: A Novel Additive Manufacturing Process

Austin Bryan Van Horn
University of Arkansas, Fayetteville

Citation
Van Horn, A. B. (2016). Selective Resistive Sintering: A Novel Additive Manufacturing Process. *Graduate Theses and Dissertations* Retrieved from https://scholarworks.uark.edu/etd/1971

Selective Resistive Sintering: A Novel Additive Manufacturing Process

A thesis submitted in partial fulfillment of the
requirements for the degree of
Master of Science in Mechanical Engineering

by

Austin Van Horn
University of Arkansas
Bachelor of Science in Mechanical Engineering, 2015

December 2016
University of Arkansas

This thesis is approved for recommendation to the Graduate Council

Dr. Wenchao Zhou
Thesis Director

Dr. Steve Tung
Committee Member

Dr. Uche Wejinya
Committee Member

ABSTRACT

Selective laser sintering (SLS) is one of the most popular 3D printing methods that uses a laser to pattern energy and selectively sinter powder particles to build 3D geometries. However, this printing method is plagued by slow printing speeds, high power consumption, difficulty to scale, and high overhead expense. In this research, a new 3D printing method is proposed to overcome these limitations of SLS. Instead of using a laser to pattern energy, this new method, termed selective resistive sintering (SRS), uses an array of microheaters to pattern heat for selectively sintering materials. Using microheaters offers significant power savings, significantly reduced overhead cost, and increased printing speed scalability. The objective of this thesis is to obtain a proof of concept of this new method. To achieve this objective, we first designed a microheater to operate at temperatures of 600^0C, with a thermal response time of ~1 ms, and even heat distribution. A packaging device with electrical interconnects was also designed, fabricated, and assembled with necessary electrical components. Finally, a z-stage was designed to control the airgap between the printhead and the powder particles. The whole system was tested using two different scenarios. Simulations were also conducted to determine the feasibility of the printing method. We were able to successfully operate the fabricated microheater array at a power consumption of 1.1W providing significant power savings over lasers. Experimental proof of concept was unsuccessful due to the lack of precise control of the experimental conditions, but simulation results suggested that selectivity sintering nanoparticles with the microheater array was a viable process.

Based on our current results that the microheater can be operated at ~1ms timescale to sinter powder particles, it is believed this new process can potentially be significantly quicker than selective laser sintering by increasing the number of microheater elements in the array. The low cost of a microheater array printhead will also make this new process affordable. This thesis presented a pioneering study on the feasibility of the proposed SRS process, which could potentially enable the development of a much more affordable and efficient alternative to SLS.

Keywords: 3-D printing, Resistive sintering, Microheater

ACKNOWLEDGEMENTS

This selective resistive sintering, research, project has been fostered along by the support of many individuals. To each one mentioned here, or not, I'm grateful to everyone who has provided support to accomplish this monumental task.

My advisor Dr. Wenchao Zhou deserves much recognition for my success. He has attributed motivation, valuable inputs to the work, and also seems to provide timely response no matter the hour of the day. Dr. Zhou has a real passion for providing meaningful research, specifically research that will have a large impact on industry. This impact he describes typically provides an overall beneficial societal impact. His general perspectives on making an impact have positively influenced me to go above and beyond what is necessary and always have a constant desire to continuously learn.

I'd also like to thank my thesis committee, Dr. Uche Wejinya, and Dr. Steve Tung. Both of these professors have contributed many efforts to help improve my research or provide the necessary knowledge to complete the task. In addition, their support and comments on my thesis have helped to better serve its purpose to educate people and document the significant impact of the work.

Many faculties of HiDEC at the University of Arkansas have contributed much help on this project in the fabrication of microheater, packaging, and learning to use their equipment. I would like to thank and recognize: Errol Porter, Dr. Simon Ang, Mike Glover, and Mike Stegger for all the help they've provided to make this project possible.

A special thanks goes to all of my lab mates in the AM^3 Lab. I'm certainly glad I didn't have to sit in a windowless room without anyone to converse with while we worked countless hours on

our research. We’ve shared lots of laughter, culture, and insane cuisine. I’ll never forget the meals I’ve had with you guys. I’d also like to thank all of them for opening up new ideas to me through their various fields of research and experiences. Each person had very unique experience and collectively helped our lab learn and think it ways we typically wouldn’t have.

A team of people has worked to help make this project happen. I would like to thank my Capstone Project team, Kendell Whitehead, Nick Segovia, and Mark Edwards for all of their help in designing 3D printing systems for future work in this project. I would also like to thank Mahsa Montazeri, a Ph.D. student in the AM^3 Lab, for helping out with the project and continuing the work of this project after I leave. Her knowledge of control systems, programming, and circuitry has made this project possible.

DEDICATION

I would like to personally thank all of those who have helped as more than just educational mentors while I've been pursuing this work in my Master's degree. It's been a long fun road to travel down, and we only hit a few bumps so thank you all for persevering with me along the journey. First, I would like to thank my family Jeffery, Cindy, and Seth Van Horn. They have provided an infinitesimal amount of love and support. They have given me opportunities that my gratitude could not express. I'd even like to thank them for their help in making revisions of this dissertation and the many other papers I've written. I would also like to acknowledge everyone in my lab. It has been fun hanging out with everyone there and I'll always remember the good food each person brought from their cultural backgrounds. Lastly, I would like to thank my advisor, Dr. Wenchao Zhou. He helped to push me all along the way during my graduate degree. You have a unique perspective on many things, and all your advice in life will always be remembered.

TABLE OF CONTENTS

LIST OF TABLES

LIST OF FIGURES

Chapter 1 INTRODUCTION

Manufacturing is a method in which raw materials are transformed into goods. Manufacturing methods generally fall into three categories: subtractive processes, deformative processes, or additive processes. Subtractive processes work by taking a bulk supply of some material, and then removing the undesired parts of the bulk piece of material. This has been seen in many of the standard machining processes such as etching, lathing, milling, grinding, sawing, and torch cutting,. Deformative processes are another very popular method of manufacturing, in which materials are deformed into shapes, such as forging, casting, or molding.

The third manufacturing method, additive manufacturing, is a quickly emerging technology for manufacturing. ASTM has defined the term for additive manufacturing (AM) as a group of technologies capable of combining materials to manufacture complex products in a single process [1].

Additive manufacturing is commonly known as 3D printing, which is becoming more popular in current manufacturing, due to its ability to almost form any shape desired, offering a wide range of customizable products without having to adjust the manufacturing method. It has been adopted for many applications but is still not considered a mainstream method of manufacturing due to its limitations in production cost for volume production. Many limitations, such as speed, cost, and product quality, have prolonged the development and widespread adoption of this technology.

Conformity to use additive manufacturing is being fostered by technological innovations such as the one developed in this research. The overall motivation is to be able to provide a “mass customization” of manufacturing, which means providing a manufacturing method where all the customization of 3D printing can be obtained with manufacturing speeds comparable to current mass production methods. This concept is not easily proven and must be taken in smaller more quantifiable steps towards the ultimate goal. For this reason, a new technology, selective resistive sintering (SRS), is investigated in this thesis. To introduce the new method of additive manufacturing, we will first provide background to similar technologies and their limitations, such as selective laser sintering (SLS), aerosol printing, and selective heat sintering.

1.1 Technologies and Limitations

In this section, an introduction to SLS and other similar technologies to the proposed SRS process will be discussed.

1.1.1 Selective Laser Sintering

SLS is a popular AM process that enables the creation of 3D objects by sintering powders together. A laser is used as the energy source, which selectively fuses the powder particles where the laser is applied to form a 3D structure. This process is shown in Figure 1.

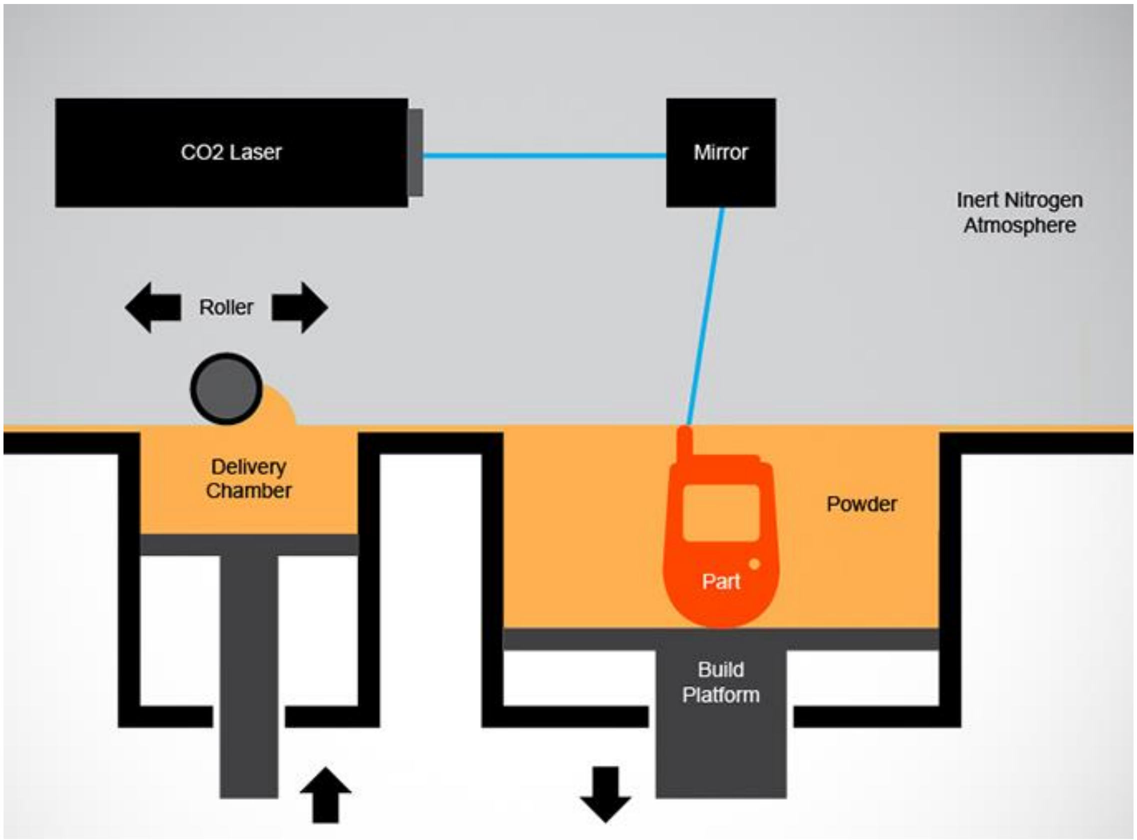

Figure 1-Schematic of How Selective Laser Sintering Works [2]

Additional layers can be successively added in order to build the geometry in the vertical direction, while the remaining non-sintered powders act as a support structure. In this method, the laser has high power consumption and resolution is limited by the laser size. This limits its scalability, and thus making the technology limited in speed and efficiency. For example, a commercially available SLS printer EOSINT P100, for printing polymers, uses 30 W which is standard for a low-temperature operation and has a build rate of 3.04cm^3/h [3]. Another example is the Optomec LENS 750 which uses a 1 kW powered Nd:YAG laser and can exceed temperatures of 2500^{0}C at a scanning speed of 16.9 mm/s [4]. This technology is advantageous due its ability to reach liquefying temperatures of most materials which enable it to create 3D structures out of a wide range of materials with relatively low porosity, but consumes a significant amount of power and has extremely slow build speeds.

1.1.2 Aerosol Printing

Another commercial additive manufacturing method is Aerosol printing. Aerosol printing is a maskless non-contact printing system from Optomec Inc. In this process, an aerosol is formed by pneumatic atomizing or ultrasonic. This aerosol then travels to the print head. In the print head, the material never touches the sides of the print head due to a flow of gas in the nozzle which focuses the aerosol. This lets the material easily transfer from the aerosol process to the head of the printer. This can be seen in Figure 2.

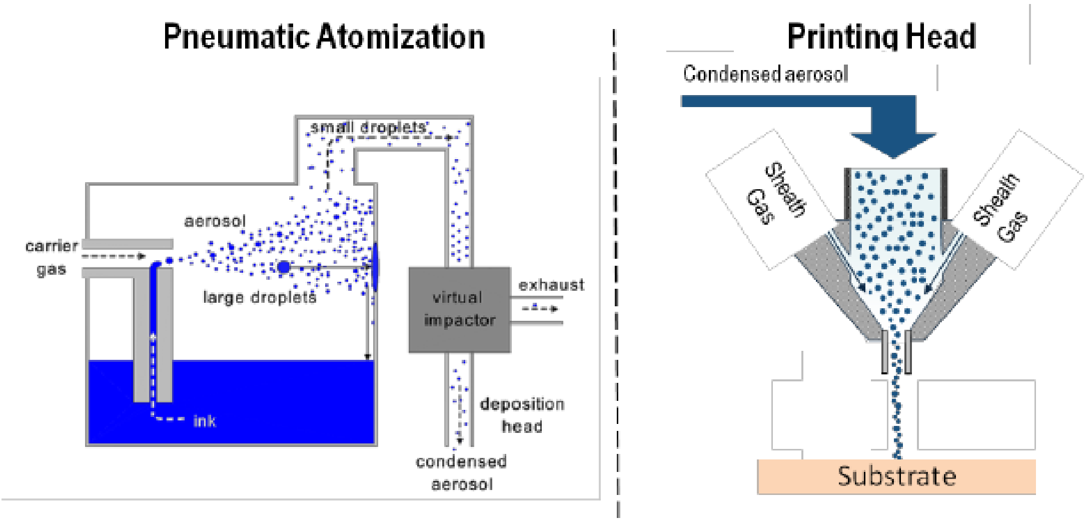

Figure 2-Diagram of How Aerosol Printing Works [5]

The material is then ejected by a nozzle. Due to the method of operation, parameters can easily be adjusted to change the resolution like the gas flow and nozzle size [6]. The highest resolution from these printers is ~1 µm, although the printing speed decreases at higher resolution [7]. The maximum speed in an aerosol printer is ~100 mm/s with resolution of 25 μm [8]. This technology is primarily focused on the development of electronic technology, low production electronics, and repairing electronics [8]. It does not operate at the speeds needed to be used as a mass production method. This process also requires post processing to sinter printed materials. Though this is a commercialized method of 3D printing it still lacks effectiveness due to the multiple steps involved in post processing the prints.

1.1.3 Selective Heat Sintering

Selective heat sintering is a method of 3D printing where resistive heating elements come into contact with particles to sinter them. It is most popularly defined by the commercially available Blueprinter. This printer depends on a powder deposition method to lay down layers, and then a heating element to move over the powders, bringing the heat source into contact with the powders. In this system, materials have to be previously heated to only a few degrees below their sintering temperature [3]. It offers build speeds at 2-3 mm/hr [9]. The build rate speed is competitive with other sintering methods, and the printer is one of the most cost-effective printers on the market. Currently, only one material is being printed by the printer. The influence from the actual heating source also has little impact, due to most of the heat being lost through the print head, due to a protective layer between the heater and material being sintered. For that reason, it is much more inefficient than it could be and the patterned heat can only contribute ~10ºC temperature change.

1.1.4 Summary

The previous section shows the current progress in additive manufacturing technologies. Aerosol printing, selective heat sintering, and SLS, are all well-known forms of 3D printing. These technologies are not typically effective for use in industry because their various complexities disable them from being a mass production method. For this reason, a new 3D printing method needs to be innovated which surpasses the current level of technology.

1.2 Problem Formulation

The SRS process proposed in this thesis is expected to have an increased manufacturing speed and an overall cost reduction allowing for widespread adoption by industries to use for mass production. Therefore, the goal of this thesis is to determine the viability of the proposed SRS process. This technology will be more narrowly focused to provide a sintering method that can selectively sinter a 100 μm area within 1 *ms*, and has lower energy consumption than other existing sintering technologies.

1.3 SRS Method

The proposed SRS method uses a MEMS microheater to transfer heat via conduction to a previously lain layer of material to be sintered. The first step in this method is to lay a layer of nano/micron particles or nano/micron-particle inks. The methodology requires repeating a new layer each time much like most selective sintering processes to create a true 3D structure. However, the goal in this thesis is to create only a 2D structure for a proof of concept. In the next steps lies the primary differences to distinguish this method from selective heat sintering and SLS. To sinter materials, a microheater moves over the top of the previously layer of nanoparticles and selectively sinters the area desired without making contact with the particles. This process is shown in Figure **3**. Here, the heater moves over the top, conducting heat through air to particles being sintered. The solid areas are sintered and the remaining spherical shapes are the unsintered particles leftover. These unsintered particles act as support structures.

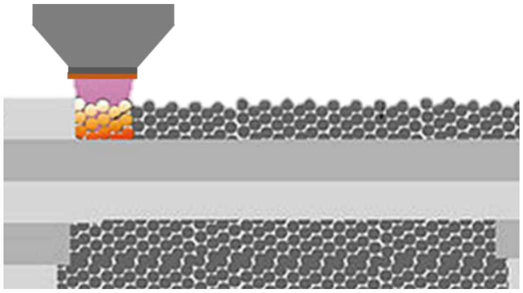

Figure 3-Overview of Selective Sintering Operation

1.4 Advantages over Existing Technology

Microheaters were chosen for this printer as the energy source. Microheaters offer a small area of heat application, low power consumption, low cost fabrication, fast thermal response times, and capability to operate at high temperatures in excess of 600ºC. Using microheaters that are small in size, offers high-resolution printing while also providing adequate heat to sinter the particles. Quick thermal response enables the ability to sinter materials.

Technologies for comparison in this research are all sintering based methods. This technology has the potential to outperform other technologies previously mentioned such as Optomec’s Aerosol printer, SLS, and selective heat sintering. SLS suffers from many issues in comparison to the newly proposed method: 1) consumes more power, 2) not a scalable technology, 3) slow build speeds. Aerosol printing is limited in speed and the fact that they require additional sintering steps to have a functional device. Aerosol printing is only a 2D printing process.

Selective heat sintering is a very similar process to the one proposed here. The printheads are very similar in that they use resistive heaters to provide sintering. Due to this similarity, both are extremely affordable methods of printing. The difference lies in the method of operation. SRS does not come into contact with the materials. In selective heat sintering, protective layers are used to protect the heaters from being damaged. This makes it inefficient compared to SRS. The temperature obtained in these printers is also drastically different. The operation of SRS provides a heat source which can sinter materials up to ~600°C, whereas SHS can only provide a few degrees difference in heat and never reaches a temperature above 140°C. Contact can possibly cause possible damage to the print and puts wear on the printer. Its speed is also limited by the way it prints.

The proposed SRS method, which rivals methods like selective laser sintering, have a technological advantage of being potentially at least 10x better in terms of speed and power consumption. Peter Theil describes this as the estimated general trend representing a true technological competitive advantage [10]. In this research, numerical simulations and experiments were performed to investigate the viability of this proposed method.

1.5 Potential Applications

SRS can be potentially used in variety of industry applications, overall transforming the use of 3D printing in industry. A particular field of application that this technology excels in is production of printable electronics. These electronics are formed by a single layer-technically 2D printing process, but it can create these custom 2D shapes at rapid speeds. The field of radio frequency identification (RFID) technology shows a promising future in using this method of production with limited application with this process being both fast and cost efficient. This technology could potentially lower the production cost to a range that is competitive with the current bar coding method now utilized. Wide consumer use is also viable due to the low cost of this technology. The system has the capability to be entirely digitalized to make it user friendly while still being powerful enough to create a user's designs. Since all the power is essentially contained within a computer system, this makes it user-friendly for customers. The MEMS microheaters are also relatively safe due to the small amount of heat being produced. Nanoparticle solutions such as the popularly used NovaCentrix paste are also relatively safe compared to non-diluted particles. This prevents hazardous nanoparticles from becoming airborne. A combination of an efficient cleaning system with this technology could make this printing method widely available to the "Average Joe" buyer with interested in another cool toy to add to his/her garage.

1.6 Outline of Thesis

Chapter 2 is a literature review of microheater technology, fabrication, packaging, calibration, and high precision control systems that are important for the SRS technology. In the review of the literature, microheaters are first reviewed for different design aspects. Microheaters were evaluated for many different design aspects such as materials, shapes, and operational parameters. Fabrication was evaluated for its aspects on the overall operation as well as contributions to design factors. To ensure the functionality of the heater for our intended uses, different packaging design was evaluated along with calibration. Many different calibration methods were assessed to help define parameters for control systems as well as numerical models. Lastly, high precision control systems were reviewed. During the modeling of the microheater for the purposes of SRS, it was found that high precision control was needed to achieve the desired heat transfer for sintering. These systems were reviewed for their actuation methods, sensors, and overall control systems.

Chapter 3 consist of the design, optimization, fabrication, and packaging of the microheater. Multiple different designs are evaluated and optimized using a constrained particle swarm optimization algorithm for the geometry of the microheater. This device must then be fabricated. Fabrication of the microheater is based on methods that are well-known and established at the University of Arkansas HiDEC. The packaging of the MEMS microheater device is a critical design for this implementation of SRS and is detailed as to the specifications required for the new printing method.

In chapter 4, the SRS process is evaluated. The validated numerical models used previously in the design of the microheater are used to validate that this method is, in fact, feasible. Different material properties and their sintering temperatures are provided to show the viability of the materials reaching a sufficient temperature to be sintered. It also defines other aspects of the operation such as the selectivity of the print, material parameters, power supply required, and special requirements between the heater and the materials to be sintered.

Chapter 5 is the design of a microheater based on the operation of the SRS system. Though many papers have been written on MEMS microheater design, none have been designed for conducting heat through a medium. In this chapter, the design of the geometry of the resistive heating element was kept from chapter 3. The remaining design aspects of the heater were changed along with operational parameters. This new design for the heater led to a power reduction of 2x. The parameters of operation for this heater were laid out so that the airgap between the heater and materials being sintering were defined, the power of the heater, and duration of the power supply to the heater. In the final remarks of this chapter, fabrication was laid out for this method to be completed by equipment available at HiDEC.

In chapter 6, the foundation for future work is laid out. This technology is far from being a mature product ready for commercialization. It is the groundwork of a new method of printing through which only validity of the process was proven. This work will spark many various projects to make the operating conditions more optimal based on a variety of operating scenarios. Such recommendations for future work will include. Optimization of microheater design by use of anonymous geometries, material optimization, redefining modeling to tune control parameters, and an overall more complex digitalization of the system for wide consumer use. Then this chapter is followed by concluding remarks.

Chapter 2 LITERATURE REVIEW

In this chapter, a literature review is provided of technology and research that aids in the design and fabrication of microheaters and micropositioning systems as well as sintering behavior. These were identified as the critical aspects of providing a proof of concept for the SRS system. Now that a background has been provided on the overall technology, literature will be reviewed to identify the technological limits of the technology being used in this SRS design. The components of this system are the microheater device, packaging, electrical interconnects, micro positioning actuators, micro positioning sensors, and sintering behavior. These subjects will be individually discussed in detail below. Definitions critical to understanding the technology are first established so readers are not lost. The definitions are provided below:

Microheater: A microelectromechanical system (MEMS) that emits heat from Joule heating. These devices to be considered microheaters have a dimension of 1 mm or smaller.

Packaging: A group of things that are boxed and offered as a unit. In MEMS they contain electrical and mechanical components [11]. In the context of this paper, packaging is the device which encloses and protects a MEMS die. It also provides the necessary environment needed for the MEMS device and provides electrical connection to the device.

High Precision Linear Control System: Precision systems are such that can be generally defined by manufacturing to tolerances which are better than one part in 10^5 [12]. Typically this system has a resolution of a few hundred nanometers to multiple microns.

Sintering: A diffusion process through which material boundaries are combined [13].

2.1 Microheater Design

The microheater plays a critical role in SRS. In this section, the state of the art microheater technology is assessed to determine the research gap for basis in the SRS design. Many different aspects of microheater design have been previously studied in literature. Geometry is a critical aspect of the design that has significant impact on the operation, power consumption, and heat transfer of a microheater. Materials are another critical aspect that plays a significant role in microheater design. Common design objectives for microheaters are the need for even heat distribution and minimizing stresses in suspended membranes. Other design considerations include power consumption, ease of fabrication, chemical stability, etc.

2.1.1 History

James Prescott Joule initiated the first research conducted in resistive heating in 1841 which was later followed by Hienrich Lenz in 1842. However, this method of heating was not accepted by the Royal Society in London until 1849 when Michael Farraday sponsored the findings, which soon after led to James Joule's acceptance in the Royal Society [14]. Since then resistive heating has miniaturized into a technology known as MEMS microheaters, and this technology has gained a wide range of applications. Among the many applications includes various sensors, micro ignition of micro-propulsion systems, micro-explosive boiling, and inkjet printing [15, 16]. Their first debut in printing came in 1984 with the invention of HP's dot matrix printer which revolutionized inkjet printing technology [17]. This printer uses a microheater to vaporize the liquid inks and create vapor bubbles which supplies sufficient pressure to push liquid out a nozzle. HP's new dot-matrix printer miniaturized inkjet technology with higher quality, lower power, and quieter operation [17]. The dot matrix was only the first application into printing technology. Currently, they are being utilized for multiple printing technologies such as inkjet [18], selective heat sintering [3], and thermal printing commonly used in a Point-of-Sale (POS) printer [19]. In the later printing versions, these technologies have evolved from the 2D printing in the dot matrix, to the 3D aspects of ink jetting and SHS.

2.1.2 Materials

Typical microheaters consist of four main elements [20]: 1.) substrate, 2.) conductive leads, 3.) resistive heating element, 4.) dielectric layers. Many materials have been researched in literature for the four components used in a typical microheater configuration shown in Figure 4.

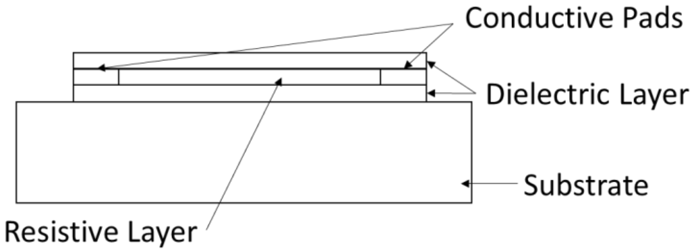

Figure 4-Microheater Configuration Showing 4 Main Components

However, the final design of these devices is ultimately determined by the parameters and objectives trying to be reached with a particular design. Of these components, only materials that can withstand ~600^{0}C are mentioned.

2.1.2.1 Substrate

The substrate provides the foundation for the microheater. Typical materials used are glass [16], silicon [21], ceramics [22], and stainless steel [23]. Silicon and ceramics typically can handle higher ranges of temperatures than steel and glass. Ceramics like alumina typically have a high thermal conductivity creating high power consumption as compared to Low-Temperature Co-fired Ceramics (LTCC) and glass [23]. LTCC is a composite ceramic/glass material typically offering much lower thermal conductivity enabling power savings [22]. Stainless steel has higher thermal conductivity but is often chosen because it is inert, robust, and has many well-defined microfabrication techniques [23]. Silicon is a frequently chosen material used for substrates due to its ability to operate at 1000ºC temperatures for prolonged periods of time and high thermal conductivity enabling quick thermal response times [21]. The high thermal conductivity, however, typically makes the heaters extremely power inefficient. Stainless steel is a conductor, making it a poor candidate for implementations where electronics need to be placed directly on top of the substrate without further manufacturing processes. A table of common materials and their properties is reviewed below in Table 1.

Table 1-Common Substrate Materials and the Properties for Microheaters

	Stainless Steel (Type 304)	Alumina	Silicon	Silicon Carbide	Pyrex-7740	LTCC (DuPont 951)
References	[24]	[22]	[25]	[25, 26]	[16]	[27]
Electrical Resistivity (ohm*m) @ 20°C	7.20E-02	>10E+18	dopant dependent	dopant dependent	1.26E+06	> 10E+12
Thermal Expansion Coefficient (1/K)	1.73E-05	6.50E-06	2.60E-06	4.00E-06	8.60E-06	5.8
Thermal Conductivity (W/m*K)	16.2	25	1.30E+02	120	1.18	3.3
Specific Heat (J/kg*K)	500	800	129	750	753.12	-
Density (kg/m^3)	8000	3780	2329	3100	2230	3100
Young's Modulus (Pa)	1.93E+11	4.00E+11	1.50E+11	4.10E+11	1.16E+11	1.20E+11
Melting Point (^{0}C)	1.40E+03	-	1.41E+03	2.73E+03	~550	-
Poisson's ratio (1)	0.29	1	0.27	0.14	0.321	0.24
Purpose	Substrate	Substrate	Substrate	Substrate	Substrate	Substrate

2.1.2.2 Resistive Material

The resistive layer is where the main source of resistive heating occurs. Resistive materials that can operate at temperatures above 600°C are needed for high-temperature microheaters. Some of the studied materials include Platinum (Pt) [22, 28, 29], Titanium (Ti) [16], Titanium Nitride (TiN) [16], SnO_2:Sb (Sb-doped in SnO_2) [21], Si:B [23], Si:P [23], Tungsten [30], and Molybdenum [31, 32]. The maximum operating temperatures of Pt and Ti/TiN are 600°C [23] and 700°C [16, 20]. Another consideration for choosing materials is the linearity of resistivity dependence on temperature. Pt has a fairly linear resistivity with respect to temperature while

Ti/TiN is generally non-linear [16, 20]. SnO_2:Sb and poly-silicon materials have temperature limits up to 1000°C, but require high voltage input due to their high resistivity, which is also non-linear with respect to temperature [21]. Tungsten has a high-temperature operation range of 1200°C, however, tungsten is only stable in an oxygen-enriched environment up to 400°C [23]. Molybdenum like Tungsten suffers significant oxidation at temperatures of 300°C, which becomes volatile at 700°C, but has capabilities of reaching temperatures of 850°C in a shielded environment [32]. The general rule of thumb, for which a material's grain boundaries start to diffuse, or agglomerate, is around one-third of its melting temperature [20]. This gives an approximation of what the operating temperatures of thin-film material will be. Experimental results of the operating temperatures for different materials are listed in Table 2. Agglomeration is the main failure method of Pt thin-film heaters. However, in materials like Ti, the main failure method is due to shear stress causing delamination from the substrate [16, 20]. Some material properties in the resistive layer also change with geometry, but the impacts of geometry on resistivity have been shown to be minimal within thin films [33, 34]. Sondheimer theory states that the change in the thickness of the material results in a minimal difference in material properties unless the material thickness is less than 8% of its mean-free-path for thin-film metals [35]. This has also been demonstrated experimentally [36]. Experiments have been performed to determine the values of resistive material properties at different temperatures [16]. Resistivity is a material property of particular importance due to its critical role in Joule heating. Materials have a tendency to increase resistivity as temperature increases [37]. This is associated with the temperature coefficient of resistance.

Table 2-Resistive Heater Material Properties

Thin-Film Resistor Material Properties

Material	Platinum	TiN	Titanium	SnO2:Sb	Tungsten	Molybdenum	Si:B/Si:P
Reference	[25, 38]	[20, 39]	[16, 40]	[21, 41]	[30, 42, 43]	[32, 44]	[23]
Resistivity (ohm*m) @ 20°C	1.06E-07	5.70E-07	1.54E-06	10-4E-5	5.60E-08	1.6E-7-6E-8	5.00E-05
Conductivity (W/m*K)	6.91E+01	2.38E+01	5.94E+00	-	1.77E+02	1.38E+02	1.30E+02
Temperature Coefficient α per °C	3.93E-03	1.40E-03	non-linear	non-linear	2.05E-03	2.31E-03	1.20E-03
Melting Temp. (°C)	1.77E+03	2.95E+03	3.42E+03	1.63E+03	3.41E+03	2.69E+03	-
Specific Heat (J/kg*K)		-	1.29E+02	-	1.40E+02	-	129
Thermal Expansion (1/K)	9.10E-06	-	8.60E-06	-	4.30E-06	5.35E-06	2.60E-06
Max Temp. (^{0}C)	6.00E+02	7.00E+02	7.00E+02	9.50E+02	>1000	1.00E+03	>800
Density (kg/m^3)		5.43E+03	4.51E+03	6.95E+03	1.93E+04	1.03E+04	2329
Young's Modulus (Pa)	1.68E+11	6.00E+11	1.14E+11	-	4.11E+11	3.30E+11	1.50E+11
Poison's Ratio	3.80E-01	2.50E-01	3.42E-01	-	2.84E-01	3.80E-01	2.70E-01
Stable	Yes	Yes	Yes	Yes	No	No	Yes

2.1.2.3 Adhesive Layers

Another material, not shown in the typical configuration, is adhesive materials. Use of adhesives to bond resistors to substrates or oxidative layers is a common practice. In Figure 5 the typical configuration of a MEMS microheater from Figure 4 is shown with the added adhesive layer in yellow.

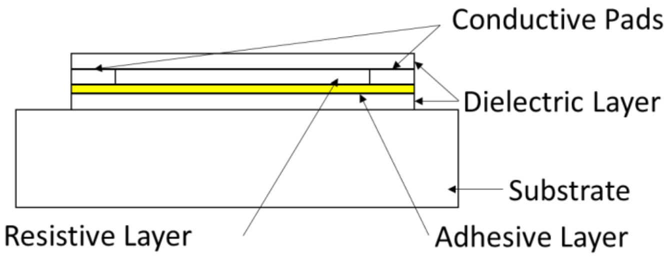

Figure 5-Typical Schematic of a Microheater Showing the Adhesive Layer

Adhesive forces play a critical role in MEMS, or microscopic bodies. These forces are known as Casimir forces and is associated with van der Waals forces, due to interactions of dipoles. The Tabor number is a dimensionless co-efficient which includes the surface roughness as a parameter in the calculation determining the adhesive force between surfaces in contact. Common calculations of this adhesion force can be calculated by the Tabor number using the equivalent radius between molecules and their surface energies of the molecules [45].

Typical adhesion materials include Ti, Ta, and Zr [28]. However, at temperatures above 700°C, Ti normally will suffer from adhesion issues, failing due to the high shear stresses, or oxidation causing the materials to peel off from the resistor or the substrate [46]. Ti adhesion layers also will cause an increase in resistance due to oxidation at high temperatures [23, 47]. A better adhesion material would be Ta or Zr. They are able to maintain their electrical properties and oxidation is not as prevalent in these materials [23, 47]. Zr and Ta can minimize interlayer diffusion which is another cause of failure to heaters [23, 47]. Zr and Ta are also low-stress options as compared to Ti, which is a predominantly a result of their lower Young’s modulus [23, 45]. However, Ti is the most commonly used material because it is abundant in supply. To combat high-stress issues from the commonly used Ti, the effects of stress can be minimized by using intermediate layers such as Silicon Nitride so that the thermal stress between layers isn’t as substantial [48].

2.1.2.4 Dielectric Layers

Dielectric layers can be used for structural integrity [49], thermal insulation [50], electrical insulation [51], and most commonly a sacrificial layer [52]. Often times, in microheater applications, these dielectric layers will be suspended. This exposes the layers to air and enables the layers to utilize the excellent insulating properties of air in the design.[49]. These materials, in MEMS fabrication, are typically formed through oxidation or a form of chemical vapor deposition [53, 54].

Materials used for dielectric layers are SiO_2, Si_3N_4, TiO_2, and Al_2O_3 [23]. All these materials have been known to cause high stresses in microheaters [55]. High stresses in dielectric layers can cause early failure of devices. These stresses are intrinsic stresses typically formed during fabrication, and they can vary based on the method used for fabrication. Fabrication methods can also create a large variance in material properties. TiO_2 and Al_2O_3 do not have as well-defined fabrication processes, standards, or definition of properties, but have shown oxidation growth rates of 1 *nm/s* and intrinsic stress of 200-400 MPa [56]. This is comparable to SiO_2 and Si3N4 making it as ideal as other materials, but lacking the fabrication capabilities in typical manufacturing facilities [56].

Of all these materials SiO_2 and $Si3N_4$ are the most commonly used in microheaters [20, 32, 49, 50, 53]. PECVD Si_3N_4 intrinsic stresses range from -300 MPa to 850 MPa, and PECVD SiO_2 are typical between -50 to -400MPa depending on the temperature and pressure of the process [55, 57]. A similar higher quality oxide fabrication method is LPCVD. It has also been shown in LPCVD Si_3N_4 the thermal conductivity can vary from 8 W/m*K to 25 W/m*K [48, 58], whereas SiO_2 generally, has a thermal conductivity of 1.4 W/m*K independent of other factors [59]. Typically, the material properties follow a trend that SiO2 has lower thermal conductivity than Si3N4. By comparing the same materials and their properties with different fabrication techniques, dielectric layers made by PECVD typically has a higher quality when compared to that made by LPCVD. Additionally, thermal oxidation of PECVD films is lower than LPCVD films due to the lower porosity and intrinsic stresses [53]. A review of the most commonly used material properties of materials in microheaters are listed in Table 3 and Table 4.

Table 3-Silicon Dioxide Material Properties

SiO2			
	PECVD	LPCVD	Thermal Oxidation
Thermal Conductivity (W/m*K)	1.4	.95	1.1 to 1.4
Intrinsic Stress (Mpa)	-450	210 to 420	-
Density (kg/m^3)	2.3	2.16	2.18 to 2.27
Specific Heat (J/kg)	730	730	1
Poison ratio	.25	.17	.17
Deposition Temperature (degC)	300	700 to 800	920 to 1100
Thermal Expansion (10E-6C^-1)	.5	.5	.56
Young's Modulus (Gpa)	85	46 to 75	66
Dielectric Constant	5	3.9 to 4.5	3. to 3.9
Source	[58, 60]	[61]	[62, 63]

Table 4-Silicon Nitride Material Properties

Si3N4		
	PECVD	LPCVD
Thermal Conductivity (W/m*K)	1.18 to 4.5	8 to 25
Intrinsic Stress (Mpa)	600 to 1200	-200 to 2000
Density (g/cm^3)	2.22	2.3-3.1
Specific Heat (J/kg*K)	700	700
Poison ratio	.25	.25
Deposition Temperature (degC)	300	700 to 800
Thermal Expansion (10E-6C^-1)	-	1.5
Young's Modulus (Gpa)	85 to 210	260 to 330
Dielectric Constant	6 to 9	6 to 7
Source	[53]	[48, 53, 58]

2.1.3 Design and Modeling Factors

Microheaters have many other design and modeling factors that affect the operations of the devices. These factors include geometry, calibration/characterization of material properties, thermal response, heat distribution, etc., which play critical roles in the functionality and accurate prediction of the microheater operation.

Experiments have been performed to evaluate the effects of heat transfer on microheaters. Microheaters are affected by three types of heat transfer which are conduction, convection, and radiation [64]. It was shown that the effects of conduction and convection can have a significant impact on the heat transfer while radiation is negligible for Ti and Pt materials at temperatures of less than ~700°C [16, 29, 64]. Heat transfer has been assessed experimentally and used extensively in modeling. Modeling has been used to select materials by evaluating the maximum temperature and power savings of microheaters with different insulating layers [22].

Geometry is another critical factor of a microheater. The thickness of dielectric layers was optimized for heat uniformity showing results with much-improved uniformity [65]. The dielectric thickness has been studied alongside different material fabrication techniques to evaluate the yield stresses of suspended membranes [48]. Suspended membranes also can offer reduced power consumption [48, 49]. Various geometries were assessed by S.M. Lee et al. as shown in Figure 6 [34]. The drive wheel design was found to be the optimal design for saving power.

Figure 6-Microheater Shapes for Comparison by S.M. Lee [34]

Another study used a spiral pattern, and the effects of heat transfer by varying geometric parameters such as the filament width and spacing between the filaments to find an optimal spiral pattern [59]. It showed that power savings could be achieved by using a double spiral, s-shape, and fan-shaped designs. This work was later optimized to enhance the double spiral design even further for heat uniformity.

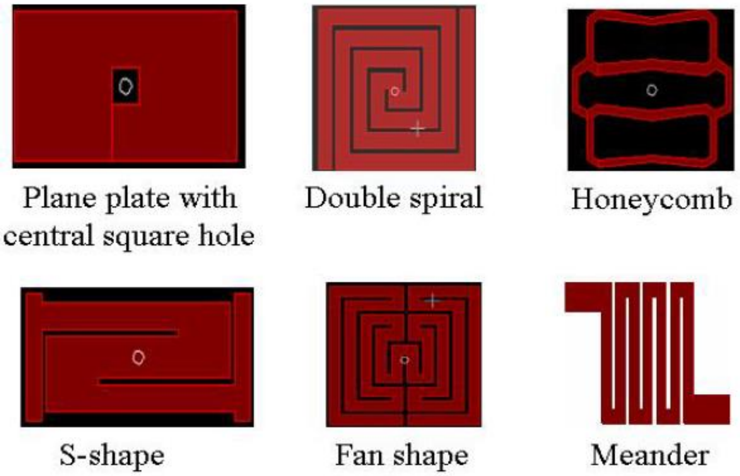

Figure 7-Shapes for Comparison and Optimization by Inderjit and Mohan [59]

In another study by L. Sujatha et al. [66], COMSOL was used to find optimal designs by creating random geometries. The optimal design for heat uniformity in this work was the square design with randomly subtracted squares to ensure the heat uniformity.

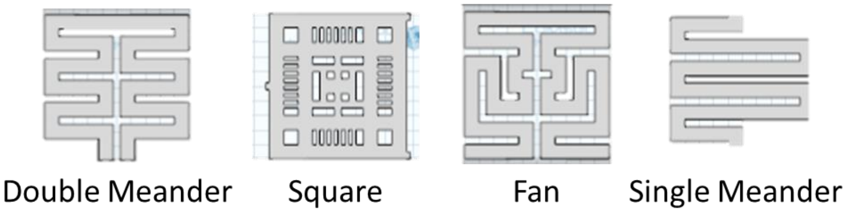

Figure 8-Shapes for Comparison and Optimization by Comsol [66]

The objective often achieved by heater geometry of having even heat distribution has been shown to have many corresponding affects. Even heat distribution often strongly correlates to providing power savings by being more efficient and also creates better responses times in microheaters [34]. The membrane to heater ratio, MHR, is an important parameter to creating a power efficient design as well preventing early failure from stresses [67]. Membrane heater ratio is the area of the suspended membrane relative to the area of the heating element. If this ratio is not balanced, this imbalance can lead to premature failure from yield stresses. [68, 69].

An overall accumulation of different factors including materials, geometry, and power supply have been used to increase the thermal response time of microheaters. The thermal response time serves to be a critical aspect of the operation of the heater, particularly in the SRS printer application. In previous studies, thermal response time reached 2ms for high-temperature designs of 600°C for Tungsten microheaters with low power consumption of 12mW [30]. A time response of 1 ms was achieved in a Pt/Ti heater reaching a temperature of 400°C using only 9mW of power [70].

There are many different design aspects that have been investigated and optimized in microheater technology. Some of the main focal points evaluated in literature are the heat transfer aspects, geometry, and thermal response time. The results of the design optimization varies in its effective heat transfer based on application and material. Therein lies the difficulty of multi-objective design for a complex mechanism such as the MEMS microheater.

2.2 Microheater Fabrication

Microheaters are typically fabricated through a combination of surface and bulk fabrication methods. These processes have been well established in IC and CMOS fabrication processes for most modern computing electronic systems [71]. These methods of fabrication will be discussed in 4 broad fabrication areas which are: etching, deposition, assembly, and photolithography. Each section will offer a review of specific processes commonly used in microheater fabrication and their impacts on design. In considering design for MEMS microheaters devices, two main considerations are given to fabrication. One is the feasibility of fabrication and the other is the impact of different fabrication methods on the design. As stated in section 2.1.2, fabrication method can have a significant impact on the properties of the materials. Figure 9 shows a simplified fabrication process flow utilizing the 4 broad categorizations of fabrication methods on a silicon substrate using silicon-based manufacturing methods. Silicon is used as the example due to it being the most commonly used substrate for MEMS microheaters [21, 34, 49, 59, 72].

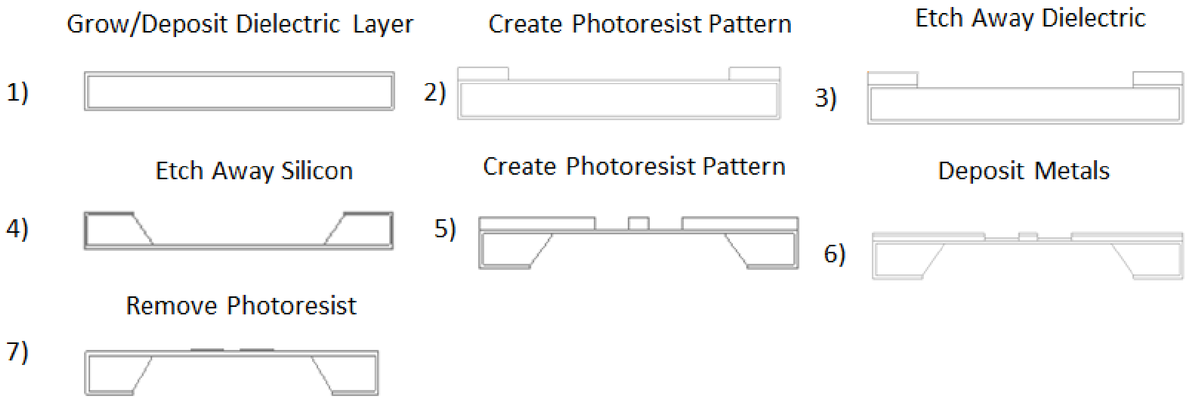

Figure 9-Typical Simplified Fabrication Process Flow for a MEMS Microheater

The assembly is a large part in the process of fabrication, but discussion regarding this topic is reserved for the packaging and electrical connections sections.

2.2.1 Etching

Etching is a process that removes material by physical or chemical means, which typically falls into the category of dry etching or wet etching. Etching is very commonly used in MEMS microheater fabrication. Figure 9 shows two different uses of etching for MEMS microheaters. One method is for creating a sacrificial mask. In the first etching process step (3), a dielectric layer was removed within the photoresist pattern by dry etching. This leaves a pattern for the next sequential process. This patterned dielectric mask enables the remaining parts of the silicon wafer to be protected from etching in the following step. In the following process, a wet etch is performed with a KOH or TMAH solution, which enables an angle of 54.7º to be formed in silicon. The etch process is most commonly performed by etching along the <111> in an (100) oriented wafer as shown in Figure 10. This is common in microheaters. It plays a critical role in the design to isolate the heating device from the silicon. The isolation enables air to act as an insulator. This saves much power as compared to being adjacent to silicon which has a thermal conductivity of ~130 W/m*K [73].

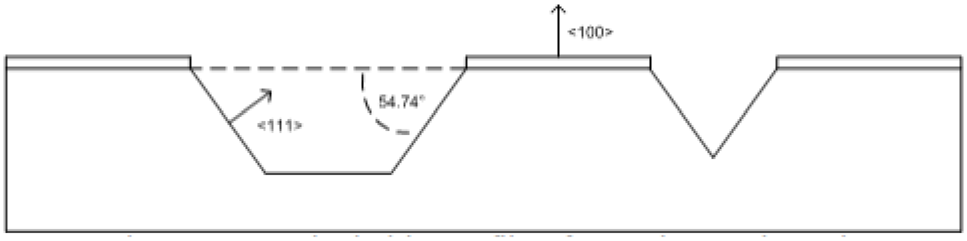

Figure 10-KOH and TMAH Etching of (100) Silicon Wafers [74, 75]

2.2.2 Deposition

Deposition processes in MEMS are additive processes that typically occur in one of the forms: Physical Vapor Deposition (PVD), Chemical Vapor Deposition (CVD), Thermal Oxidation, or

Plating. Evaporation, a PVD process, is commonly used in microheater fabrication, is typically performed by either, electron beam evaporation or thermal evaporation. The main purposes of deposition in microheaters, as seen in Figure 9, is primarily to create the initial dielectric layer or to create a metallization. Dielectric layers are formed through thermal oxidation or some form of CVD. In microheaters, these materials act as electrical insulators, structural support, and masking materials. LPCVD silicon nitride is often desired as the initial foundation layers because it can offer protection to silicon from commonly used etching processes like KOH. This is due to the selectivity of KOH to silicon and silicon dioxide over silicon nitride. It also offers tunable stresses to prevent early stress failures [49]. Microheaters use this fabrication method to promote desired heat transfer properties and create protective layers from oxidation [65]. Due to the low operational temperatures, layers can be deposited on top of metallizations that will agglomerate at low temperatures. Depending on their use, different methods may be desired for each method. Metallization is typically created by a form of physical vapor deposition. Electron beam (E-beam) evaporation is the most commonly used method in microheaters [16, 34]. E-beam evaporation uses large voltages from 20-30kV to form an electron gun which evaporates metals by accelerating electrons into a crucible containing the materials to be evaporated. This process can take place with wafer temperatures as low as 200^0C. Due to the low-temperature operation, polymers, like photoresist, can be used during the fabrication process. This makes it favored in microheater fabrication due to ease of patterning microheater resistive elements and conductive pads.

2.2.3 Photolithography

Photolithography is a critical process in all of MEMS manufacturing. This is the primary method used for creating patterns on devices and is also the main workhorse in the industry and creating any pattern of microheaters. Microheater resolution, or the smallest feature possible, for this process using proximity and contact methods is 2-3 µm [76]. Photolithography resolution can also be improved by using projection photolithography. This is the process where unique lenses and excimer lasers are used to focus light creating resolutions down to 37 nm [77]. Other specific photolithography methods popular in microheater fabrication, are image reversal techniques and hard baking.

An important part of photoresist patterning is the removal process after successive deposition or etching methods. There are many methods in which this material can be removed. The most popular method is by placing the wafer with photoresist into a solution which will dissolve polymers. Examples of these solutions are acetone, PRS 1000, acetone, and piranha. Lift-off is a wet process commonly used in microheater patterning after metal materials are E-beam evaporated into patterned areas. This is favorable due to the easy of patterning without having to use specific etchants or masking materials to create a pattern in the resistive element or conductive leads of a microheater [34]. A substitute to wet removal is a dry method called, ashing. Ashing is quicker than wet methods and typically is non-invasive to other materials making it usable for a wide range of materials. The critical aspect that makes this method favorable is the ability to avoid stiction issues where surface tension forces can pull small features together.

2.2.4 Summary of Fabrication with Example and Rationale

Fabrication techniques play a very crucial role in microheater fabrication. A standard fabrication process flow for a microheater based on the design and fabrication issues mentioned above is shown in Figure 11.

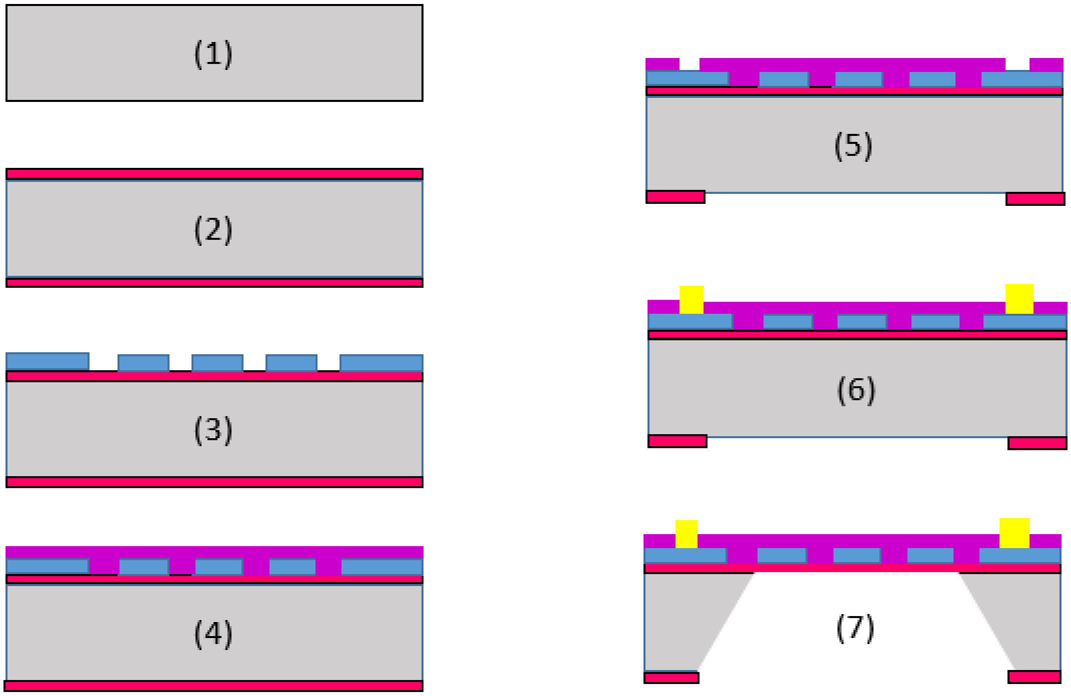

Figure 11. (1) Silicon (100) (2) Silicon dioxide deposited on substrate using LPCVD (3) Metal resistive heater is electron beam evaporated on (4) Second layer of silicon nitride is deposited by PECVD (5) Openings are etched away using hot phosphoric acid (6) RIE of LPCVD silicon nitride (7) Backside is etched away using TMAH

Much rationale has been provided for this type of process flow. The initial layer, as shown deposited in step (2) of Figure 11, is an electrically insulating layer that protects the semi-conductive silicon from coming into contact with metallization. It is also was used as the main structural member in microheaters, and to form a mask for the final etch in Step (7). The suspended membrane is a common design used to separate the high thermally conductive silicon, from the heater to enable greater thermal efficiency. Often materials of LPCVD silicon nitride are used so that the intrinsic stress levels can be tuned in this suspended layer. The higher quality of materials used in LPCVD allows for higher reliability as compared to PECVD materials. Step (3) is a metallization. This is typically done by electron beam evaporation which easily forms patterns by photolithography and lift-off. Step (4) of the fabrication process entails deposition of another dielectric layer. This layer serves many purposes. This layer adds protection to help prevent oxidation of the resistive material, and it also provides thermal insulation. This layer is PECVD silicon nitride. It is necessary to have this layer as a protective layer, to insulate the heater to create power savings, and for protection during the final etch. Silicon nitride as compared to silicon dioxide offers higher conductivity, creating more even heat distribution. PECVD has higher stress and oxidation than LPCVD but is not typically used due to the temperatures during the fabrication exceeding the eutectic temperatures of the metals and causing agglomeration. Step (5) is a hot phosphoric acid wet etch of silicon nitride. This is done to make openings for the conductive leads to contact the resistive element and for the pattern on the backside for the TMAH etch. Step (6) is another metallization. Again, the electron beam is chosen due to the ease of patterning with photolithography and lift-off. Then the final process, Step (7), is a backside TMAH etch. This etch provides an opening isolating the heater. This isolation creates power savings by preventing the heat from escaping through the highly thermally conductive silicon substrate. This similar process and rationale can be found in S. M. Lee et al., Velmathi et al., and sources [34, 59].

2.3 Microheater Packaging and Electrical Connections

Many common engineering practices in packaging design and electronic connection can be found in literature. Generally speaking, the design of these devices entails: protection from harsh environments, provides an electrical communication with other parts of the circuit, facilitates thermal dissipation, and imparts mechanical strength to the die. No printed standards for these devices were found in the literature. Packaging and electrical connections are closely coupled with the device itself and how it operates. For this reason, multiple different packaging devices may be required for the exact same die, making this part of the technology very hard to standardize. Packaging is complex and often more costly than the chip that it encompasses. Packaging and interconnects can cost from 40%-90% of the entire device [63]. Most of the unique applications and packaging of the devices are being utilized in an industry where the details of how to fabricate these devices are buried within proprietary details companies won't disclose [78, 79]. It often contains complex circuitry, mechanical design, and fabrication techniques.

2.3.1 Packaging

Packaging is a container for a MEMS device. This packaging is designed around the MEMS device to ensure the MEMS operates correctly. This configuration for a microheater can be seen in Figure 12 [80].

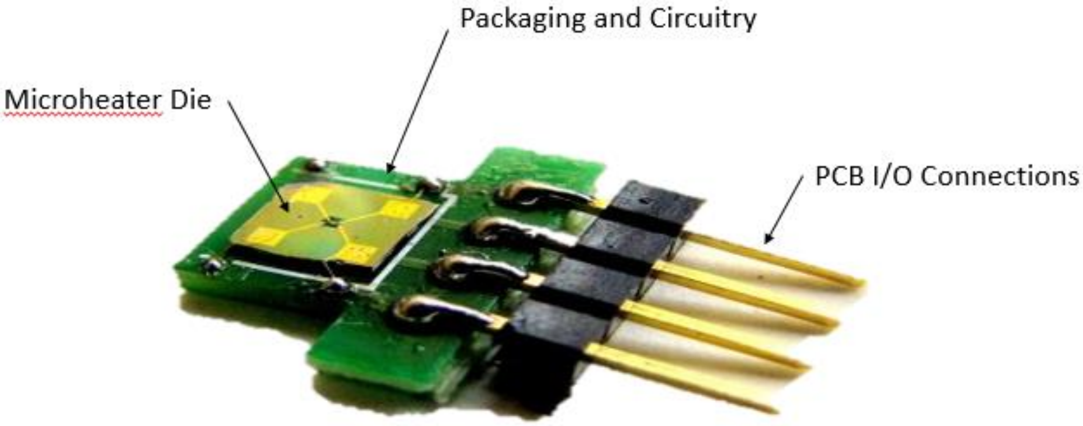

Figure 12-Microheater with Packaging and Electrical Connections [80]

2.3.2 Packaging Materials

Common materials used for packaging of microheaters are metals, ceramics, silicon, and plastics [80]. The material of the packaging device is chosen to withstand the operating conditions. High temperature operation, high pressure, chemical resistance, mechanical and thermal shock, and vibration [81, 82] are typical operational conditions the packaging may encounter.

Metal packaging is often used for the quick turnarounds for prototyping. This packaging material is robust and easy to assemble and meets the pin count requirement for most MEMS technology [80]. The mechanical integrity and chemically inertness of metals are key features that make this material favorable for applications in harsh environments [83]. Stainless steel is a commonly used metal packaging material used for microheaters due to its ability to stay chemically inert at high temperatures [23].

Ceramics packaging is the most popular material used due to its ease in shaping and material properties (e.g. electrical insulating, hermetic sealing, thermal conductivity, chemically inertness) [80, 83]. Ceramics decrease the complexity of designs by integrating the packaging in to the MEMS. Fabricating them as one integrate piece eliminates many steps and reduces the fabrication time. This was done for thick film microheaters where the same LTCC substrate, containing the microheater, could be dually used as the packaging device and its circuitry components [84].

Plastic packaging is primarily fabricated from three different methods. These methods are plastic molding, plastic embossing, and more recently 3D printing. Plastic molding and embossing are favorable for its ease of mass production once an initial mold is created. These materials are even starting to be integrated into fully assembly design where circuitry will be created by making polymers conductive [85]. Plastic packaging typically has a temperature limitation of 250^0C, but depending on the polymers, the specific polymer used can have many different susceptibilities to chemicals. 3D printing makes development easy due to the ability to create a minimal number of packaging devices without spending the overhead for an additional cost of fabrication. Another idea for 3D printed packaging is a printer by Donald Hays et al. which was created to rival mass production methods. This printer eliminates all packaging and electrical connections into a 1 step, hit print, process. Here they printed the packaging for micromirros out of polymers, and electrical connections out of soldering paste to form electrical connections using ink jetting technology [86].

Multichip packaging is a common process used that utilizes the same MEMS/IC fabrication that the initial die is typically built. Studies have shown that many industries are pushing to modularize their technologies [79]. In multichip fabrication, different silicon based manufacturing methods using etching, deposition, and photolithography processes are used to create the packaging structure. Anodic and fusion bonding are surface micromachining methods that are also commonly used for this type of packaging device. This bonding method enables the combination of the wafer containing the initial die to another glass or silicon wafer containing any additional circuitry, enclosure, or necessary components of operation. Integration of MEMS systems into MCMs offers reduced size, electronic noise, and system power [87].

2.3.3 Electrical Interconnects

Electrical interconnects are the means by which the die is connected to the packaging device. This is an essential part of providing power and creating feedback temperature controllers in microheaters. Electrical interconnects take the microheater device and give it a macroscopic connection enabling it to be controlled and easily connected without the use of microscopes and high dollar equipment. As devices get smaller and more complex so does the means of fabrication and cost rises; so it’s essential for developmental stages for this technology to be scaled up. Wire and tape bonding, flip chip technologies, soldering, and printing are some of the more common methods of creating interconnects. Often times these connections are protected by high temperature epoxies in microheaters to ensure they don’t melt during operation [16].

Wire and tape bonding are very popular and well-established methods of creating an electrical connection from the die to the packaging device [79]. This method is commonly called thermosonic bonding or ball bonding. Heat, pressure, and ultrasonic energy are used to bond the area on a contact pad to a wire, but some processes don’t use all three forms of energy to create the bond. The term ball bonding comes from the spherical shape created by the wire connection to the initial pad. Gold and aluminum are the most common materials used in wire bonding.

Aluminum is preferred for higher current operations, but gold tends to bond easier than aluminum [87].

Flip is a bonding technology where the die, containing conductive connections on the top side is placed face down on another substrate with conductive connections on its surface. Plated solder bumps are used on pads to bond the pads together. This technology is ideal for tight spacing. Gaps between the die and package are 50 µm – 200 µm. Flip chip has a unique advantage over wire bonding in that (I/O) connections can be placed anywhere on the die without having to worry about crossing wire connections.

Printed conductive leads is a new and quickly evolving field. Sawyer B. Fuller et al. used 3D printing to fully fabricate a MEMS device by ink jetting metal nano-particles and sintering them together. This method was used with 5 µm accuracy and the sintered ink had twice the resisitivity of the material in its bulk form [88]. Another popular device being used to print conductive leads is the Optomec Aerosol printer. This device can print leads with +/- 10 µm accuracy, and has shown to be an excellent tool to repair MEMS devices and other electronics [7, 8].

2.4 Calibration and Testing of Microheaters

Testing and fabrication are necessary for almost all circumstances due to the differences that arise in the microstructures from variations in parameters of the fabrication method [16, 89]. Without testing and calibration, the control and feedback systems cannot be developed. Also, microelectronic circuits are commonly tested before being diced by probing stations and different automated electronic test equipment to provide initial testing on their behavior [63, 90].

Microheaters are typically tested before being diced to ensure they function before money and time are spent packaging the devices [91]. Through initial testing continuity and the room, temperature coefficient of resistance is measured which is also an essential component of control and feedback systems. In a secondary testing process that often occurs after packaging and electrical connections, the electrical and thermal properties of the device can also be checked and calibrated over a temperature range. A typical calibration process was described by K.L. Zhang et al. [16] where the device was placed in a furnace and the different material properties, primarily the resistivity, were calculated over a range of temperatures. To ensure data was accurate, thermocouples were placed in the furnace close to the heater to know the exact temperature at the location of the heater. This was shown to be an accurate method of calibration in Glod et al. [89].

Having found the material properties enables capabilities of calibrating sensor technology to accurately monitor the temperature of a heater as well as control the amount of power required to reach the desired temperature [89, 92]. Important properties used in calibration are the resistivity, temperature coefficient of resistance [93], emissivity, specific heat, and thermal conductivity [16].

2.5 Precision Linear Control Systems

Control of a precise gap, ~1 µm - 100 µm, is a critical aspect of the SRS process. This is due to a microgap required between the heating device and the material to be sintered. For this reason, a review of technology and relevant subjects is needed to create a micro precision gap. Control systems for this device need to have the resolution of 1 µm and range of motion of at least 100 µm which was determined from modeling results as part of the operational parameters of this method of printing.

2.5.1 Introduction

Precision control systems can be generally defined by manufacturing tolerances which are better than one part in 10^5 [12]. To obtain these tolerances, actuation methods need to be within a micron to submicron range. Common industries in which these technologies are used are in semiconductor manufacturing, magnetic and optical memory manufacturing, high-resolution imaging, and precision metrology. Depending on the operation of the system, many different methods of actuation are used to achieve this precise control. Overall, these systems can be divided up in two critical elements of precision control which is sensor technology and actuation methods.

2.5.2 Actuation Methods

Common challenges in the field of precision actuation methods are found in providing long ranges of motion with a precise resolution for an economical price. However, some of these systems have achieved these objectives and found their way into commercial applications.

One such device is part of the read/write system of computer hard drives. This system utilizes a voice coil motor to provide long range of motion, but the precision of the technology is limited to ~1 µm [94]. This lack of precision has been under development, and one of the emerging areas of technology addressing this resolution issue is to have a dual stage actuation device. In this dual staging, common applications have been to add a piezo actuation system. Piezo actuation is a favorable system for rapid response and ultra-high resolution [95], but the motion of the systems is often drastically reduced to ranges of 100 µm [96, 97]. However, for fine precision systems, PZT piezo actuation systems offer the most precise control at 10 pm [96]. Piezo actuators have been manipulated to achieve 200 mm ranges of operation by using an inch worm technique where different piezo actuators move a worm shaft [98].

A newly evolving field of actuators popular in MEMS devices is shape memory alloys (SMA). These alloys are able to retain their exact shape after being deformed. At high temperatures, these devices can exhibit large deformations extending into the super elastic regions of the material. This makes them ideal for usage as a thermal actuator. Thermal actuator actuation length is dependent on the thermal expansion between materials but is commonly used in MEMS to achieve actuation of ~100 µm [99].

One of the most commonly used systems is a stepper motor or DC motor coupled to a precision screw and nut set to create a linear pusher. This is a popular and well known method of actuation that has been used for ~100 years. Current systems have been recorded with resolutions of 49 nm with motion range up to 5 cm by Applicable Electronics [96]. An evolution of the stepper motor is the permanent magnet linear motor. This motor is naturally akin to applications requiring high speed and precision. Precisions as high as 5 nm have been recorded from these linear translation systems [100]. In addition, these systems have been recorded to have translation speeds of 3-5 m/s [101]. The downsides of the permanent magnet linear motors are: 1) they cost nearly $500 for 100 mm of travel length; 2) the force is proportional to the cross sectional area; 3) suffers from resistive heating losses [101].

2.5.3 Sensor Technology

Closely related to actuation method is the sensing technology that determines the position of the device. In most cases, high precision control is difficult or costly to obtain without some form of feedback. In addition, it is nearly impossible to know the relative position of the actuation device on micro scale movement systems without some form of sensor measurement. Often times these devices are integrated into the systems, making them dually purposed devices. This is commonly seen in piezo actuation and stepper motors. Noise and resolution of a sensor are some of the most misreported aspects to sensor technology due to the failure to mention bandwidths of the device operation and lack of statistically verified information [102]. Position sensors are designed to produce an output that is directly proportional to the measured position, however, all position sensors, in reality, have an unknown offset, sensitivity, and nonlinearity to some extent. This creates uncertainty in the actual position being measured and is often taken into account in the control aspects of the systems [102].

Resistive strain gauges are low cost, simple, and widely used for nano and micro positioning sensors. They're most commonly used in piezo actuators, and can be integrated into the actuator itself or bonded to the actuator surface. This offers a closed feedback system to help increased accuracy of piezo actuators [103].

Capacitive position sensors are another type of sensing devices that can achieve nano to micron scale sensing. These devices are commonly used in combination with electrostatic microactuators due to their ability to be used as an open or closed loop control setup. The capacitance variation of this sensor to measure on this small scale is ~100fF/µm [104]. The advantage of this sensing system is that it's a non-contact method with very high resolution.

Eddy-current sensors work on the principle of electromagnetic induction [105]. Like capacitive sensors, this is a non-contact method of sensing. They also work in a similar method to capacitive sensors in that they require an oscillator and a demodulator to derive the resistance [106]. These sensors use a method of shielding to prevent magnetic interference from interrupting signals, but this also significantly limits the range of the sensors. This continues to be a critical limitation of this type of sensing device. A similar device is the inductance proximity sensor. This sensor uses an inductive target instead of a conductive target, but all operational equipment for the devices is the same. Typically these sensors operate between 100 µm - 500 µm. These sensors are not as popularly used due to the susceptibility to temperature and magnetic interferences [102].

Linear variable displacement transformers (LVDT) have been used in some of the harshest environments due to its rugged properties. This sensor is popular due to its contactless sensing, linearity, virtually infinite resolution, low temperature sensitivity, robustness, and ease of implementing its radiation harness [107].

A popular laser positioning system, laser triangulation, works by sending a source light towards an object whose position is desired to be measured. The light reflects off of the surface. This reflection is picked up by a detector which measures the angle between the original light source and the returning light to determine the vertical position of the object. The disadvantage of this systems is often the reflectiveness of the surface [108]. Other types of lasers have been used for position measurement such as the laser interferometer providing accuracy of a few parts in 10^{11} [109]. These systems are typically more expensive than other precise measurement systems and are sensitive to interference such as dust. However, they have the greatest range of any nano to micro positioning system at ranges of meters [102].

Linear encoders are also commonly used micro positioning sensors. Linear encoders work by optical encoding, magnetic, capacitive, and inductive. Optical encoders have the highest resolution of all the various methods of encoders. However, optical encoders suffer from interference such as dust. Other encoders tend to be more reliable than optical, but do not have as high of resolution [102].

2.6 Sintering of Micro and Nano Particles

Millisecond sintering of micro and nano particle by use of a resistive microheater via conduction through the air is the ultimate objective of this thesis. Sintering is the process that will enable 3D geometries to be formed by the diffusion of the grain boundaries to form a singular solid. Sintering is a complex behavior through which many of the modeling aspects are computationally expensive. In attempts to reduce the computational expense many people have come up with simplified models. Research has also proven that this is a feasible and advantageous method of forming 3D geometries in processes such as the popular SLS, SHS, and photonic sintering methods of printing. In this section, we will review the current developments in sintering micro and nano sized particles. Through this review, the feasible limits of this technology and process will be defined.

2.6.1 Sintering Behavior

Materials behave differently on the microscopic level. This is the beneficial aspect of using micron and nano sized particles to create sintering. It enables particles with high melting temperatures to be sintered much below their melting temperatures. Nano particles can sinter at temperatures ranging from (.2 - .3)*T_m, where T_m is the melting temperature of the material. In micron sized particles this typically occurs in the range of (.5 - .8) *T_m. Nano-scale sintering processes have been shown to create higher densities at above 95% but are more difficult to control due to particle agglomeration, high reactivity, inherent contamination, grain coarsening, and loss of nanofeatures [110]. Sintering of nano and micron particles of Ag has commonly been done at low temperatures with drying and sintering durations of 5 minutes for drying at 160ºC and curing for 30 minutes at 160ºC [111]. It has been recorded that for low temperature materials like Ag and Au that sintering can often occur at temperatures as low as 150 ºC [112]. However, to increase the speed of sintering to as desired rate in the SRS system for 1 *m*s thermal response, temperatures at which the material is sintered must be increased. This phenomenon has been proven in the NovaCentrix Pulse Forge machine. In this process, materials of a couple microns or less are sintered in milliseconds of time. This is done by heating the surface of the material up to temperatures in the range of 400ºC - 1100 ºC, thus proving that sintering can be done in the 1*ms* response time [113]. Sintering can be performed with these high temperatures on mostly any substrate which can withstand ~150 ºC. Due to the quick application of heat, the material properties of substrates below the material being sintered do not have time to change. This makes sintering with temperatures of above 1000 ºC possible on polymer substrates [114]. Quick applications of heat for sintering has limitations. These limitations include: exceeding the gasification temperature of the substrate can cause the film to lift off, materials can be too porous, have too much solvent, or binders may be volatile. Most of these issues can be remedied by ensuring your material is not too porous and offering a low temperature quick pulse of heat for drying before sintering [114].

2.6.2 Prediction through Simplified Models

An important part of establishing operating parameters of the SRS printer is identifying simplified methods of the heat transfer involved with millisecond sintering processes. Different thermal conductivities of materials can create a wide range of operational constraints on the heat transfer of this device. A popular method of modeling is by assuming the material to be sintered is in bulk form. This has been proven in the modeling software developed by NovaCentrix for millisecond sintering of thin film materials [115], and again in a study on modeling of laser powder bed fusion [116]. In these processes, an accurate representation of the thermal conductivity and density of the powder beds is a necessary component of the modeling of heat transfer. The Zenhner-Schlunder's model [117], later improved by Samuel Sih et al. [118] has been commonly used for the prediction of the thermal conductivity with 30% relative errors when compared to the experimentally measured values. This expression is shown by:

$$\frac{k}{k_g} = \left(1-\sqrt{1-\varepsilon}\right)\left(1+\frac{\varepsilon k_r}{k_g}\right)+\sqrt{1+\varepsilon}\left[(1-\varphi)\left(\frac{2}{1-\frac{Bk_g}{k_s}}\left(\frac{B}{\left(1-\frac{Bk_g}{k_s}\right)^2}\left(1-\frac{k_g}{k_s}\right)\ln\left(\frac{k_s}{Bk_g}\right)-\frac{B+1}{2}-\frac{B-1}{1-\frac{Bk_g}{k_s}}\right)+\frac{k_r}{k_g}\right)+\frac{\varphi k_s}{k_g}\right] \tag{1}$$

For an overview of the equation:

Ratio of thermal conductivity=Free fluid* [Core heat transfer (incomplete solid contact) + (Complete solid contact)]

Where,

k=effective thermal conductivity of the powder bed, W/m-K;

k_g= thermal conductivity of the gas inside the pores of the powder bed, W/m-K;

k_s=thermal conductivity of the skeletal solid, W/m-K;

ε=porosity of the powder bed;

k_r=thermal conductivity part of the powder bed owing to radiation, denoted by the Damkoler's equation below, W/m-K;

φ =flattened surface fraction of particle in contact with another particle; φ=0 when there is no contact for the particles; φ=1 when there is complete particle contact; and

B=deformation parameter of the particle; B=0 is the z-axis, B=1 for spherical particles, and B=inf for a cylinder

$$k_r = \xi s d_p e \sigma (T_b^2 + T_l^2)(T_b + T_l) = 4\xi s d_p e \sigma T_b^3 \tag{2}$$

Where,

ξ=the area fraction occupied by the canals for the radiation per total unit area,

s= a numerical factor about 1, sξ=1/3

d_p=the diameter of the powder particle

e=emissivity,

σ=Stefan-Boltzmann constant=5.67E-8 W/m^2-K^4

T_b=temperature of the powder bed, and

T_l=temperature of the surrounding assumed to be near to T_b

Using this equation, the thermal conductivity of powders in bulk form can be calculated for modeling purposes. The thermal conductivity relationship in Equation (1) and Equation (2) has also been proven by Stephen U. S. Choi et al. [119] using similar equations. The bulk density or porosity of the material is also an important factor for the thermal conductivity and heat transfer. The effects of this have been shown in different packing densities for powders where thermal conductivity ranged .05 W/m-K - .25 W/m-K in different Cu, Ni and SUS 316L metal powders [120].

Chapter 3 MICROHEATER DESIGN, PACKAGING DESIGN, AND FABRICATION

Microheater design, fabrication, and packaging are essential to the selective resistive sintering process. In this section, the methodology and results for the design and optimization of the microheater are provided. This is followed by a specifically defined and detailed fabrication plan, the design of the packaging, and prototyping. The results of the microheater design, fabrication, and packaging will be assessed at different intervals during the fabrication to ensure the device functions as intended. The prototype will be tested using a unique test setup prior to its actual functioning assembly discussed in the next chapter.

3.1 Microheater Design

As defined in the problem formulation, a heater needs to be designed that can operate at temperatures of 600^{o}C or above in a time span of 1 *ms* or less with low power consumption. In this chapter, we develop an understanding about the order of magnitude in the different scenarios through the evaluation of analytical models. The designs are then, further evaluated using numerical modeling. In the numerical modeling, an optimization code is developed using particle swarm optimization (PSO).

3.1.1 Numerical and Analytical Modeling

The design of the microheater can be improved by two methods of modeling. These two methods include analytical modeling and numerical modeling.

3.1.1.1 Analytical Modeling

Analytical modeling is a mathematical model with a closed form solution. Analytical models are used to gather information relative to the order of magnitude of a solution and to understand the governing physics and variables effecting the design. They also provide a simplified model for a basis to the understanding of the physics. This enables us to find solutions for problems based on parameterized inputs describing the changes in a system. Electrical, heat transfer, structural mechanics, and electro-thermal characterizations are all used to help predict solutions analytically.

3.1.1.2 Electrical Characterization

Electrical characterization is defined by the circuitry of the heater. In this scenario the heater circuitry can be treated much like a basic resistor such that:

$$R = \rho_r \left(\frac{A}{l}\right) \tag{3}$$

&

$$P = I^2 R \tag{4}$$

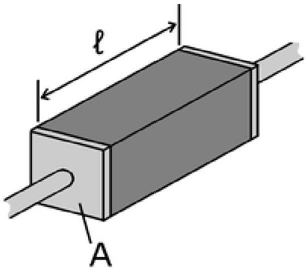

Figure 13-Description of Geometric Entities used in Resistance Calculations

where R is the resistance, ρ is the intrinsic property, resistivity, A is the cross sectional area of a resistor, *l* is the length of the resistor as illustrated in Figure *13*, *I* is the current in the circuit, and P is the power loss from resistive losses in a circuit. Power lost due to resistive losses is transferred into mostly thermal losses. In this way, the electrical power is coupled to heat transfer.

3.1.1.3 Heat Transfer

The most significant forms of heat transfer in microheaters, conduction, and convection, are critical to understanding the key parameters of heat transfer through a medium to sinter an object. This can be analytically described by:

$$Q = \frac{kA\Delta T}{L} + hA\Delta T$$

$$Q = conduction + convection \tag{5}$$

where k is the thermal conductivity of the material the heat is being transferred through, A is the cross sectional area, ΔT is the temperature difference, L is the length, and h is the convection coefficient.

3.1.1.4 Electro-thermal Response

The electro-thermal response is an equation derived from the time taken to heat a material based on its intrinsic thermal and electrical properties. The two were coupled together by relating the electrical energy loss from (4 to the thermal response of the energy absorbed from the heaters heat capacity. This is shown by:

$$V = \sqrt{\frac{C_p \rho_0 \rho_r \, l^2 \Delta T}{t}} \tag{6}$$

where C_p is the specific heat, ρ_0 is the density, ρ_r is the resistivity, l is the length of the element, t is the time it takes to heat the element, V is the voltage, and ΔT is the temperature difference to achieve.

3.1.1.5 Structural Mechanics

Thermal stresses are resultant from the difference in thermal expansion of different materials and are predicted by:

$$\sigma_s = -\alpha \Delta T E \tag{7}$$

where σ_s is the stress in the material, ΔT is the temperature difference, and E is the Young's modulus of the material.

3.1.1.6 Summary of Analytical Characterization

Microheaters are governed by electrical, heat transfer, and structural physics. All three physics are coupled together in this modeling by ΔT. It can be seen in (6 that the power consumed is significantly dependent on the thermal response desired. This also is related to the heat transfer, where if a specific material has a high thermal conductivity more power will be required for the heater due to heat transferring away more readily as shown in (5.

Analytical solutions were used to provide an initial guess for the amount of power that would be required to heat the microheater to 600 ºC. (6 displays that the temperature difference has a significant impact on the amount of power input into the microheater. Using (6 again, it was found that a .603V voltage supply would be required to have enough heat to heat just the resistive element alone. During the actual usage of the heater, the heater would also have convection and conduction transferring heat away from the heater into other materials, as shown in (5. This causes the power required to increase significantly. Using the information above the analytical solution was calculated providing a lower bound for the amount of power required for this heater. The results of the temperature, thermal response time, and the voltage applied are listed below.

Table 5-Electro-thermal response Results Based on Analytical Modeling

Temperature	Time	Voltage
600 ºC	1. *ms*	.603 V

3.1.2 Numerical Modeling

Numerical modeling of a microheater involves multiple coupling physics. The physical phenomenon experienced in a microheater is that of Joule heating. Joule heating consists of electric currents and heat transfer. In this simulation the structural mechanics involved were also considered which were coupled with heat transfer by thermal expansion. In this section, a model for microheater operation is developed. This section walks through the governing equations used to predict the electrical, thermal, and mechanical response of a microheater. A grid study analysis is included in final remarks in this section, to ensure the results are independent of the numerical meshes.

3.1.2.1 Current conservation

Joule heating is created by running current through a resistive material. The constitutive relationship for the resistive material is described by Ohm's Law:

$$\boldsymbol{J} = \sigma \boldsymbol{E} \tag{8}$$

J is the current density, **E** is the electric field strength, and σ is the electrical conductivity:

$$\sigma = \frac{1}{p_r} = \frac{1}{p_{r,0[1+\alpha(T-T_0)]}} \tag{9}$$

where p_r represents the electrical resistivity, α is the temperature coefficient of resistivity with the assumption that the resistivity changes linearly with temperature, and $(T - T_0)$ is the change in temperature of the resistive material.

Based on charge conservation and equation of continuity, the electric potential throughout the microheater can be described by:

$$-\nabla_t \cdot d(\sigma \nabla_t V) = 0 \tag{10}$$

where d is the layer thickness, V is the electrical potential applied, and ∇_t denotes the gradient operator in the tangential direction of the electric field. Resistive heating is induced from the resistivity in the circuit opposing electron flow. This opposition creates heat that can be shown by:

$$Q = \sigma|\nabla_t V|^2 \tag{11}$$

where Q is the heat being generated. The equations are coupled together based on the governing equations dependent on other physical phenomena.

3.1.2.2 Heat Transfer

Heat transfer follows the law of thermodynamics. In microheaters, heat produced by Joule heating is primarily transferred away by conduction and convection for temperature below 700 ˚C. Since only these forms of heat transfer are present, the first law of thermodynamics ultimately reduces to the governing equation for heat transfer:

$$\rho C_p\left(\frac{\partial T}{\partial t}\right) - \nabla\cdot(k\nabla T) - h\nabla T = Q \tag{12}$$

The unknown variables are the heat source Q and $\frac{\partial T}{\partial t}$ represents the change of temperature with respect to time and ∇ is the gradient operator.

3.1.2.3 Structural Mechanics

Stress is induced in microheaters as a result of thermal expansion when materials experience a rise in temperature. The governing equation for the structural mechanics is:

$$\frac{\rho(\partial^2 \boldsymbol{u})}{\partial t^2} = \nabla \cdot s + \boldsymbol{F}\mathrm{v} \tag{13}$$

where s is the stress tensor, **u** is material displacement, and **F**v is the volume force vector.

The computational cost of modeling microheaters can be extensive due to the large ratio of the thickness of the resistive material layer (typically ~200 nm) to that of the substrate (~ 25 µm), and could cause significant meshing issues. One way to simplify is by using the shell theory. Structural mechanics shell theory is different from three dimensional structural mechanics in that the models are formulated by using the Lagrange continuum mechanics with mixed interpolation of tensor components. This reduces computations to consider only plane stress since other stresses will have minimal impact. The mechanical stress is formulated as:

$$\frac{\mathrm{\rho}\left(\partial^2 \mathbf{u}_2\right)}{\partial \mathrm{t}^2} = \nabla \cdot \mathrm{\sigma} + \mathrm{Fv} + \frac{6(\mathrm{M}_\mathrm{v} \times \mathrm{n})\mathrm{z}}{\mathrm{d}^2}\ \& \tag{14}$$

$$\mathrm{\sigma}_\mathrm{z} = 0 \tag{15}$$

where σ is the in plane stress, $(\mathrm{M_v} \times \mathrm{n})$ is the volume moment vector, z is the vertical direction, and d is the overall thickness of the shell. The stresses induced in the design are all resultants of thermal expansion which is shown from the thermal strain as:

$$\varepsilon_{\mathrm{th}} = \alpha_{\mathrm{th}}(\mathrm{T} - \mathrm{T_0}) \ \& \tag{16}$$

$$\mathrm{x_{th}} = \frac{\alpha_{\mathrm{th}}(\mathrm{T} - \mathrm{T_0})}{\mathrm{d}} \tag{17}$$

where x_{th} corresponds to the strain subject to the bending stress in the shell from thermal expansion, $\varepsilon_{th}$is the strain in the entire domain from thermal expansion, and α_{th} is the thermal coefficient of expansion. The thermal expansion can be coupled to (13) and (14) using the stress-strain relationship of materials

3.1.2.4 Grid Study

The critical, or smallest, dimension in the model determines the largest grid size that can be used to create the elements for modeling. In a numerical model, the angle between nodes needs to be greater than 10º or the model may result in singularities. Using the critical length the smallest element length can be predicted by simple geometry from:

$$\frac{y}{x} = \tan(10°)$$

(18)

where y is the smallest dimension and x is the smallest element length. Default settings in COMSOL provided meshing smaller than this dimension which resulted in no change in the solution when decreasing mesh size. It was noticed that when using default settings in COMSOL, the extremely fine settings had a smaller mesh size than what was predicted. The solutions from the mesh found using (18) were compared with the solutions from the default settings and findings were conclusive that there were no differences in the solutions. The extremely fine default settings were used for the remainder of simulations.

3.1.2.5 Validation of the Numerical Model

The numerical model was implemented using COMSOL 5.1. A multiphysics model was developed for a Pt microheater on an alumina composite substrate by coupling the three physics involved (i.e., electrical, mechanical, and thermal). This study evaluated the temperature change in the microheater and substrate. To form a solution the numerical model was evaluated transiently.

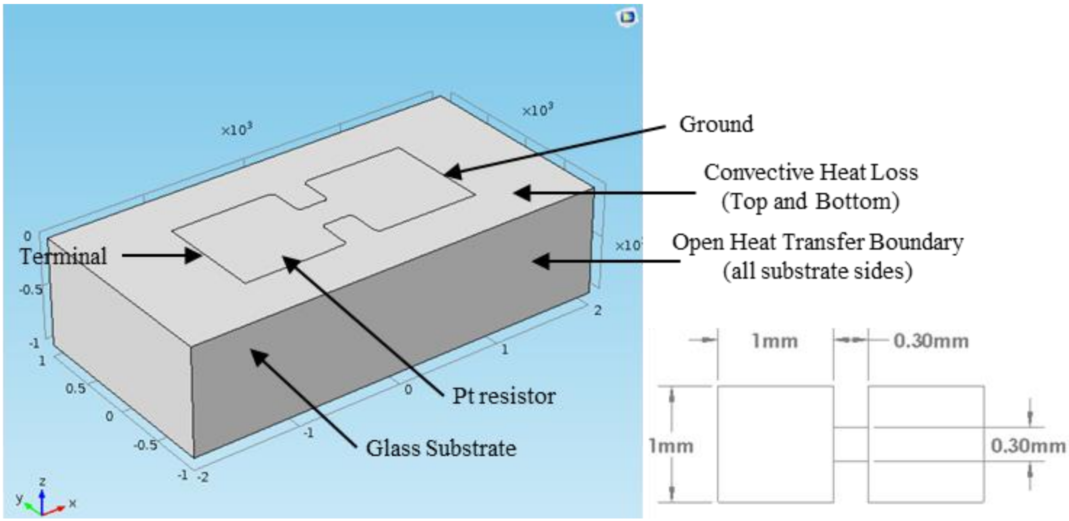

Figure 14-Heater Geometry and Boundary Conditions

Table 6-Material Properties for the 1st Numerical Validation

Summary	Pt	Al2O3
Specific Heat (J/kg*K)	133	800
Thermal conductivity (W/m*K)	71.6	25
Coefficient of Thermal Expansion (1/K)	8.80E-06	6.50E-06
Density (kg/m^3)	21450	3780
Temperature Coefficient of Resistance (1/K)	3.93E-03	-
Resistivity (Ω*m)	8.33E-07	-
Young's Modulus (Pa)	1.68E+11	4.00E+11
Poisson's Ratio	0.38	0.22
Function	resistor	substrate
Thickness (μm)	0.6	1000

Figure 14 and Table 6 shows the initial setup of the numerical model, where the shell boundaries of the Pt resistor were centrally located on the substrate. The open boundary condition was placed on the boundary where the domain would be continuous. This assumes $q|_{x=boundary} = 0$ so the temperatures of the un-modeled part have continuous temperature change at the boundary. The convective heat loss coefficient applied to all other sides was 5W/m*K, which has been commonly used in literature [16, 22].Table 6 shows the material properties.

The model was validated by comparing the simulation results with the experimental data obtained from literature [22], which are shown in Figure 15. The change of temperature at the center of the microheater after 200 *ms* with respect to input voltage was compared. As we can see, the results have an excellent agreement between our numerical simulations and the experimental data from the literature.

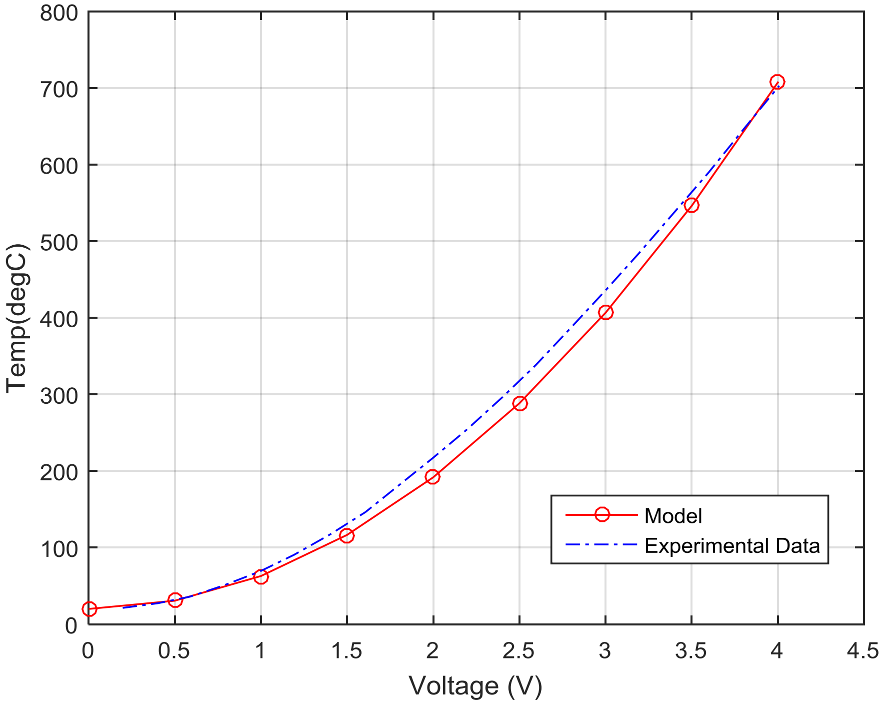

Figure 15-Temperature Change with Voltage Input Comparing Numerical Modeling with Experimental Data

A second validation was also performed on the transient response of the microheater over time because of the importance of transient behavior of a microheater. Simulations of a Ti/Au resistor on a 7740-Pyrex glass substrate were performed to compare with experimental results and other modeling results from literature [16].To simplify this model, the conductor layer composed of Au/Ti was modeled as two resistors in parallel. This was assumed due to the parallel orientation in which the materials were stacked and current was supplied through the conductive layer. The convection coefficient used in this model was 100W/m*K to be accurate with experimental setups [16]. The simulation configuration and material properties are shown in Figure 16 and Table 7 respectively.

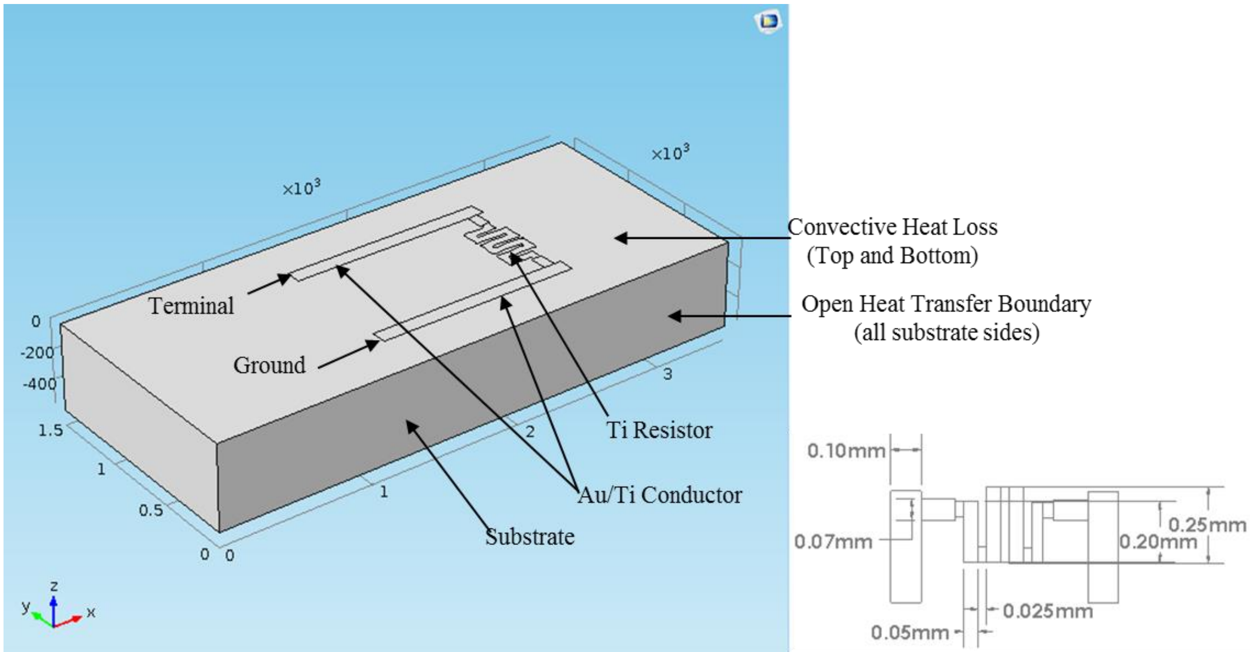

Figure 16-Geometry and Boundary Conditions for 2nd Validation

Table 7-Materials Properties used for 2nd Validation

Summary	Pyrex-7740	Au	Ti
Electrical Resistivity (Ω*m)	1.26E+06	3.99E-08	1.54E-06
Thermal Conductivity (W/m*K)	1.18	1.76E+02	5.8
Specific Heat (J/kg*K)	753.12	0.3	131
Density (kg/m^3)	2230	19320	4507
Temperature Coefficient of Resistance (1/K)	-	3.40E-03	1.30E-03
Young's Modulus (Pa)	1.16E+11	6.40E+10	7.00E+10
Poisson's ratio (1)	0.321	0.2	0.44
Thermal Expansion Coefficient (1/K)	8.60E-06	3.25E-06	1.42E-05
Function	Substrate	Conductor	Resistor
Thickness (μm)	550	0.077	0.206

Having setup the numerical model, solutions were then created to form a validation. A 3V potential difference was placed on the resistor, and then the maximum temperature recorded over the entire microheater configuration was extracted at each time step. The transient temperature change over time was compared to previous experimental and modeling results shown in Figure 17 [16]. From the comparison, we can see a good agreement. The model being validated agrees more closely with the experimental data as it approaches a steady state than the results from the previous model [16].

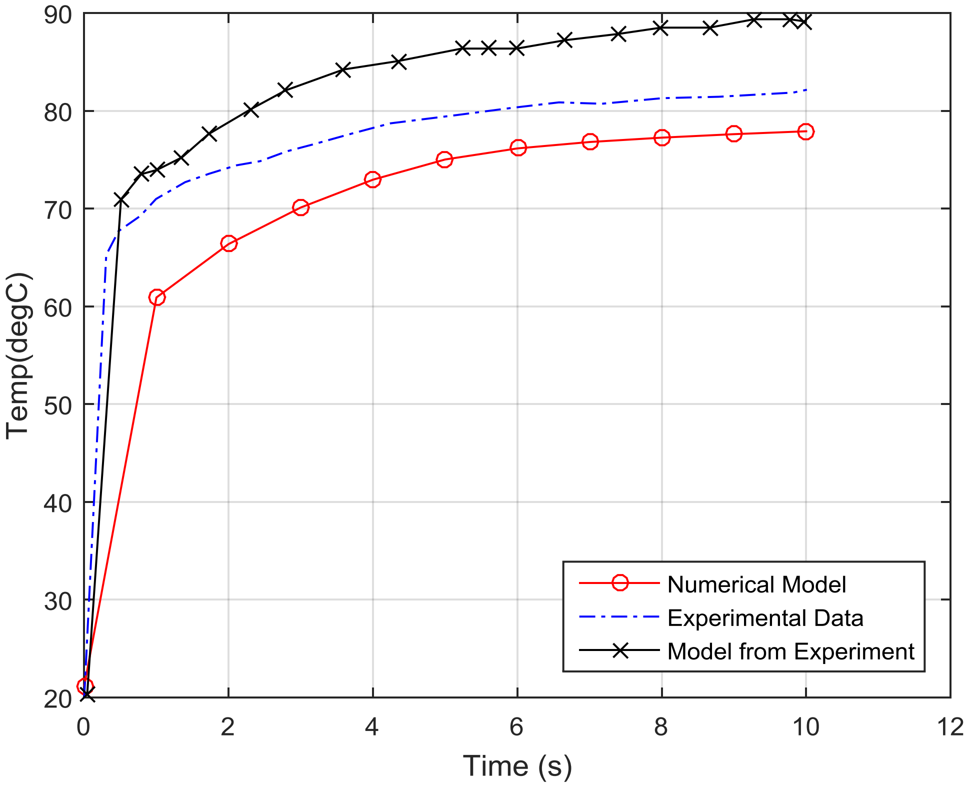

Figure 17-Comparison of Numerical Model to Data Obtained from previous Numerical Work and Experimental Validation

3.1.2.6 Summary of Numerical Modeling

In this section, a numerical model was developed, the grid size was defined, and appropriate boundary conditions and material properties were applied to the model to validate the model. Simulations were performed to compare with two different experiments. Results show good agreements, which validates the developed numerical model.

3.1.3 Microheater Design Optimization

To optimize the design of the microheater, particle swarm optimization (PSO) method was used. PSO was initially a method of predicting social behavior in animals [121]. This method has been adopted for an extensive amount of applications [122], such as array failure correction for antennas, predictive and tuning controls, design optimization, etc. This method stochastically searches for the optimal solution [123]. The method evaluates the fitness of a current set of solutions and identifies new design parameters based on a fitness evaluation for minimizing an objective function. Each solution generated moves the parameters closer to the optimal solution at which the numerical problem reaches convergence [124]. One recent publication utilized particle swarm optimization in design of microheaters to create power savings for microheaters [65]. This application used analytical models and no numerical models. The parameters used were the oxide layer thickness, temperature, and active area. No attention was given to optimizing for stress nor was the actual geometry of the microheater changed. They also did not consider any constraints, or utilize a finite element model.

3.1.3.1 Initial Design and Variables

Based on our literature review, an initial design of the microheater was chosen as follows. An Ultra-thin Glass (type AF 32*eco from Schott Inc.) was used as the substrate to support the resistive filament and conductive pads. This material was chosen due to its low thermal conductivity making it power efficient [16]. It also has a transition temperature of 717ºC making it capable of reaching the desired operating temperature range before reaching the transition temperature. Titanium was chosen as the resistive material because of its capability of reaching temperatures in excess of 600°C. Its failure from thermal stress is often a limiting factor, but not until temperatures are in excess of 700°C. Gold was also chosen as a resistive material due to its high electrical conductivity. Gold also has a low coefficient of thermal expansion, when compared to other popular conductors like silver, which induces less stress in the design. The material properties are listed in Table 8.

Table 8-Material Properties of Initial Model for Optimization

Summary	Titanium (Ti)	Ultra-thin Glass	Gold(Au)
Electrical Resistivity (Ω*m) @ 20°C	1.54E-06	-	2.77E-08
Temperature Coefficient of Resistance (1/°C)	3.50E-03	-	0.0034
Thermal Expansion Coefficient (1/K)	8.60E-06	3.2E-06	1.42E-05
Thermal Conductivity (W/m*K)	21.9	1.16	3.17E+02
Specific Heat (J/kg*K)	522	820	129
Density (kg/m^3)	4507	2430	19300
Young's Modulus (Pa)	1.16E+11	7.29E+10	7.00E+10
Poisson's ratio (1)	0.321	0.208	0.44
Thickness (μm)	0.2	50	0.2
Purpose	Resistor	Substrate	Conductor

The initial geometric design established was obtained from [34]. It was demonstrated to be capable of creating a minimal temperature deviation across the design space. Figure 18 shows the initial design. The outer radius determines the size of the microheater and was chosen to be 50um for this study. The initial values of the rest of the design parameters are listed in Table 9.

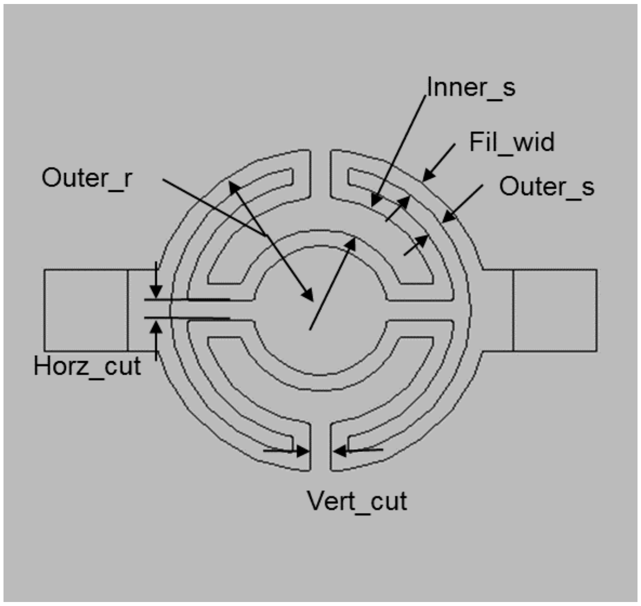

Figure 18-Design Parameters Describing Topology of the Resistor

Table 9-Initial Values of the Design Parameters

Parameter	Value	Unit	Description
Fil_wid	12.5	Um	Filament Width
Outer_s	27.5	Um	Outer Spacing
Vert_cut	25	Um	Vertical Cut
Horz_cut	12.5	Um	Horizontal Cut
Inner_s	10	Um	Inner Spacing
Fil_thick	200	Nm	Filament Thickness

3.1.3.2 Particle Swarm Optimization

With the six design parameters chosen, we needed to determine the optimal combination of the design parameters in the six parameter design space. Because it was impossible to test every design in the design space, an efficient method was needed to search for the optimal design. We developed a unique method for constraining particle swarm algorithms as well as using complex numerical models within the algorithms. In this section, we will use constrained particle swarm optimization to search for optimal geometric design using the variables initially established in the geometry.

In this algorithm, each particle is a design with a set of design parameters (i.e., the six design parameters in Table 9). The lower bound and upper bound of the design parameters determine the boundaries of the design space. Each particle has its own unique position and velocity in the design space. The velocity is determined by the particle's personal best and the global best of all particles and used to updates the particle's current position based on:

$$v = v_i + c1 * rand(\,) * (pbest - present) + c2 * rand(\,) * (gbest - present) \tag{19}$$

Where c1 and c2 are arbitrary constants, pbest is the personal best of the particle, rand is a random number from [0,1], gbest is the overall best is the algorithm, the present is the present solution, and v_i is the current velocity.

The validated finite element model was used to evaluate the fitness of each particle with respect to the design objectives. The algorithm randomly generates initial particles and moves the particles in the design space based on their velocities. This stochastic search enables the convergence of optimization algorithms for complex problems such as a microheater design. Certain designs are undesirable for the microheater, which was accounted for by placing constraints on the particles. One constraint was that the total resistance of the microheater was to be above 100 Ω so that the heat concentrates on the microheater instead of on the external circuit. The constraints are applied using the following procedure. First, the overall resistance of the device is calculated using initially established material properties and the geometry defined by the design parameters. If the calculated resistance is not within the defined constraint, the set of design parameters is discarded and a new set of design parameters will be generated until the calculated resistance satisfies the constraint. Another constraint is used to ensure geometric continuity in the design. Continuity is enforced to ensure that electricity has a free path to flow from the terminal to ground. A break in geometry would disrupt the current flow. This continuity is also calculated from the geometry defined by the input design parameters (Fil_wid, Outer_s, Vert_cut, Horz_cut, Inner_s, Fil_thick). With the stochastic search, the algorithm outputs the optimal design, $x_{optimal}$, and minimized objective function, f_{min}.

The pseudo code of the particle swarm algorithm is presented below.

```
1   Initialize function [$x_{optimal}, f_{min}$] defining the boundary of the design parameters
2   Randomly generate initial particles                  // each particle is a design
3           Check Resistance of the design               //initial constraint
4                   If Resistance>100Ω; continue
5                   If geometry is continuous; continue
6                   Else; go to step 2
7   Evaluate the generated particles using COMSOL
8   Find the best particle from initially generated particles
9   For i=  1: # of iterations
10          Move the particles based on their velocities calculated from ( 19 )
            $x_{n+1} = x_n + v$ where $x_n$ is the position of the particle
11          Check resistance (updated particles)
12                  If R>100; continue
13                  If geometry is continuous; continue
14                  Else; go to step 9
15          Evaluate updated particles using COMSOL
16                  If; objective function value< previous objective function value, update
                    particle position
17                  Else; keep previous particles
18          Keep best particle
19          Update the velocities for each particle
20          Evaluate iteration number
21                  If  i>max iteration; go to step 23
22                  Else keep the best value; go to step 7
23  Solution=[$x_{optimal}, f_{min}$]
24  End
```

3.1.3.3 Results and Discussion

Boundaries of each design parameter are defined in Table 10. The first objective function was to minimize the maximum stress over the entire microheater. Only thermal stresses in the substrate are accounted for in this design. Stress is sometimes induced in the devices from fabrication methods and exist in other parts of the microheater (i.e. filament, adhesive interface), but are not taken into account here. The second objective function was to create even heat distribution by minimizing the standard deviation of temperature within 121 evenly distributed sample points over the entire microheater. The amount of sample points used to evaluate the model was determined to be sufficient in this study because increased number of points above the 121 points didn’t change the standard deviation. Even heat distribution was accomplished within the sample space by optimizing variables input to the optimization algorithm. For the simulations, power was supplied at 1W for 1 ms. The simulation creates a temperature of ~600ºC within the design for both objectives. Results from optimization are in

Table 11 and Table 12.

Table 10-Upper and Lower Bounds of Design Parameters used for Optimization

x values in µm	Fil_wid	Outer_s	Vert_cut	Horz_cut	Inner_s	Fil_thick
Lower bound	4	7	7	7	10	0.15
Upper bound	4.25	10	11	11	17	0.2

Table 11-Initial and Optimal Design Parameters

x values in µm	Fil_wid	Outer_s	Vert_cut	Horz_cut	Inner_s	Fil_thick
Initial	4	7	11	10	13	0.2
Optimal Stress	4.1	8.5	11	10	17	0.2
Optimal Heat Distribution	4.2	8.9	10	10.7	14.9	0.2

Table 12-Values Obtained for the Initial and Optimal Design

Values	Optimal Stress (MPa)	Optimal Heat Distribution (degC)
Initial	96.6	90.6
Optimal	93.5	89.7

The stress resulting from the difference in thermal expansion in the materials was reduced from 92.1 MPa to 88.7 MPa. This is within the yield strength of the Ultra-thin glass making this a feasible design. For even heat distribution, the initial design had a standard deviation of 92.2ºC and was reduced to 90ºC. Results from the single objective optimization problems were compared as shown below Figure 19. Differences in the geometry can be seen from Table 11, but the values obtained for the solutions show a little difference compared to the initial design. This may suggest that a larger design space should be used. This will enable a greater variation in results by adding or redefining the design parameters.

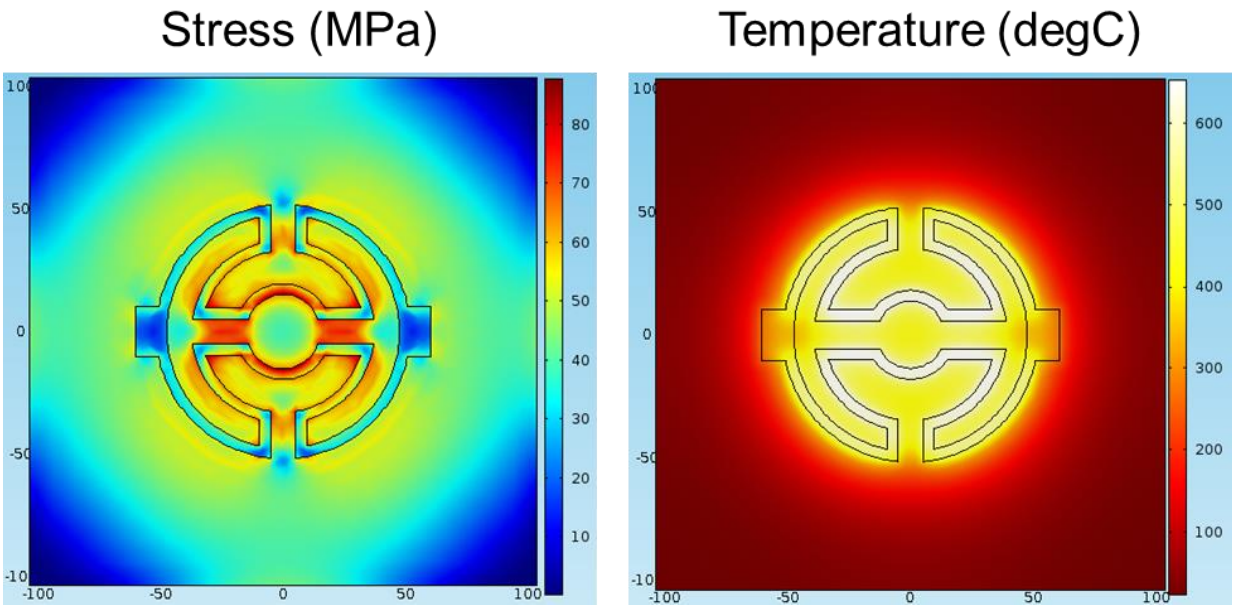
Stress (MPa)

Temperature (degC)

Figure 19-Comparing Optimal Solution of Minimizing Stress with Even Heat Distribution

The six design parameters, Fil_wid, Outer_s, Vert_cut, Horz_cut, Inner_s, Fil_thick, all have a limited range that they can move to vary the geometry. However, for the optimization presented, Inner_s (spacing between sections of filament closer to the center of design) must be larger than Outer_s (spacing between sections of filament closest to the outer radius of design) due to the trivial observation that heat will tend to be concentrated more at the center of the heater. Both of these parameters are also constraining the diameter of the center section of the filament. When the sum of the parameters Inner_s and Outer_s becomes large enough it will cause a stress concentration in the center. This is due to the heat concentrations and stress concentration from the small radius of the center section of the filament. The parameter Horz_cut (parameter along the horizontal axis of symmetry) will always be greater than Vert_cut (parameter along the vertical axis of symmetry). Again this is due to the heat concentrating at the center. As Fil_wid (width of the filament) increases it will cause a heat/stress concentration. This is due to the fact that more heat is squeezed into a predetermined diameter of the microheater. However, if this value is too small, it will also increase stress due to the large temperature gradient from a smaller heating source.

A particular point of interest in this study was the convergence and solve time of the algorithm. The algorithm used 5 particles and 50 iterations, which takes around 12.5 hours to run. The best solution at each iteration was recorded and plotted against the iteration number. As shown in Figure 20, the algorithm had converged around 10 iterations and 26 iterations for minimizing temperature variation and stress respectively. From this, we learn that this algorithm not only converges but that it converges quickly.

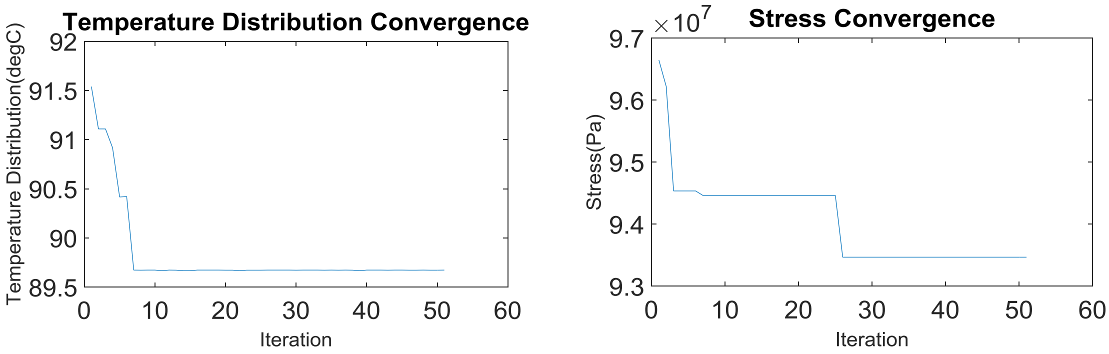

Figure 20-Convergence of Optimization Problems

3.1.4 Scaling to an Array

The optimized design of the microheater was used in a 4-heater array in the final design of the microheater printing system. A 4-heater array was chosen to prove that multiple heaters could operate in unison while providing only minimal additional cost, which would arise from the additional power consumption. The fabrication cost, however, would remain, for the most part, the same. Additionally, using multiple heaters helps to digitalize the printing process rather than raster a moving print. This operates by firing a heater in a different location, or firing multiple heaters at one time, instead of physically rastering heaters to the desired location. Two features were changed from the optimized design. The filament width, parameter fil_wid, was switched to 5 µm due to the lack of impact on design and desire to have whole numbers during fabrication. The thickness of the filament, fil_thick, was also changed to 150 *nm* to save material cost and time during fabrication. From these changes, the power consumption was slightly affected requiring 1.1 W of power per heater to have a thermal response time of 1 *ms*. This change of power is primarily caused by the reduction in thickness of 25%. The following final configuration used for this experiment is shown in Figure 21 and is used for all modeling for the remainder of this dissertation.

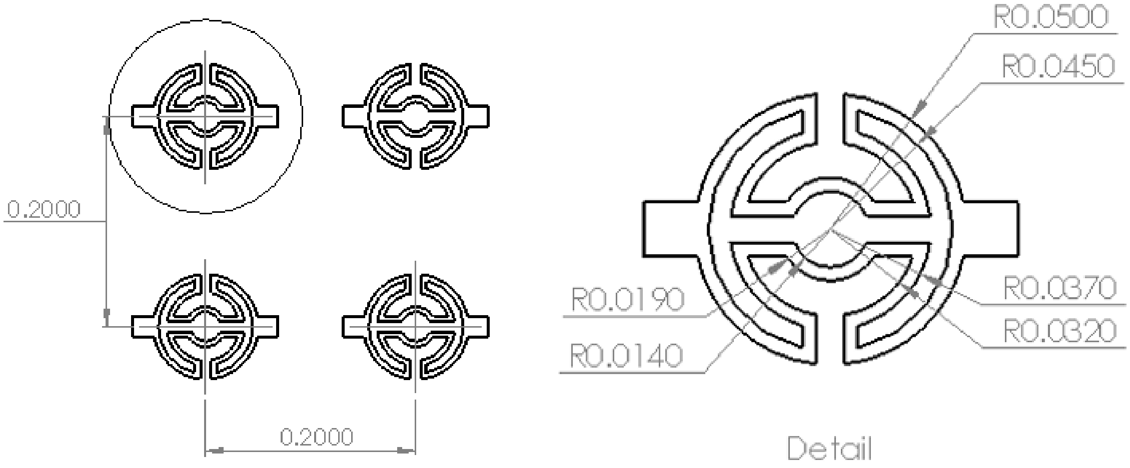

Figure 21-Final Design of Microheater Printing Array

The 4-heater array shown above was further evaluated for using the previously validated modeling. In this modeling, power consumption, heat distribution, and lead temperatures were all considered. This was to examine the effects of multiple heaters on these areas as compared to the previously optimized heater. The lead temperatures were approximated to ensure that they would not fail from agglomeration during usage of the device. The hypothesis of this work is that, if multiple heaters are working in unison they can have less uniformity, but generate power savings. Upon preliminary modeling, it was observed that the leads will not be subject to heat greater than 250^0C, that power consumption remains the same per heater, and uniformity is impossible to maintain across heaters of this geometry and spacing. 25 µm spacing was left for each lead in this study. This and the temperatures which the gold leads can withstand are the limitations preventing this design from being further optimized. 4.4 W total were required to heat all 4 heaters in the array to 600^0C in 1 *ms*. The results of heating distribution for the final model and the temperature ramp up to 600^0C in 1 *ms* are shown below in Figure *22* and Figure *23*.

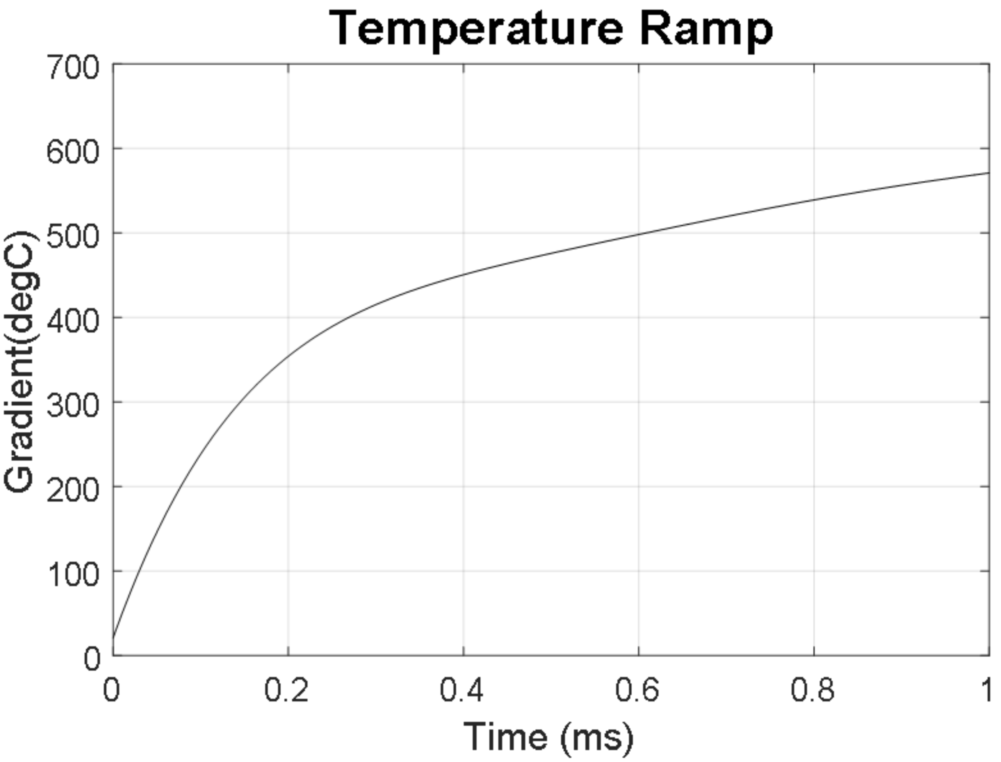

Figure 22-Time vs. Temperature Ramp of Scaled Heaters

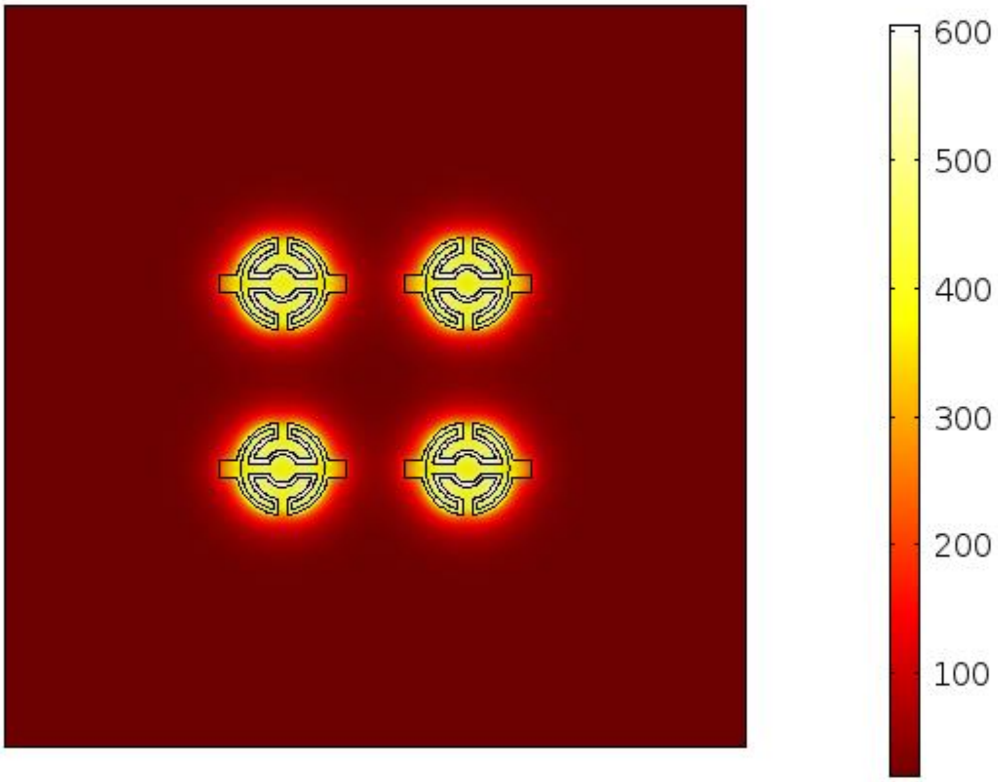

Figure 23-Simulation of Final Design of Four Microheater Array

3.1.5 Summary of Microheater Modeling

During this section, a numerical model was developed for modeling the operation of microheaters. A design was proposed, and it was optimized using a newly developed constrained particle swarm optimization algorithm. Stress and heat uniformity were reduced to 93.5 MPa and 89.7^{0}C. With the optimization results, an array of four microheaters was designed to show the scalability of this printing method. Each individual heater consumes 1.1 W of electrical power to reach a temperature of 600^{0}C in 1 *ms*, which achieved all of our design objectives set in the beginning of this chapter.

3.2 Fabrication of the Microheater Array

To fabricate the designed microheater array, established MEMS fabrication techniques were used with the equipment in the high density electronic center (HiDEC) at the University of Arkansas. Creating the microheater consisted of two uniquely designed masks. One of which was used for the resistive heating element fabrication and the other was used in the evaporation of conductive leads. Sixteen heating arrays were fabricated from these mask on a 4-inch diameter glass wafer supplied by Schott. Each array contains 4 heaters, an exploded view is provided in Figure 25. The design of the two masks are shown in Figure 25 and Figure 27 and the fabricated masks are shown in Figure 26 and Figure 28 respectively. Other features outside the arrays and leads are features used for alignment. All details of equipment operation and fabrication parameters are shown in Table 13 and a process flow of the entire process is shown in Figure *24*.

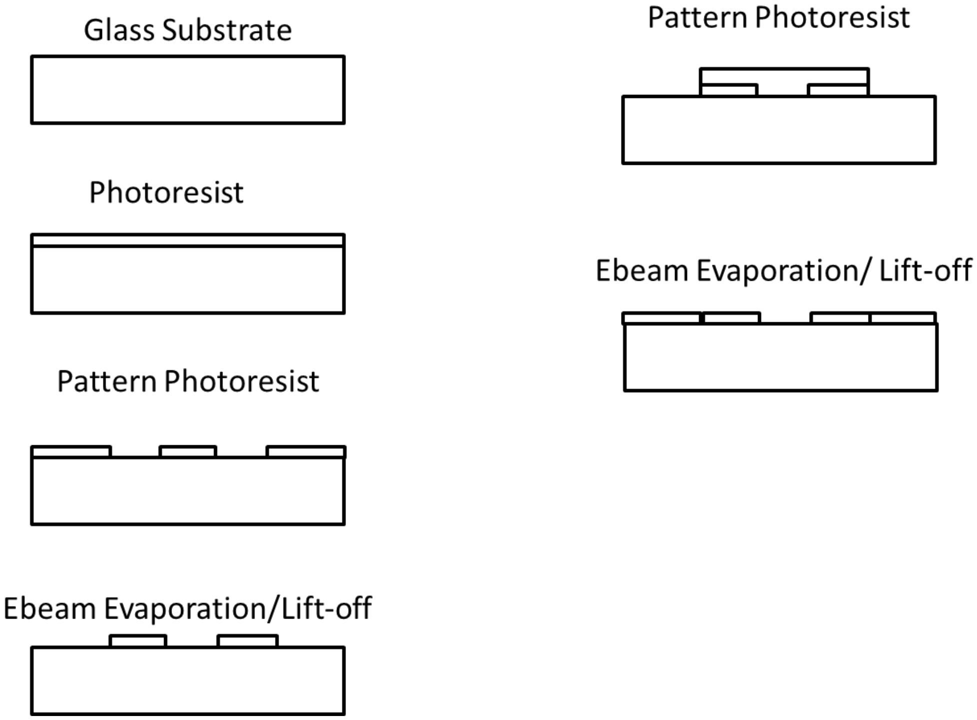

Figure 24-Process Flow for Fabrication of the Microheater Array

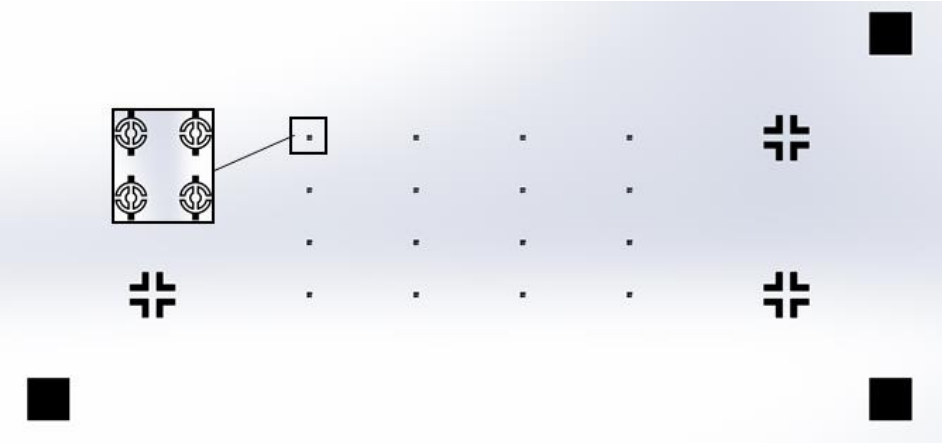

Figure 25- Digital Design of PhotoMask for Microheater Arrays

Figure 26-Microheater Array Photomask Pattern

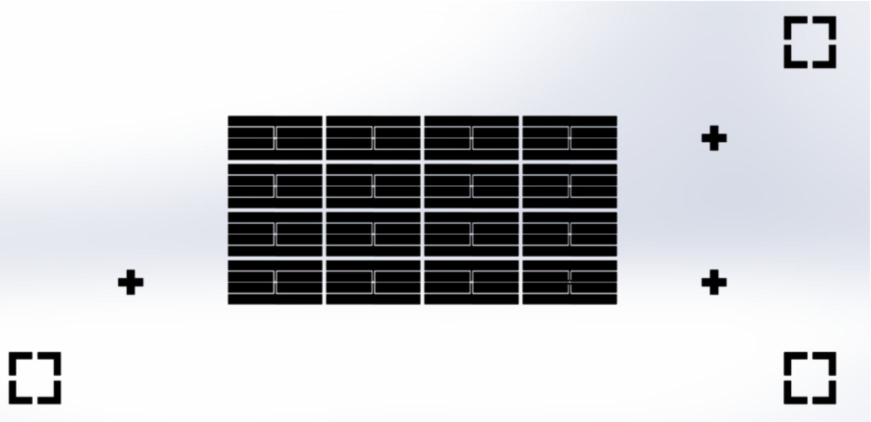

Figure 27-Digital Design of Photomask for Conductive Leads

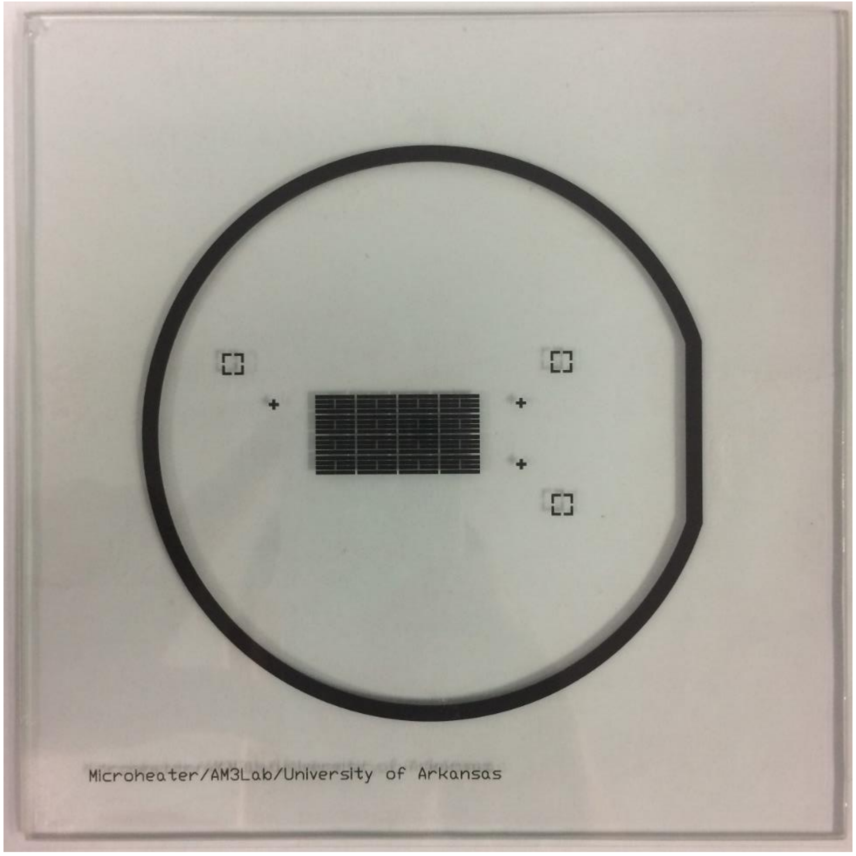

Figure 28-Leads Photomask Pattern

First, a wafer is cleaned before the fabrication starts. Cleaning was done by rinsing in DI water then quickly followed by a spin dry which will prevent water residues from being left on the wafer. One hundred percent acetone is spun on the wafer next to promote adhesion of the photoresist used. AZ series 5214E photoresist was then spun on at 4000 rpm for the 30s to create a 2 µm thick layer of resist. To ensure the resist is dry, an initial bake is performed at 88 °C for 45 seconds. The resist is then exposed for 6 seconds under UV light with the first photomask for heaters. To reverse the image of the positive photoresist and additional bake is done at 106^0C for 45 seconds followed by another exposure. Image reversal was used to create negatively sloped side walls to prevent peeling during liftoff stages of fabrication This second exposure uses a completely clear glass mask so that the entire wafer is equally exposed to the light for 45 seconds. The photoresist is then developed using AZ series 300 MIF developer. The pattern remaining on the wafer should be a reverse image of the microheater resistive element. Ti then evaporated onto the surface of the wafer using electron beam evaporation until a layer of 1500 Angstroms was formed. Finally, a lift-off process was used to remove the photoresist and metal on top of photoresist. Success of this step is heavily dependent on the type of photoresist removed. Positive photoresist was never successfully used in this fabrication. Positive resist enabled the metal patterns to connect with metals on top of the photoresist from depositions on the positively sloped sidewalls. To perform the lift-off of materials from the wafer, the wafer was submerged in acetone inside an ultrasonic vibration generator. The final product is a resistive element made of Ti on top of the glass wafer in Figure 29 where the image on the left is the digital design and the right is the actual fabricated device.

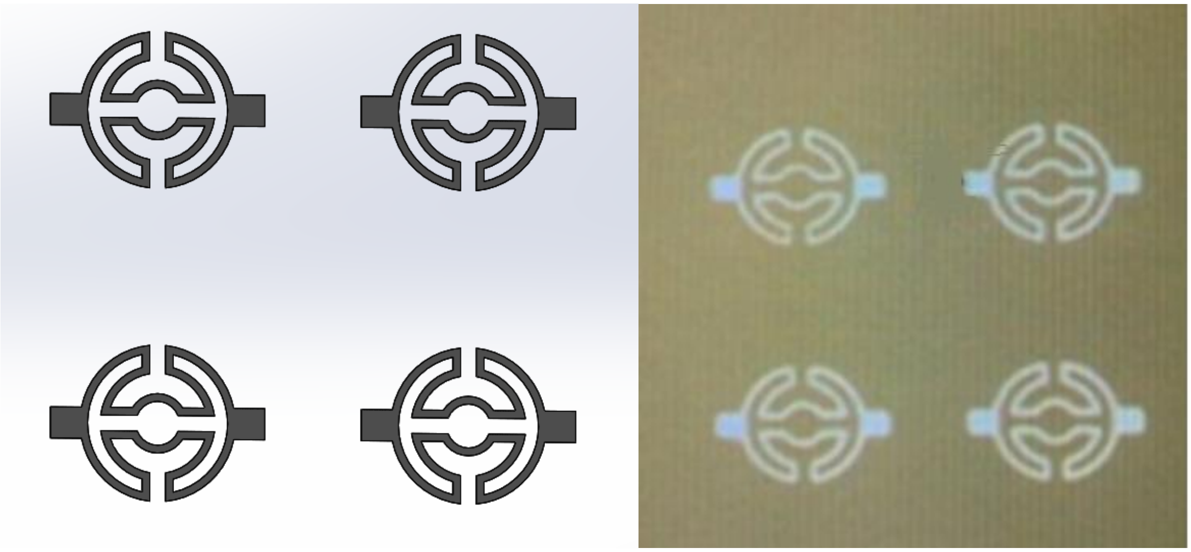

Figure 29-Ti Resistive Element or Heater on top of Glass Digital Design (Left) Physical Image (Right)

Table 13-Heating Element Fabrication Process Details

Step	Machinery	Process	Heating Element Process Description	Details
1	Semitool Dryer	Clean	Rinse wafer in DI water followed by spin dry	Speed: 2500 rpm spin Time: 3min
2	Specialty Coating Systems G3P-8 Desktop Coater	Spin Coat	Spin on Acetone (100%)	Speed: 500 rpm Dwell: 10s Ramp: 500 rpm/s
3	Specialty Coating Systems G3P-8 Desktop Coater	Spin Coat	Spin on photoresist AZ 5214-E	Photo resist AZ5214-E Step 1) Speed:1000 Time: 10s Ramp: 1000 rpm/s Step 2) Speed:4000 rpm Time: 30s Ramp: 1000 rpm/s
4	Electronic Micro Systems Ltd Model 1000-1	Bake	Hotplate Bake 88C	Temperature: 88C Time: 45 seconds
5	Suss Microtec MA150	Expose	Exposure from contact aligner w/ no aligns using heater mask	1000W UV Light Tower Time: 6 second exposure Energy: 60 W Intensity: 10 Power: 275W
6	Electronic Micro Systems Ltd Model 1000-1	Bake	Hotplate Bake 106C	Temperature: 106C Time: 45 seconds
7	Suss Microtec MA150	Expose	Exposure from contact aligner w/ no aligns using a clear mask	1000W UV Light Tower Time: 45 second exposure Energy: 450 W Intensity: 10 Power: 275W

Table 13-Heating Element Fabrication Process Details (Cont'd)

Step	Machinery	Process	Process Description	Details
8	AmeriTrade Wet Bench	Develop	Submerge wafer in developer of AZ MIF 300 and immediately rinse and dry	Time: 45 seconds
9	TeleMark/Edwards	E-beam	Evaporate Ti	Thickness 1500 angstroms Deposition Rate ~1.2 A/s Final Temp. 30^{o}C
10	Branson 1800 Ultrasonic Bath Model CPX1800H	Lift-off	Submerge wafer in acetone and place in ultrasonic bath to run agitation	Time: 5 min Agitation: Sonic

The same process described above was used to create the conductive leads with a few minor exceptions. These were: 100 Angstroms of Ti for adhesion and the conductive element was 1000 Angstroms of Au. In addition, a mask for the conductive leads was used and aligned with the existing heater geometries. The final result of these processes is in Figure 30 where the figure on the left is the digital image and the right side shows the actual fabricated device. The process details are in Table 14.

Table 14-Conductive Lead Fabrication Process Details

		Conductive Leads		
Step	Machinery	Process	Process Description	Parameters
11	Semitool Dryer	Clean	Rinse wafer in DI water followed by spin dry	Speed: 3600 rpm spin Time: 3min
12	Specialty Coating Systems G3P-8 Desktop Coater	Spin Coat	Spin on Acetone (100%)	Speed: 500 rpm Dwell: 10s Ramp: 500 rpm/s
13	Specialty Coating Systems G3P-8 Desktop Coater	Spin Coat	Spin on photoresist AZ5214-E	Photo resist AZ5214-E Step 1) Speed:1000 Time: 10s Ramp: 1000 rpm/s Step 2) Speed:4000 rpm Time: 30s Ramp: 1000 rpm/s
14	Electronic Micro Systems Ltd Model 1000-1	Bake	Hotplate Bake 88C	Temperature: 88C Time: 45 seconds
15	Suss Microtec MA150	Expose	Align and exposure with leads mask	1000W UV Light Tower Time: 6 second exposure Energy: 60 W Intensity: 10 Power: 275W
16	Electronic Micro Systems Ltd Model 1000-1	Bake	Hotplate Bake 106C	Temperature: 106C Time: 45 seconds
17	Suss Microtec MA150	Expose	Exposure from contact aligner w/ no aligns using a clear mask	1000W UV Light Tower Time: 45 second exposure Energy: 450 W Intensity: 10 Power: 275W

Table 14-Conductive Lead Fabrication Process Details (Cont'd)

Step	Machinery	Process	Process Description	Parameters
18	AmeriTrade Wet Bench	Develop	Submerge wafer in developer of AZ MIF 300 followed by immediate rinse and dry	Time: 45 seconds
19	TeleMark/Edwards	E-beam	Evaporate Ti+Au	Thickness 1500 angstroms Deposition Rate ~1.2 A/s Final Temp. 30^{o}C
20	Branson 1800 Ultrasonic Bath Model CPX1800H	Lift-off	Submerge wafer in acetone and place in ultrasonic bath to run agitation	Time: 5 min Agitation: Sonic

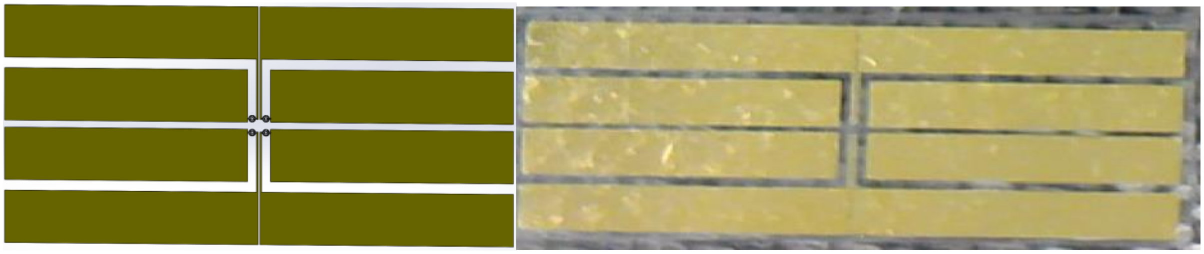

Figure 30-View of Heaters with Conductive Leads Digital Image (Left) and Image from Microscope (Right)

3.3 Packaging Design and Prototyping

Packaging design includes how the array of microheaters are attached to external circuitries and serves as a structural device for housing the microheater array. The design and fabrication of the packaging and electrical connections of the microheater in this section utilized a non-typical method of fabrication because of funding and time limitations. This non-typical method was necessary because of the close proximity of the SRS system to the objects to be sintered. The non-typical fabrication also eliminated additional fabrication steps to save time and money. It is not ideal but is sufficient for low production numbers for proof of concept. In the design, a PCB was used as the main packaging housing with no protection from the external environment. The PCB was used to create surface mount device (SMD) pads to mount the heating array. Wire bonding and conductive epoxy are used to form the electrical connections between the SMD pads and the microheater leads. With the entire packaging design completed, this section will then go into the prototyping of this device. The prototype of the packaging is also, for the purposes of this printer, considered the main printhead device.

3.3.1 PCB Design

The PCB packaging offers essential components to provide digital control of the microheaters from a microcontroller with a serial connection. The resistance of heaters is estimated from the geometry defined in the optimization above and existing literature to be ~213 ohms. This was found using (3. To ensure heating and resistive losses are focused on the heater, the resistance of the external circuitry is desired to be much lower than the heater resistance. A PCB was used with copper traces and electroless nickel immersion gold (ENIG) surface mounting pads. Using these materials with a thickness of 10 mil traces makes the resistance less than 1 ohm making the impacts nearly negligible on the power losses and with no external heating. This design is a device which utilizes screw mounts which can be used for preliminary testing of the heater functionality as well as full incorporation into the printing system. The design of the packaging device is seen in Figure 31.

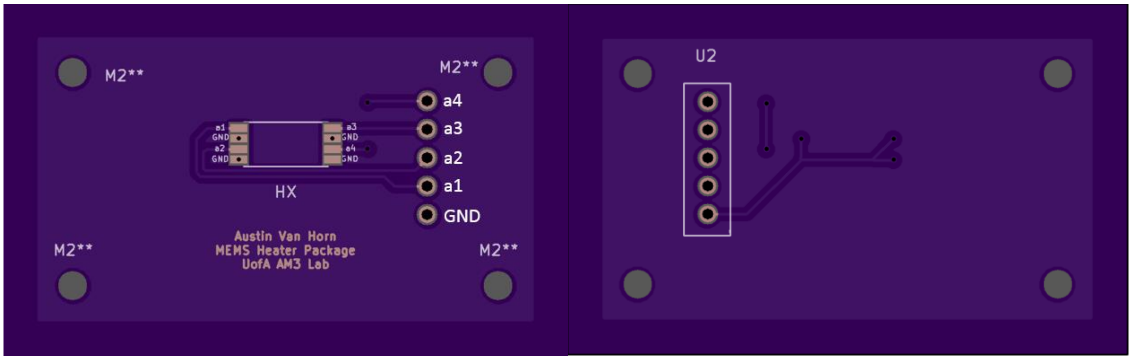

Figure 31-PCB Microheater Packaging with Front (Left) and Backside (right) Views

The devices and features which will be made operational on this board are as follows:

- M2 mounting screws for mounting the PCB to the print head and other testing setups
- a1, a2, a3, a4 are power connections to the 4 heater array
- GND is the ground pin
- HX is the surface mount pads and heater location

3.3.2 Electrical Connections

There are two essential components to the electrical connections. One is the conductive paste which combines the wire to the conductive leads on the heater and the other is the wire bonding which enables connection to the PCB. Conductive paste was used because the conductive leads were too thin to allow for wire bond attachment. A schematic is provided in Figure 32 for a visual representation of the design. In this design, heaters are connected to the evaporated part on conductive leads, conductive leads are epoxied to a 5 mil aluminum wire, and the aluminum wire is wired bonded to the ENIG layer on a PCB shown in Figure 32.

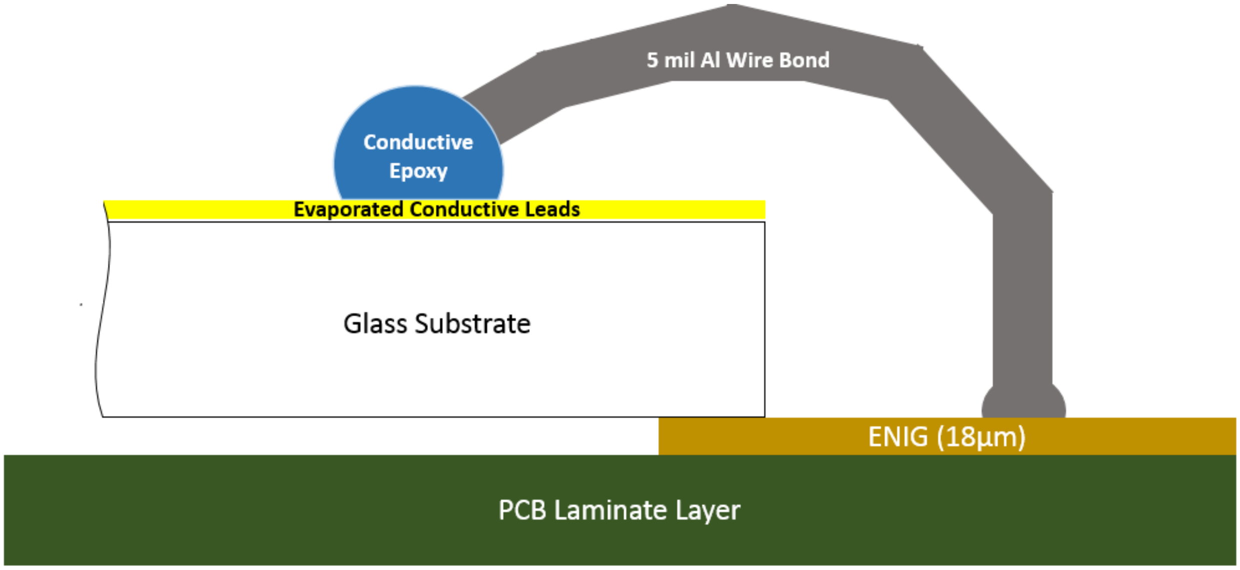

Figure 32-Configuration of Electrical Connections

The evaporated leads made of gold in the previous design is a layer of 1000 Angstroms thick gold on top of a 100 Angstrom Ti base for adhesion. This design was chosen primarily for fabrication purposes which will be discussed in the device fabrication, and also by the fact that it offered low resistance. Table shows the resistivity of the materials used, which result in a negligible electrical loss from these designs and materials.

Table 15-Review of Resistivity for Electrical Connection Materials

Material	**Resistivity**	**Units**
Epoxy	4.00E-05	ohm-cm
Al Wire	2.65E-05	ohm-cm
ENIG	6.00E-08	ohm-cm

3.3.3 Prototyping

Fabrication of the prototype is described in two main steps. The first step is creating the microheater based on micromachining methods. Then the microheater was used in the overall assembly and packaging of the heater and its components. In this process, equipment was used specifically by the equipment available in HiDEC at the University of Arkansas.

Assembly and packaging are performed by standardized processes in the exception of the attachment of the wire bonded aluminum wires to the microheater device. The first step in the assembly was dicing the wafers. Sixteen different arrays were fabricated on the glass substrate initially, but only 1 array can be used in each PCB packaged assembly. This was performed by using a 4 mil dicing saw. Once the heaters were cut out, they could be super glued to the PCB. Loctite super glue was used and heaters were placed so that glue was only under the part of the heater suspended by the ENIG is shown in Figure 32. Next ultra-sonic bonding is used to bond a 5 mil aluminum wire to the ENIG pads on the PCB, and the leads are extended 1 mm above the pads straight into the air. Then, the wires are manually folded onto the conductive leads and conductive epoxy is manually applied from the wires to the heaters under the vision of a microscope to ensure accuracy in placement. The final process is a curing process which dries the epoxy and ensures conduction is achieved in the epoxy. This was done in an air tight oven at 160^0C for 5 minutes. To ensure the material is cured, a test drop of epoxy is placed on the PCB in the oven with the microheater and packaging devices. The test drop was probed to ensure the material was hardened and conductive before removing. A final view of the fully assembled microheater to PCB with electrical connections is in Figure 33. Detailed steps and relevant parameters are listed in Table .

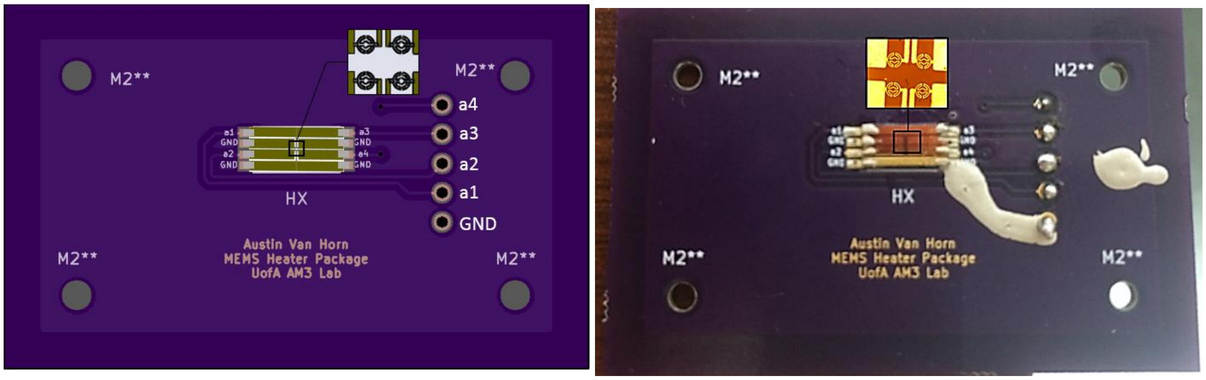

Figure 33-Final Assembled Microheater, Packaging, and Electrical Connections Digital Design (Left) Physical Image (Right)

Table 16-Assembly and Packaging Fabrication Process Details

		Assembly and Packaging		
Step	Machinery	Process	Process Description	Parameters
21	Kulicke and Soffa Industries Model 928-10	Dicing	Dicing wafer w/ dicing saw	Spindle Speed: 25K rpm Blade Size: 4 mil thickness Single Cuts
22	Manual	Super Glue Die	Glue and align die leads w/ heater	Brand: Loctite
23	Orthodyne Model 10	Wire bond	1mm vertical wire bond to PCB	Diameter: 5 mil Material: Aluminum
24	Manual	Fold Wires	Manually fold wires under microscope with tweezers	
25	Manual	Epoxy Leads	Use sharp needle to apply fine amounts of epoxy	Brand: Epo-Tek Epoxy Technology Type: P1011/ 1 oz
26	Fisher Isotemp Vacuum Oven Model 282	Cure	160C 5 min checking cure check	Vacuum level: 15mmHg Time: 5 min Temperature: 160 C Purge gas: N2

3.3.4 Summary of Packaging Design and Prototyping

Packaging is a highly studied area of development, as was shown in Chapter 2. Packaging is part art and part intensive understanding of physics. In this design, all designs were made out of simplicity to offer as little resistance losses as possible while also being economically affordable. The PCB structure also offers ease of integration into many different operational scenarios. Having a flexible PCB design lets us use the same design for testing the heater as will be implemented in the print head of the new SRS printer.

3.4 Testing and Characterization

Testing is an essential part of the fabrication process as well as quantifying the operation after the entire device is fabricated. Testing was broken down in to two main sections. The first section is in-situ testing during fabrication, and the second is post-testing after fabrication. During the in-situ testing, testing will be performed after each step of the fabrication process. This is a necessary method of testing to ensure each fabrication process worked as intended. During the post testing, the heater needs to be tested to ensure its functionality. The various methods for both of these sections will be discussed in the following sections.

3.4.1 In-Situ Testing

At multiple steps in the fabrication process, different techniques were used to evaluate whether the fabrication process was successful. During the microheater fabrication, all photolithography processes were always checked under a microscope. In this process, under close inspection, there is a clear boundary which exists to differentiate between what is photoresist and the other materials. This ensured that the photoresist was not over/under developed, that all features existed, and alignment was correct. This took place in between steps 8 and 9 and between steps 18 and 19 from Table 13 and Table for fabrication of the heater and the conductive leads respectively. Below in Figure 34 is a photo confirming that the shapes fully developed and were to the specified size.

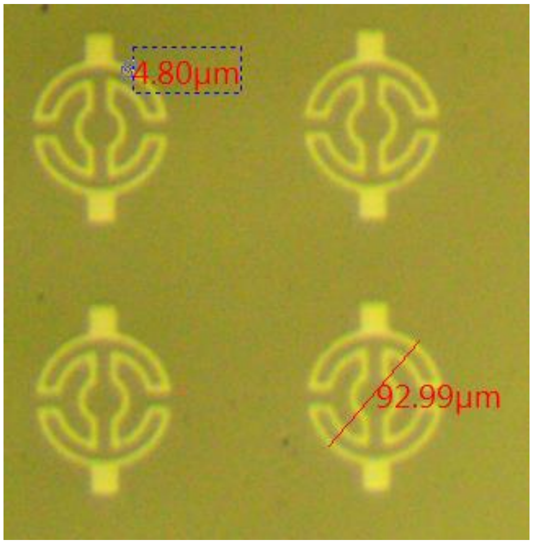

Figure 34-Confirming Photoresist

This same visual inspection method was used after steps 10 and 20 in Table 13 and Table respectively. After the lift-off process is performed, it is important to check to make sure the geometries formed as you intended. There is the possibility of adhesion issues and peeling which could occur, but have not been experienced in this method of fabrication discussed above. For steps 10 (in Table 13) and step 20 (in Table), additional testing also needed to be performed. Microheaters are electronic devices, and it is important to check their conductivity as well as the resistance of the devices in the circuit. The process of checking the resistive elements for continuity tended to damage the heaters, so this process was only performed for two heaters in two different arrays. Once the larger conductive leads were added after step 20 (in Table), electrical characterization could be obtained by measuring the resistance of the heaters without damaging the heaters. The Au evaporated conductive leads provided negligible, less than 1 ohm, of resistance making this measurement accurate even with the additional materials through which the measurement is made. Five microheater arrays (out of 16 arrays on one wafer) were successfully obtained. The yield rate is 31.25%. Design specific details were that the micro heaters were structurally intact and the resistance was within 10% of the estimated 213 Ω resistance.

3.4.2 Prototype Testing

Post testing after fabrication enables us to determine whether or not the entire device will be functional during the printing operation. During this operation, the heat should travel upwards due to convection arising in the air. This eliminates the possibility of overheating any equipment below the resistive element, such as the packaging. It also creates ease of setup, due to the ability to plug the electrical connections straight into a breadboard and form the remaining testing setup around it. An enclosure was used which encompassed the entire setup to prevent forced convection which could arise from the various movement of people, AC system, etc. The external circuitry requires an external power supply to power the microheater and an additional sensing device. Power is provided by a 12V variable DC power supply and an Arduino Mega 2560 microcontroller was used to precisely control the power supply.

3.4.2.1 Camera Testing

Initial post fabrication testing was performed using a 12V power supply and Arduino controls. The circuitry used is shown in Figure 35.

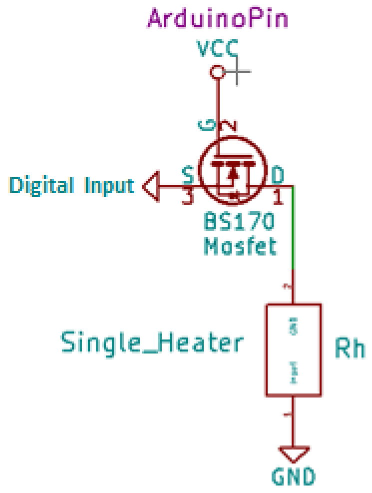

Figure 35-Testing Control Circuit to a Single Heater

During this test, a 10 second electrical pulse was applied to the heater to ensure it reached its maximum temperature. The VCC was set to the maximum 12 V. A ME320 series AmScope microscope was used to visualize the heat being applied to the heater. This microscope has a frame rate of 30 Hz. This rate corresponds to a 33 *ms* thermal response time of the heater. Based on this applied voltage the camera could not capture the heating as intended. However, this is not unexpected to be due to the frame rate. The heater was expected to heat to 600^{0}C in less than 1 *ms*. This would not have been capable of being captured during 1 frame. The inability to record data was likely due to a lag in the serial connection updating to the computer. The inability to record data was observed through a noticeable delay in the images put on the screen when moving the microscope. However, failure was observed in the heater, which previously has only been observed happening at temperatures in excess of 650^0C according to literature [16], from blistering of the filament. This can be seen from the top left heater in Figure 36.

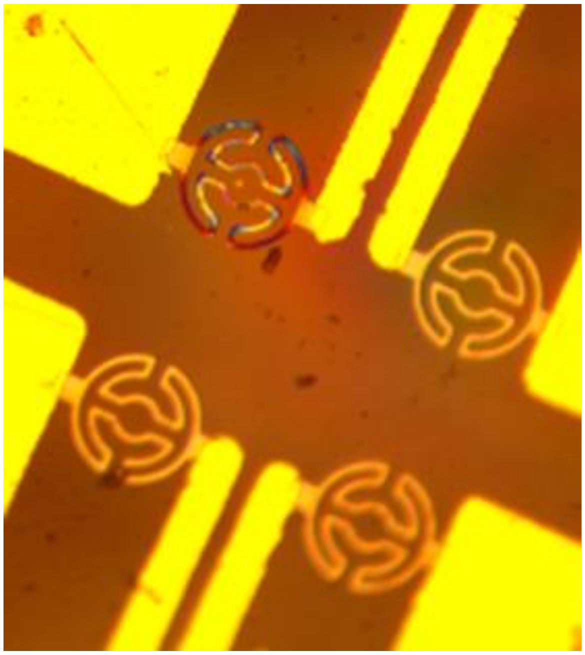

Figure 36-Burnt Out Heater

3.4.2.2 Thermocouple Testing

A second test was conducted to see if the thermocouple could measure a change in temperature from the heater. In this test, a voltage supply was applied directly to the heater without any other devices in the system. There also would be no feedback, nor any controls determining when and how long the DC voltage would be applied. This was a test intended to destruct the heater in order to determine the temperature limits of its operation by use of an external measurement system. The thermocouple used was much larger than the microheater, roughly 200um in diameter at the tip, which was known to likely cause problems with the heat transfer and delay the thermal response time.

In this setup, Figure 38, a MAX6675 IC device was used to measure the temperature. This provided direct feedback from the thermocouple to the Arduino serial feed. This system was only used for monitoring and did not get used for feedback controls. The thermocouple is denoted as TC+ and TC-. The outputs SO, CS, SCK, VCC, and GND are all outputs to Arduino which are used in the programming of the microcontroller. The SO, CS, and SCK are digital outputs required for the device to be functional. The circuitry can be seen in Figure 37. This device uses temperature change to drive a thermoelectric effect where the voltage change can be measured.

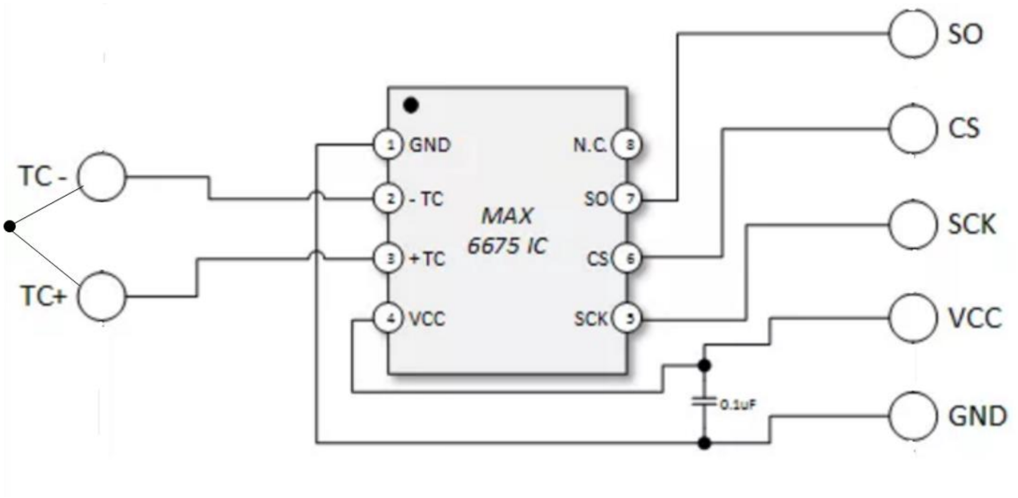

Figure 37-Thermocouple Setup

To accurately place the thermocouple close to the microheater, the Type K thermocouple was attached to a micrometer and a camera was used to accurately place the device, approximately 5 um away from the heater. A picture of this setup is shown in Figure 38.

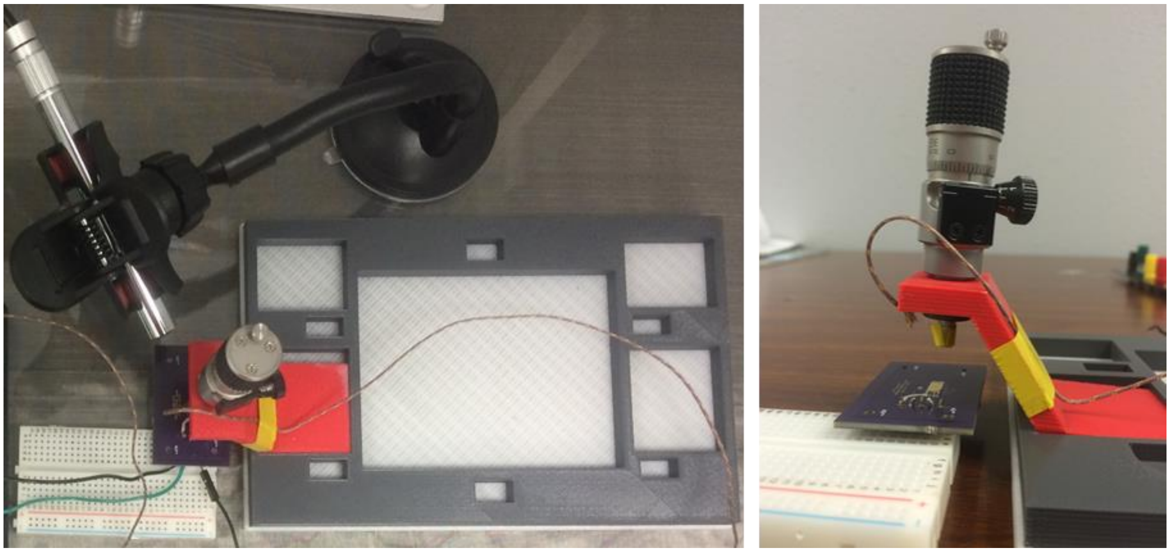

Figure 38-Thermocouple and Camera Setup for Test 3

It was predicted that 8V would cause the heater to heat up with 10 *ms* from simulation, but is not entirely accurate for this scenario due to most of the heat being transferred into the highly conductive metals of the thermocouple. This system setup resulted in temperature measurements of up to 44.5^{0}C from the thermocouple, and temperatures were gradually increasing when the heater ceased operation.

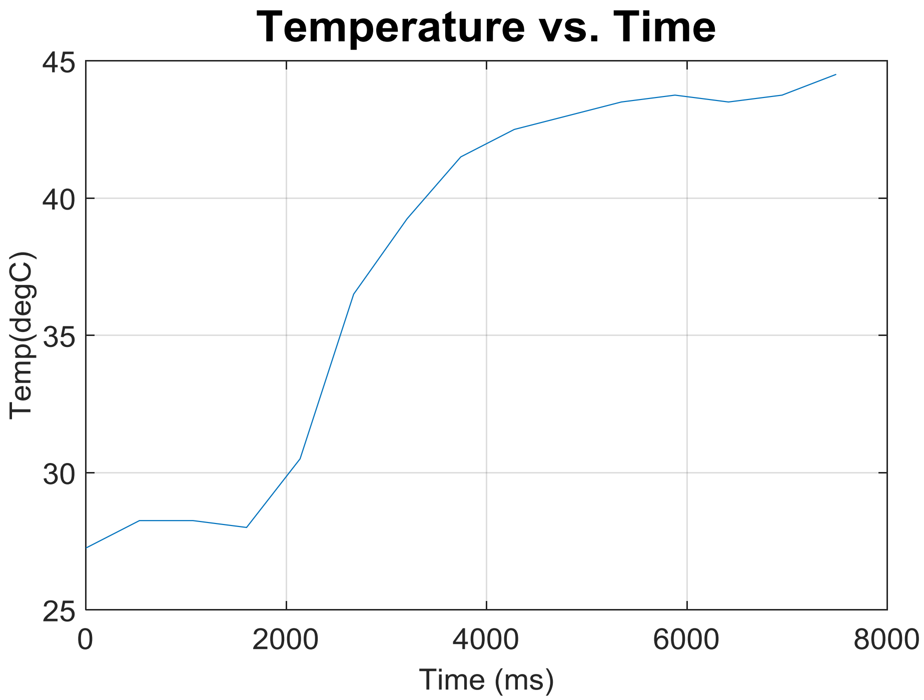

Figure 39-Plot of Temperature vs. Time Measured by Thermocouple

From these results, it can be interpreted that the heater increases in temperature much quicker than the thermocouple can measure. It is confirmed that heat is being transferred away from the heater, but cannot be accurately measured using this particular thermocouple.

3.4.2.3 Internal Circuitry Feedback Testing

A third heating test was performed using circuitry that can also be used in the printing scenario. This setup required a device to be able to serially communicate with the heater. To accomplish this, Arduino was used with a series of MOSFET transistors that only would supply power to the heater when a voltage was applied to the gate of the transistor. This circuitry can be seen in Figure 40.

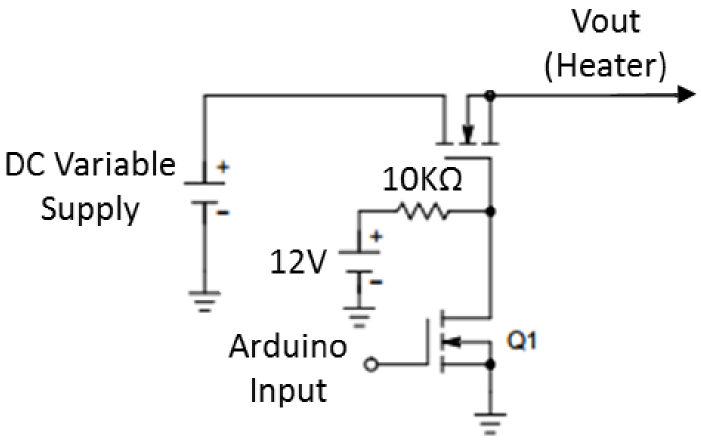

Figure 40-MOSFET Power Supply Control

A feedback system was also implemented to protect the microheater from reaching over 600 °C based on the change of the resistance of the microheater. The heater will be turned off if the resistance of the microheater indicates that the microheater temperature has gone above 600 °C based on a pre-calibrated temperature-resistance relationship. This relationship works by using an analog input which corresponds to the resistance to calculate the temperature change. The circuitry utilized a LM741 op-amp setup in a unity gain. This prevented excessive currents from damaging the Arduino because of the analog input. The setup of the circuitry was shown in Figure 41. Small capacitors in the system enable quick ramp up times <<1 *ms*, but most of the time delay is in the Arduino serially communicating the signal from the Arduino to the computer which operated on a time scale of 40 *ms* – 80 *ms*.

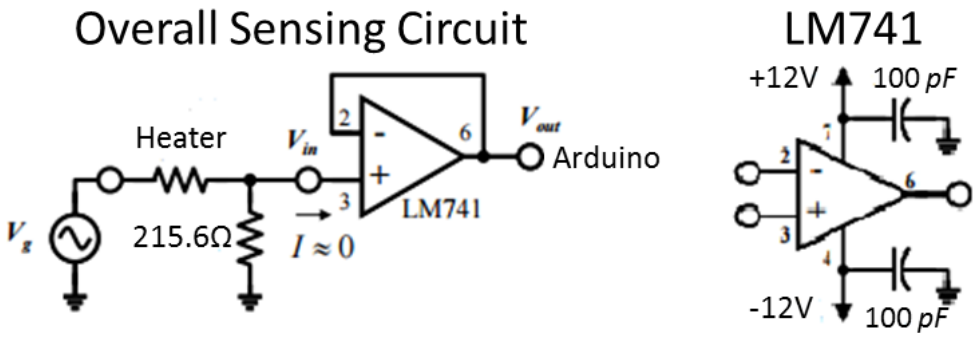

Figure 41-Feedback Circuitry w/ LM741 Op Amp

In addition to this circuit, the thermocouple which was used in " 3.4.2.2 Internal Circuitry Feedback Testing" was used again for this circuit with a faster analog sampling rate to have additional validation. The full setup can be seen in Figure 42. Here a camera was added to the circuit providing visual recognition of the heater and the thermocouple placement.

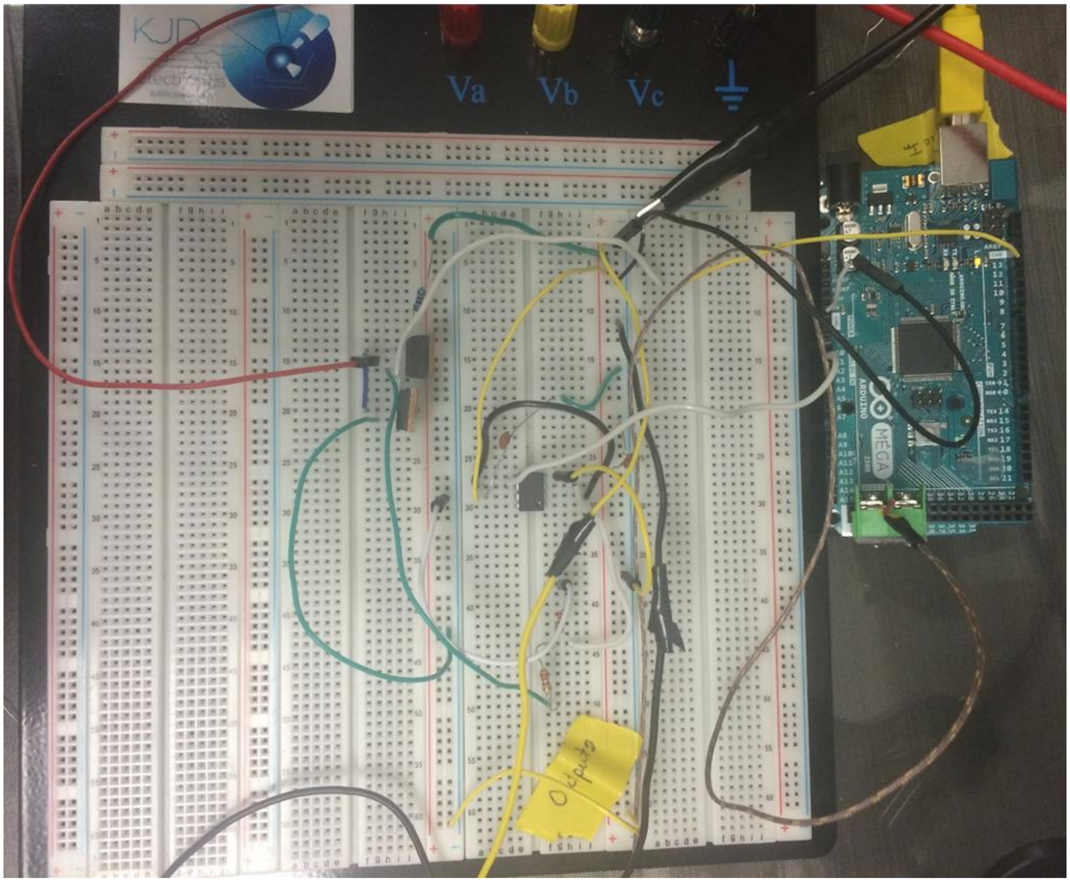

Figure 42-Full Circuitry Setup

The results of this testing were done by setting the DC voltage output to 5V supplied directly to the heater. Resistance was recorded to determine the temperature. The initial resistance of the heater was 195.6 Ω and the maximum resistance was 313.2 Ω. It was found that the resistance did not lower back to its original resistance. The resistance returned to 266.8 Ω instead of 195.6 Ω. The temperature was found by post processing the resistance data and using the temperature coefficient of resistance (TCR) of Titanium. The temperature was found to have reached a maximum of 693.74^{0}C. A corresponding resistance versus time plot was created for this test. However, it appears that the feedback system from serial communication is not quick enough to capture much data. This is due to the heater ramping up to the maximum temperature quicker than the analog signal can be fed to a computer. In the test, a delay is noticeable from when the system is started to when the heater ramps up in temperature. The heater then immediately ramps up to its intended temperature. This is shown in Figure 43.

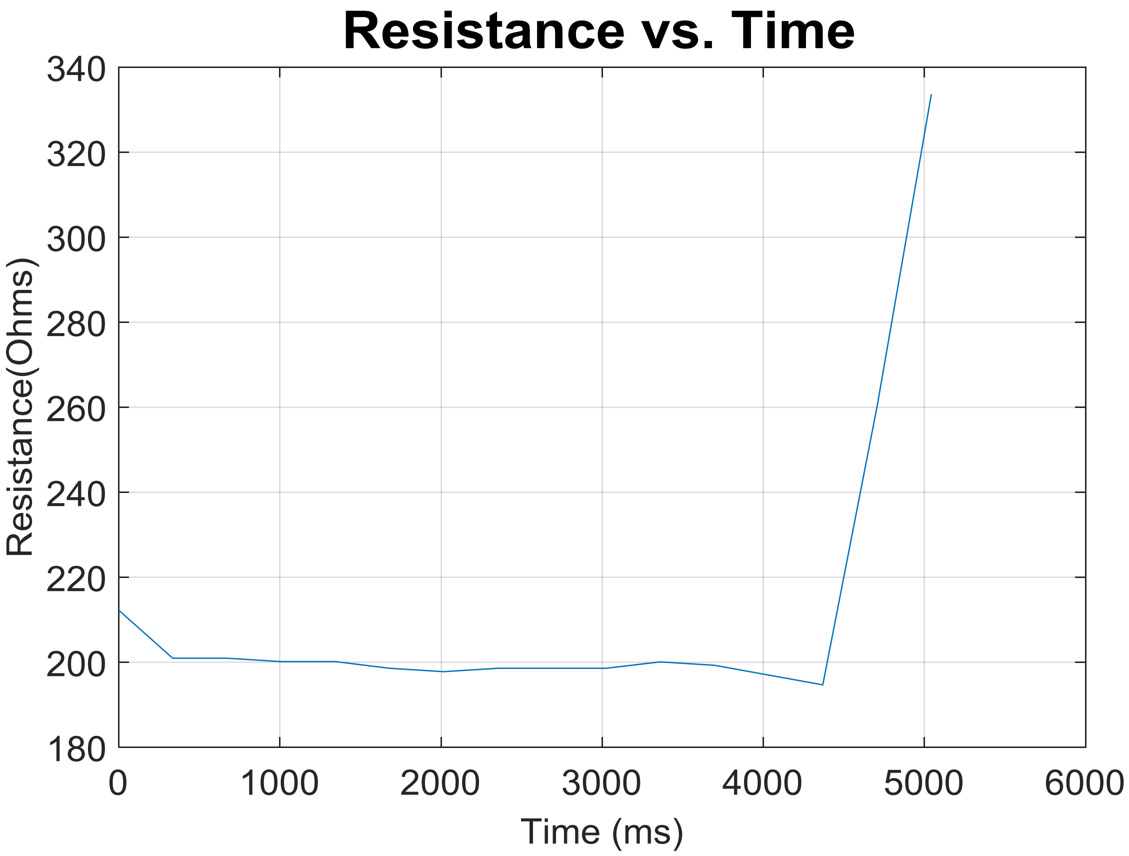

Figure 43-Resistance vs. Time of the Microheater Feedback System

In this testing, a thermocouple and the internal feedback circuitry were used to measure the temperature of the microheater. However, the thermocouple did not work in this testing. Though it wasn’t stated in literature on the device, the MAX 6675 was not capable of recording temperatures faster than 300 milliseconds. The sampling rate in this testing was set at 50 – 80 milliseconds, which is the fastest the Arduino could serially communicate. For this reason, data was recorded for the internal circuitry feedback, but results did not exist for the thermocouple measurements.

3.4.3 Summary of Testing and Characterization

During Prototype Testing, heaters were tested individually to see if they operated the way the numerical modeling predicted. Based on analog feedback, which enabled us to interpret the resistance of the heaters, the heaters reach high temperatures of greater than 600^{o}C. The equipment used, however, was not capable of measuring the thermal reponse sufficiently fast. It is only known that the resistance change should be equivalent to a system which is operating at the predicted high temperatures. A thermal couple was also used in the testing of the system. It was confirmed that the microheater provided substantial amout of heat to heat a thermocouple which was much larger in size than the microheater. The temperature was reported rising from room temperature up to 44.5^{o}C. Results of testing confirm that the heater does work successfully, and this should be an adequate device to add to the prototype of the overall printing system.

Chapter 4 SELECTIVE RESISTIVE SINTERING PRINTING SYSTEM

Selective resistive sintering as a printing system will be discussed in this chapter. Relevant parameters of the printing system will be evaluated by numerical modeling. Numerical modeling gives insight to whether the method is a viable method, and what operational parameters (temperature, air gap, material properties, etc.) are required to for it to be viable. A focus will then be given to necessary equipment design to enable the printing system to be a viable method.

4.1 Numerical Proof of Concept

In this section, we focus on two primary materials for sintering. The first is a polymer based Nylon 12 from 3D Systems, and the other is a silver nano particle solution by NovaCentrix (JS-B40G). The ultimate objective is to numerically validate that the resistive heating source previously designed can provide an adequate heat to elevate temperatures to sintering temperature in one millisecond. Temperatures will be measured at the surface of particles being sintered to make this determination. In this validation, we will feature a series of different numerical simulations which will define the details of operation. Upon definition of materials, boundaries, and meshes, simulations can then be performed to assess the validity and define the operation parameters. Relevant parameters that will be investigated in this study, will be the air gap, temperature on the surface, and sintering resolution based on a 1 *ms* heater ramp and 2.1 W power operation.

4.1.1 Initial Setup for Simulations

The numerical model of the microheater previously described in Chapter 3, is used again for simulation for the proof of concept of the printing system. This design includes a Schott’s glass substrate with a Titanium resistive element and gold conductive leads. The model is a 3D model which models the resistive element as a shell. In this study, a convection coefficient is not assumed as was previously done in Chapter 3. This is accounted for by modeling the medium of air as a fluid which heat conducts between the heater and the material being sintered. The material being sintered is a thin layer of material placed on a glass substrate. The overview of this setup can be seen in Figure 44.

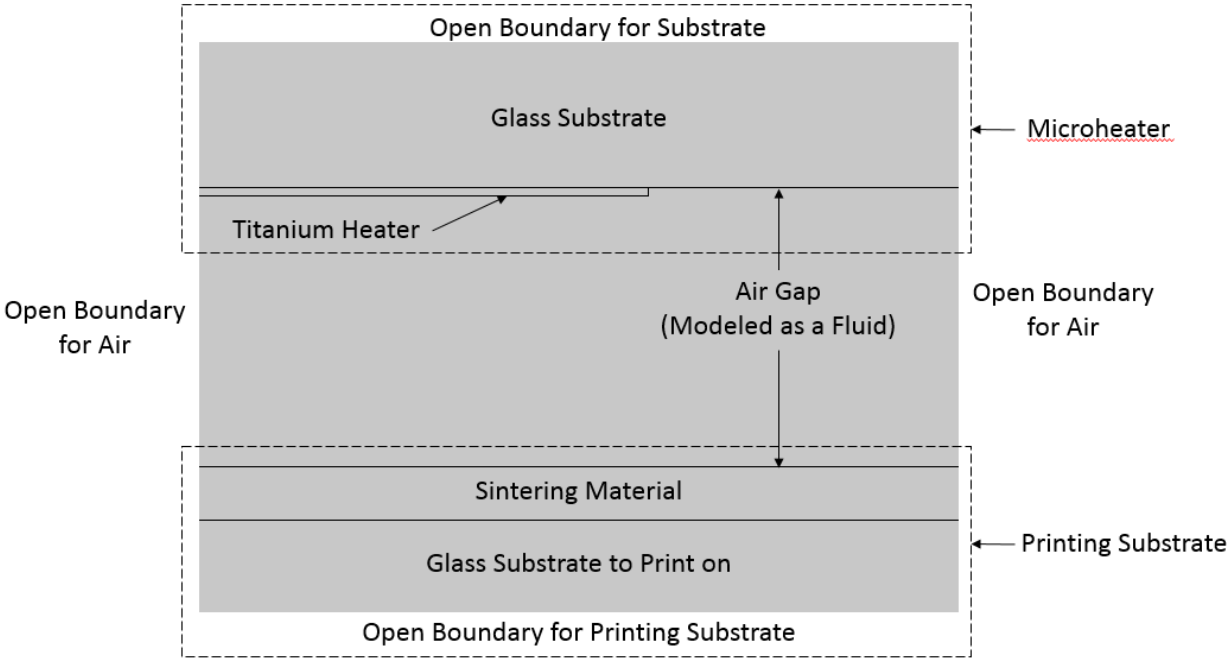

Figure 44-Modeling Setup for Proof of Concept

This system would create an extensively large model if modeled in its entirety. To simplify the numerical model, open boundaries have been used where boundaries would be continuous. The initial room temperature in the simulation is 20^{0}C. Material properties are the same for the microheater part of the simulation. Air has material properties that are temperature dependent, which are modeled based on known relationships [119]. The glass substrate being printed on is Pyrex 7740 glass. The additional material properties used at room temperature are in Table .

Table 17-Material Properties Used for Simulation

Summary	Pyrex-7740	Air
Electrical Resistivity (Ω*m)	1.26E+06	-
Thermal Conductivity (W/m*K)	1.18	.0257 or >
Specific Heat (J/kg*K)	753.12	1.005 or >
Density (kg/m^3)	2230	1.225 or >
Temperature Coefficient of Resistance (1/K)	-	-
Young's Modulus (Pa)	1.16E+11	-
Poisson's ratio (1)	0.321	-
Thermal Expansion Coefficient (1/K)	8.60E-06	-
Function	Substrate	Conducting Medium
Thickness (μm)	550	0 to 50

4.1.2 Sintering Conditions

Sintering is an Arrhenius thermal process and the sintering rate is exponentially related to the sintering temperature. In traditional oven-sintering of silver nanoparticles, it usually takes minutes to sinter at 150 °C. To achieve our objective of millisecond sintering, the sintering temperature needs to be significantly higher. K. A. Schroder from NCC Nano LLC have studied the sintering conditions for achieving millisecond sintering in a photonic sintering process of silver nanoparticles [115]. In the photonic sintering process, a strong pulse of light is applied and the energy is absorbed by the silver nanoparticles and the substrate, which leads to the temperature rise of both the silver nanoparticles and the substrate as shown in Figure 45 [114]. The surface temperature reaches over 1000 °C in less than 1 millisecond and quickly cools down. Their results show good sintering quality can be achieved under this condition. It is not clear from their study whether good sintering quality can be achieved at a lower temperature (e.g., our target temperature of 600 °C) in 1 millisecond. Without a clear target on the required sintering time for our proposed SRS process, we will use 10 milliseconds as a target in our evaluation.

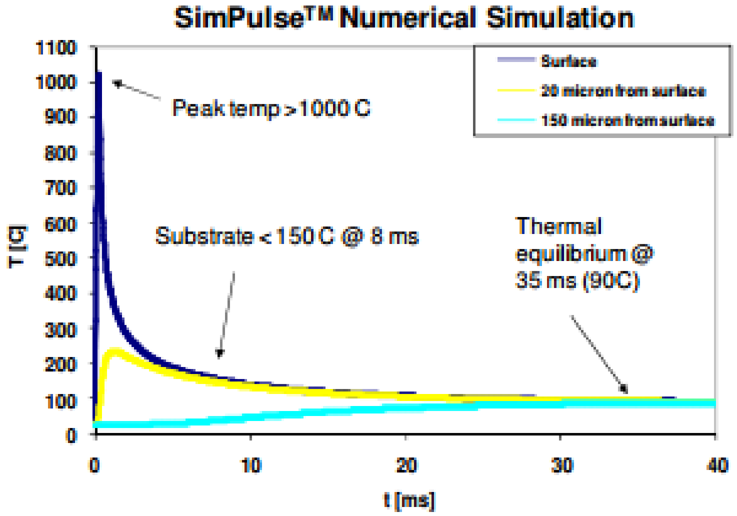

Figure 45- Temperature Change of Silver Nano-Particles and Substrate in Photonic Curing [114]

4.1.2.1 Effective Thermal Conductivity

Modeling the thermal conductivity of the powder particles is an essential aspect of accurate prediction. The combination of densely populated nano-particles and air can be treated as a bulk thin film material with an effective bulk thermal conductivity, which has been shown to be accurate in simulations [116-118, 125]. Equation (1) can be used to calculate an effective thermal conductivity of the silver nanoparticles. To ensure the materials were being modeled properly Equation (1) was used to calculate the thermal conductivity of the material being sintered. In Figure 46 data is recorded from experimental and analytical calculation of data.

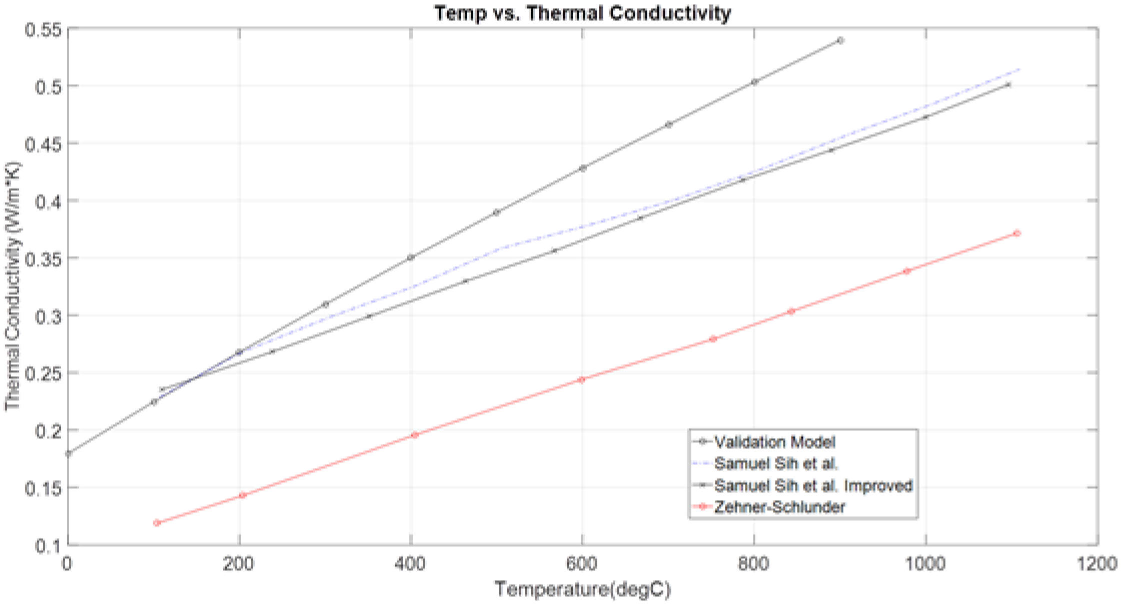

Figure 46-Temperature Dependent Thermal Conductivity of Powders

Model Samuel Sih et al. Improved is the improved replication of data performed by Samuel Sih et al. which is an improved version of the Zehner-Schlunder equation, and the exact parameters were used with changes to the thermal conductivity of the powders [117]. The powder in this case was Ag, which has a thermal conductivity of 406 W/m*K. This same equation will be used to predict the bulk thermal conductivity of silver nano-particles in air to replicate the heat transfer in the printing scenario. The thermal conductivity of the silver particles based on this equation is shown in Figure *47*.

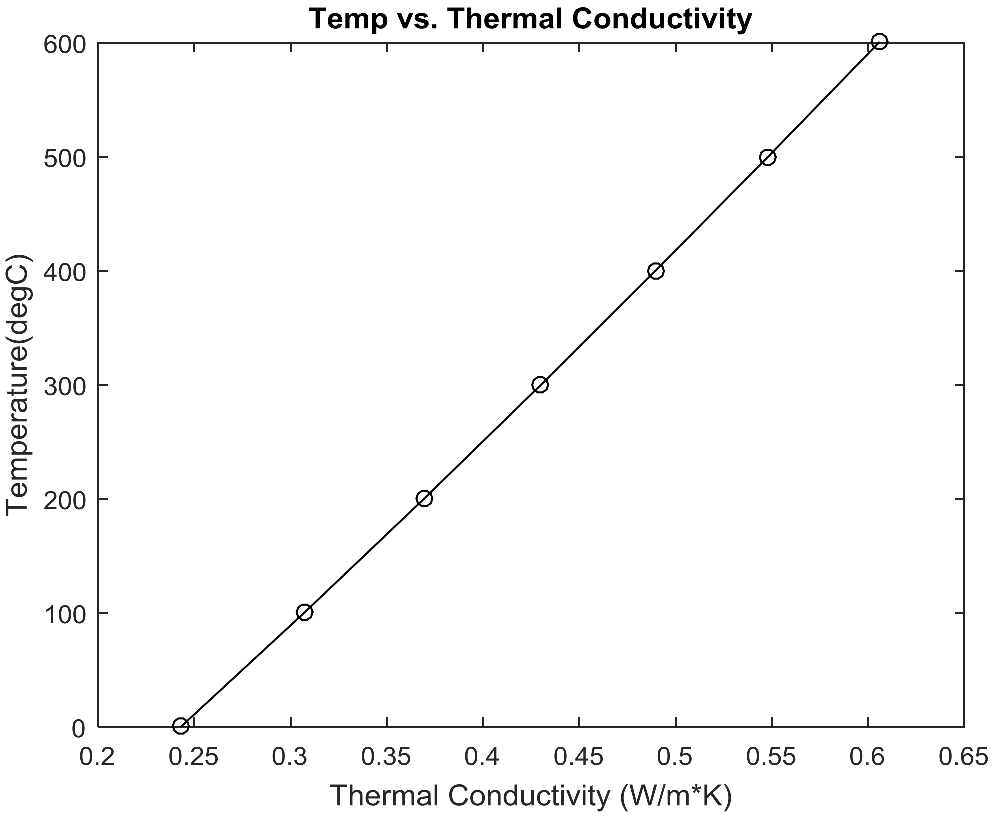

Figure 47-Thermal Conductivity of Silver Nano-Particles

This shows that the thermal conductivity of silver nano-particles approximated as a bulk material with air is reduced by two orders of magnitude. This model will be used to calculate the effective thermal conductivity of the silver nanoparticles.

4.1.2.2 Simulation Results

With the calculated effective thermal conductivity, a 3D simulation is performed to evaluate the sintering of the silver nanoparticles using the SRS process and the results are illustrated in Figure 48. Simulation results show that it takes a power input of 2.1 W for the microheater to reach 600

°C in 1 millisecond (in contrast to 1.1 W shown in Chapter 3). This change is due to the different treatment of the air. This was determined to be more accurate due to the accurate representation of the convection of air.

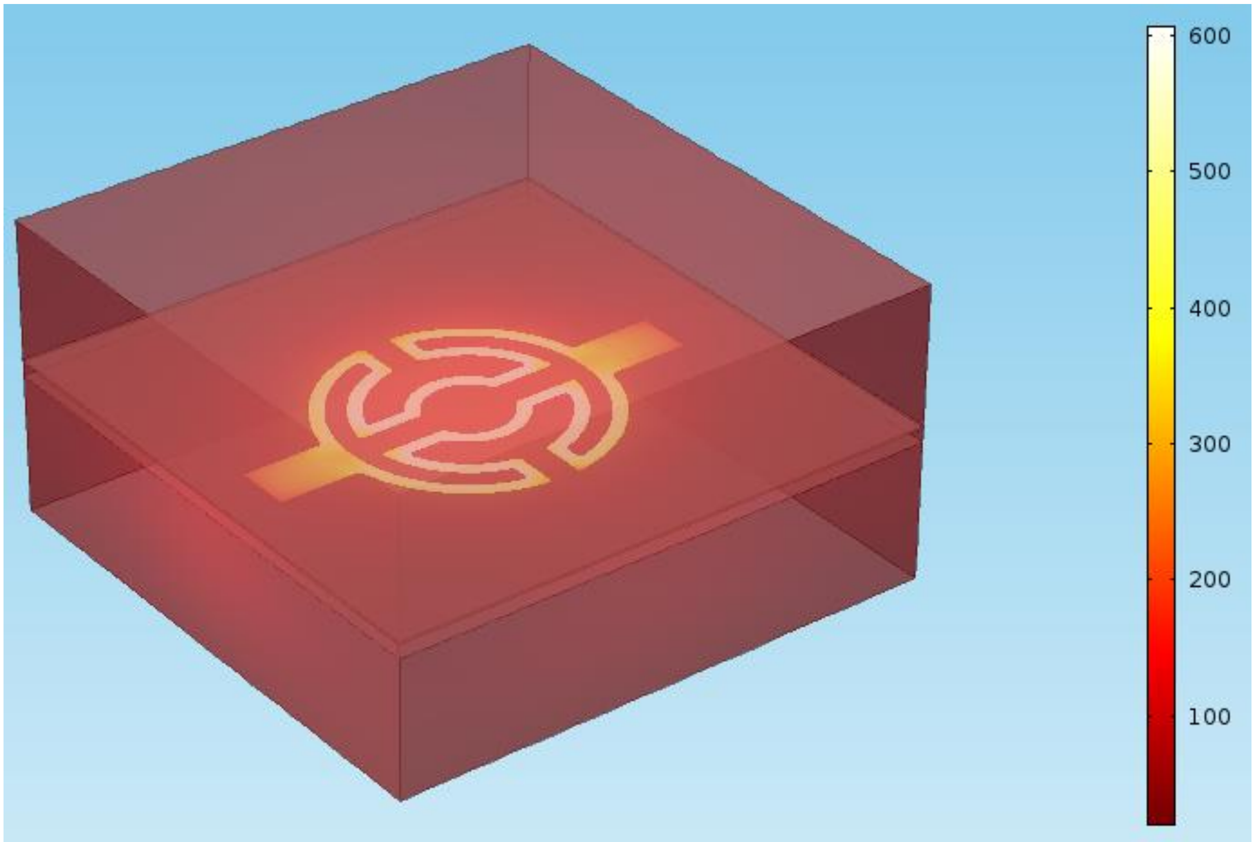

Figure 48-Temperature Rendering From Proof of Concept Simulation design from Figure 42

In this initial simulation, a 5 µm airgap was used to determine the temperature on the surface of the silver nanoparticles. Previous studies suggest that 1000^0C surface temperature is required for 1 *ms* operations. In this simulation, surface of the particles reached a temperature of 292^0C in 1 *ms*. From this evaluation, the heater temperature must maintain 600^0C for a prolonged period of time. This was accomplished by creating a temperature ramp, based on the time and temperature correlation, established in the initial model. This temperature ramp can be seen in Figure 48.

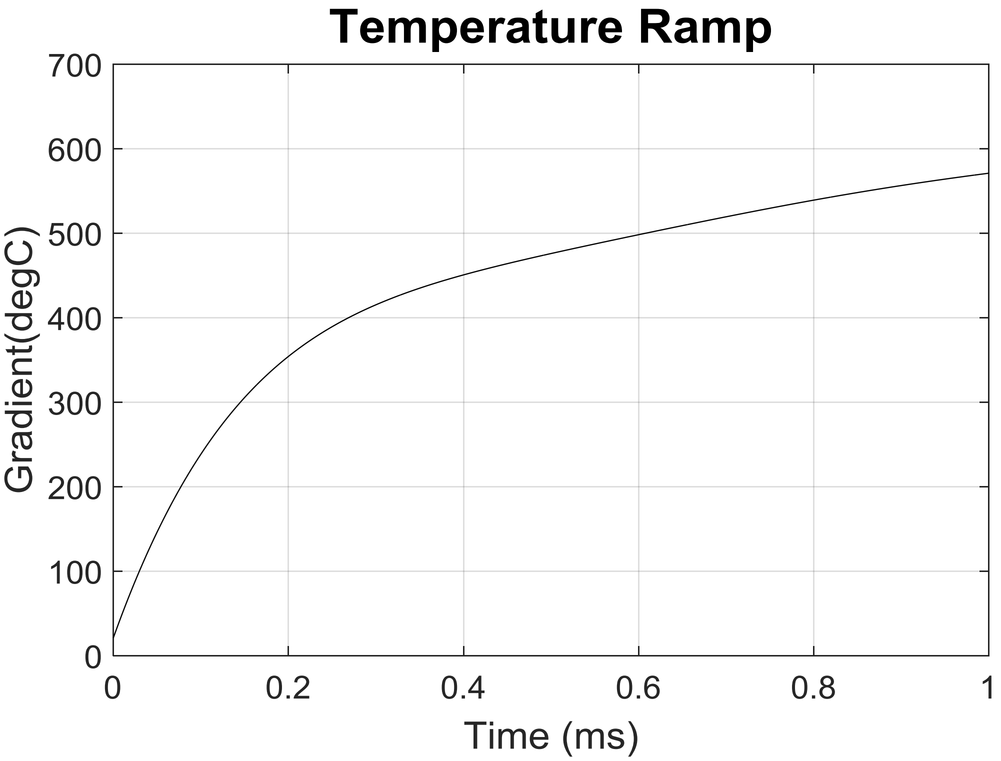

Figure 49-Temperature Ramp for a 2.1W Microheater

Since 1 *ms* was determined to be an insufficient amount of time to provide a high enough equilibrium temperature based on previous research, a new thermal response time was changed to 10 *ms*. The heater in the following results ramps up to 600^{0}C in 1 *ms* and then it is maintained for 9 *ms*. Using these exact parameters, the next goal is to see how the temperature on the surface of the nano-particles will be affected by varying the airgap from 1 µm - 30 µm. These results are provided in Figure *50*.

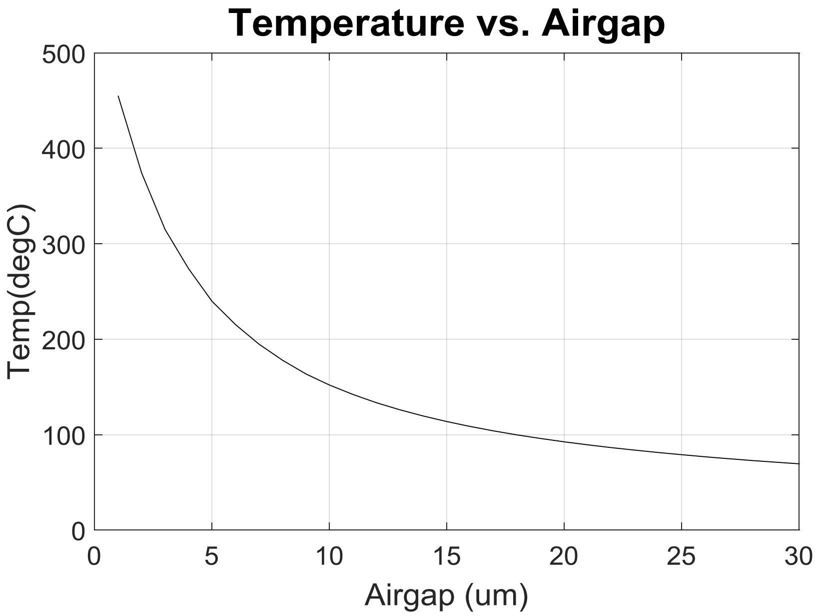

Figure 50-Temperature on the Surface of Particles with Varying Airgap

It can be seen that the temperature quickly drops off with increases in the airgap. This suggests that for a 10*ms* duration, the heat provided by a microheater quickly becomes negligible at distances of greater than 30 μm. Another parameter to observe was the printing resolution. This was evaluated by observing the temperature distribution on the surface of the nanoparticles. The temperature was sampled every 1 μm along the centerline of the microheater as illustrated in Figure *51* by the dotted line labeled x-axis, and extending 50 μm outside the heater. The temperature distribution on the surface of silver nanoparticles at 10 *ms* are shown in Figure 52.

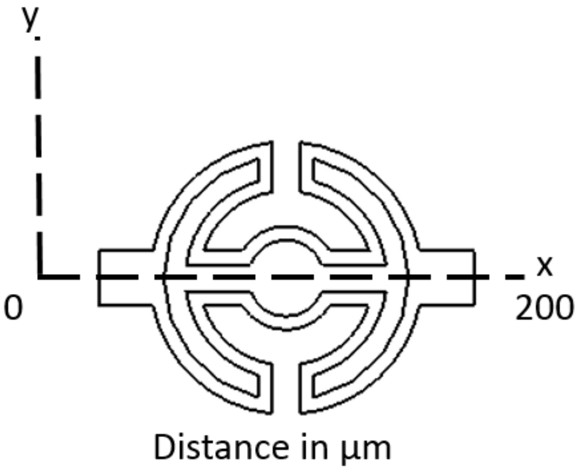

Figure 51-Line Sampled for Temperature Plot to Show Selectivity

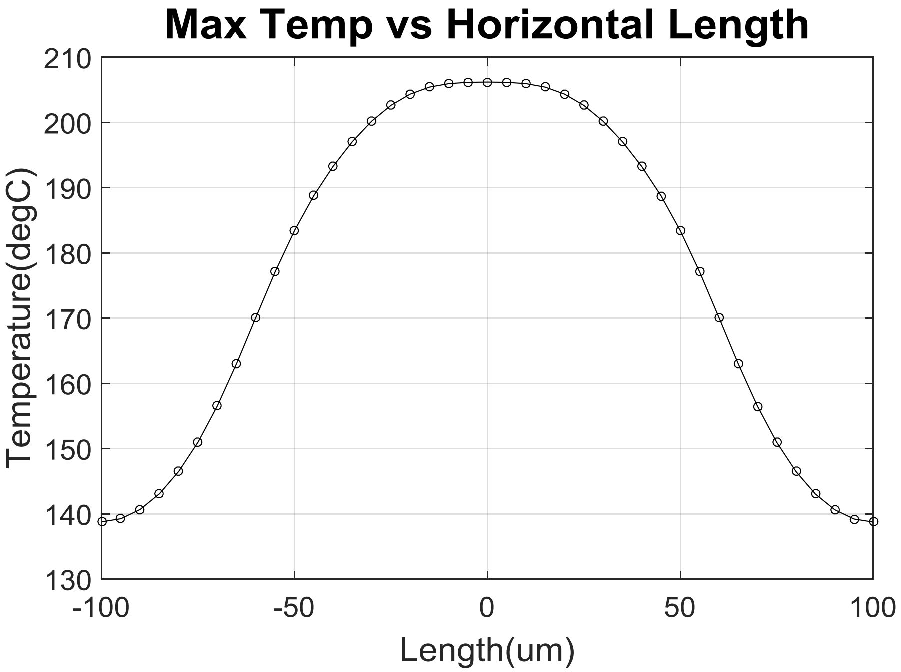

Figure 52-Temperature across the Microheater to Show Selectivity

From the simulations presented here, the SRS printing system is a viable method of providing selective sintering with close proximity operations. Based on previous work, it is likely that an extended heating time will be required to achieve good sintering quality However, this concept is new and requires experimental confirmation to determine whether sintering can actually be achieved. From surface temperature evaluation in numerical modeling, this method appears feasible.

4.1.3 Particle Simulation

SRS is also capable of printing different materials. To prove the versatility, we have also evaluated printing of polymer materials using SRS. In the evaluation, Nylon 12 was used and the particle size ranges from 25-92 µm in diameter. Its melting point is 184^{0}C. In a typical SLS 3D printer from 3D Systems, the surface temperature of the Nylon particles is raised to a temperature ~180^{0}C with a laser scanning speed of 4000 mm/s - 5000 mm/s [126], which suggests a sintering time scale of less than 1 millisecond. To achieve millisecond sintering of Nylon particles with SRS, we need to be able to raise the surface temperature to above ~180^{0}C on a millisecond timescale. To test the feasibility of this goal, a numerical model was developed to simulate the SRS process with an air gap of 5 µm. The results are shown in Figure 53, which show the temperature on a Nylon particle surface have gone well above 180 ^{0}C at 1.5 *ms* (Note this image is upside down as compared to all the previous images).

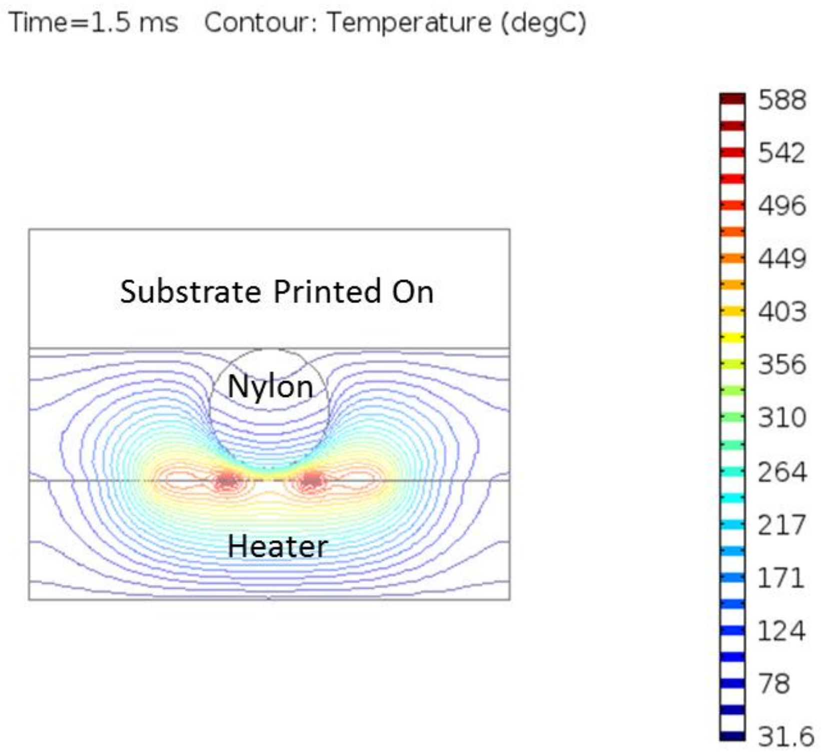

Figure 53-Thermal Contours of a Nylon 50 µm Particle Exposed to a Microheater for 1.5 ms

4.1.4 Improved Operation

The key to improving the SRS process is to keep the heat in the particles to be sintered, which means to maximize the heat flux into the particles and minimize the heat flux out of the particles. Heat flux is determined by thermal conductivity and temperature gradient as shown in (20.

$$q_s = -\frac{k\partial T}{\partial x} \tag{20}$$

In this equation q_s is the heat flux out of the surface of the particles. Therefore, to minimize the heat flux out of the particles, the objective is to reduce the thermal conductivity of the printing substrate (i.e., the substrate to be printed on) and to minimize the temperature gradient $\frac{\partial T}{\partial x}$ between the surface of the printing substrate and the particles to be sintered. On the other hand, to maximize the heat flux into the powder particles, the thermal conductivity of the medium (currently air) needs to be increased and the temperature gradient between the heater and the particles to be sintered needs to be maximized. Figure 54 shows the areas being evaluated to improve operations. Here the domain flux is the transfer of heat through the air into the particles being sintered, and the boundary flux is the flux out of the particles and into the substrate.

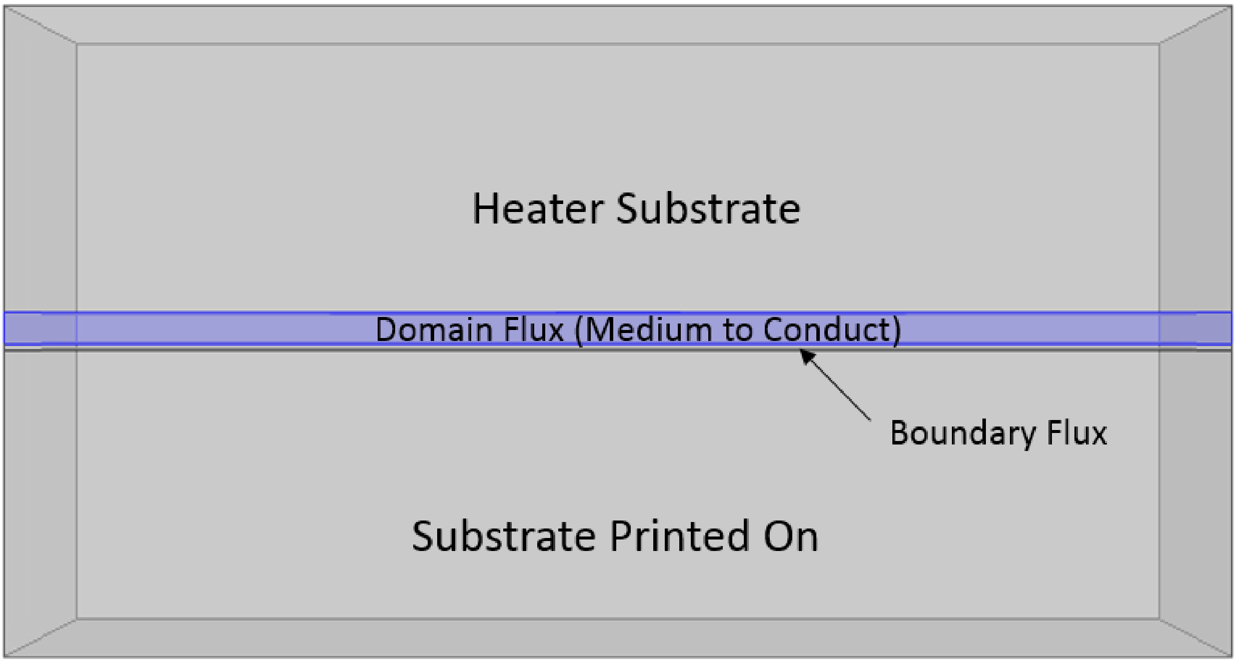

Figure 54-Operational Improvement Sections of Printing System

To numerically prove these concepts, four different cases were setup where materials with different thermal conductivities were used to evaluate the max temperature with consistent power consumption. The four scenarios each change the parameters that will enable a more optimal operation of the printer. These cases are as follows:

Case 1:

Substrate printed on is Silicon

Medium to conduct is air

Initial surrounding temperature is 20 °C

Case 2:

Substrate printed on is glass

Medium to conducti is air

Initial temperature is 20 °C

Case 3:

Substrate printed on is glass

Medium to conduct is Helium

Initial temperature is 20 °C

Case 4:

Substrate printed on is glass

Medium to conduct is helium

Initial temperature is 100 °C

Each case reveals that when these three parameters are changing, this can have a significant impact on the operations of the printer as shown in Table . Another observation was that the heat flux in and out of the particles being sintered was generally close to one another. The reason is because the majority of the heat being directly transferred in and out which is caused by the layer of particles being relatively thin, 1 μm in size.

Table 18-Characteristics of Heater Based on Different Cases

	Power (W)	Max Temperature (^{0}C)
Case 1	2.1	27
Case 2	2.1	239.65

Case 3	2.1	411.86
Case 4	2.1	442.58

It is demonstrated that the SRS process can be improved with a larger thermal conductivity of the medium gas, a smaller thermal conductivity of the printing substrate, and a smaller air gap. The larger the gap, the more air could absorb the heat and energy and the smaller the temperature gradient. This gap allows waste, as the heat and energy are being dispensed into the air instead of into the nano-particles to be sintered.

4.1.5 Comparison to SLS

In comparison to SLS, SRS outperforms SLS in multiple facets. The SRS printer was compared to a commercially-available low-cost Prodways SLS printer. It was found that the SRS consumes 14x less power, has a greater operation temperature, and over 4x greater resolution [127].

Table 19-Table Comparing Characteristics of Two Types of Printers [127]

Brand	Model	Type	Power	Max Temp	Scan Size
ProdWays	P1000	SLS	30 W	200C	450 um
-	-	SRS (New Method)	2.1 W	450C	100 um

In addition, the SRS printer is a scalable printer. The process can theoretically use a large number of microheaters in an array much bigger than the 2x2 heater array used in this thesis. This can significantly increase speeds and digitalize the printing process.

4.2 Overall System Design

To complete the overall printing system, the printer requires external circuitry to power and control the heater and a high-precision linear motion system to control the air gap. The circuitry used an Arduino Mega 2560 microcontroller to control power to the heater and to record the feedback in the system. The design of the linear motion system provides 500 nm resolution with a unique contact sensing method designed for this system to create a reference point. This system was tested in two different setups, but was not successful.

4.2.1 Circuitry and Control

The external circuitry requires an external power supply to power the microheater and an additional sensing device. Power is provided by a Dr. Meter Hy3005M-S variable DC power supply, use of an Arduino Mega 2560 microcontroller to provide the control systems, and a 12V computer power supply. The circuitry is the same setup as was used in 3.4.2.3 of the microheater testing with additional logic provided in Arduino to prevent the heater from burning out.

4.2.2 High Precision Linear Motion System

The high precision linear motion system was necessary as determined by the operational parameters. As was shown in Figure 50, little heat will be transferred from the heater to the particles if the operation is not within close proximity. These results show that the motion control system will need to be able to maintain a ~1 μm gap to achieve the desired heat transfer. To accomplish this goal, a device was designed that utilized a high precision Thorlabs motor with 50 nm resolution and 800 nm repeatability, an OptoSigma micrometer (WGP-13R) with 500 nm resolution, and a contact sensor.

The full assembly of the motion system and its main components are shown in Figure 55. Here the system shows the two different components: the main assembly and a ThorLabs motor. The main assembly consists of a manual micrometer, a linear rail system, return springs, and a holder for the printhead (i.e., the packaging of the microheater array), which is used to adjust the Z-position of the printhead.

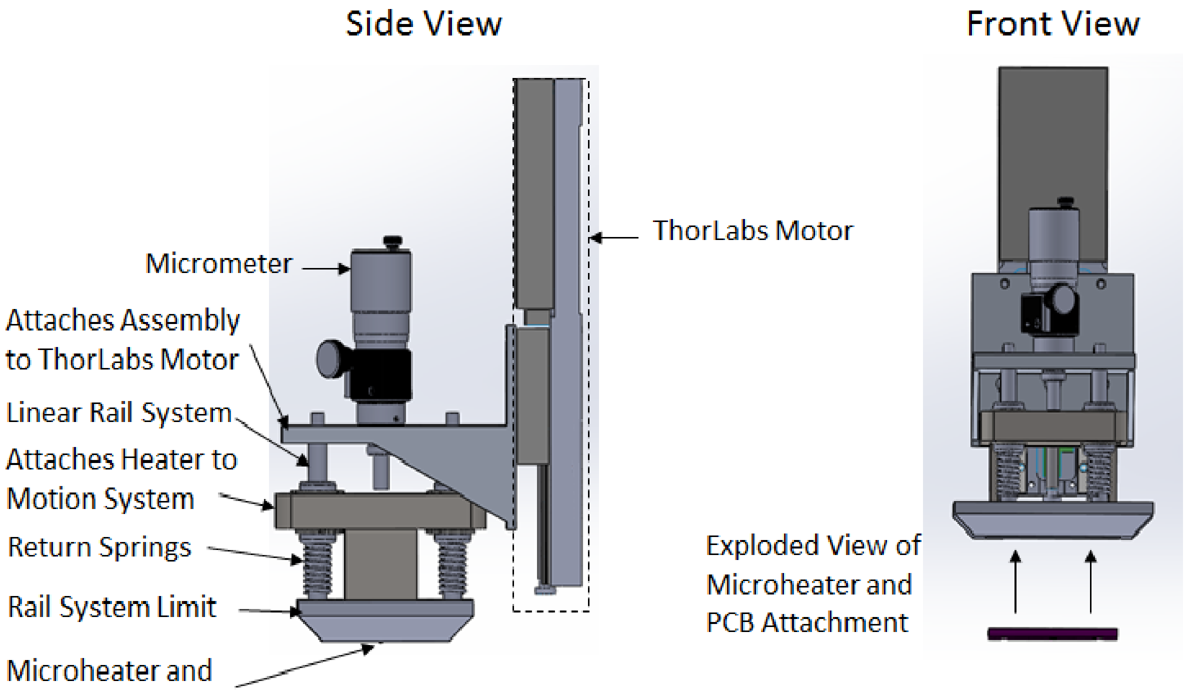

Figure 55-Motion System Design of Actuators and Structural Assembly

This device works by using the Thorlabs as part of a roughing motor to move the entire assembly vertically. Once the assembly is in a position close to the contact sensor, the micrometer can then be used to further adjust the Z-position of the printhead.

A compact affordable sensing mechanism with a millimeter range of motion was required for the high-precision motion in Z axis, which put many constraints on the choice of sensors for the SRS printing system. Because the objective of this thesis is to obtain a proof of concept rather than to develop a fully functional SRS printing system, a simple method was developed to help locate the printhead in very close proximity of the substrate. First, we integrate a contact sensor on the printing substrate to detect the contact between the microheater and the printing substrate. In reference to this contact position, the micrometer is then used adjust the Z-position of the microheater at a resolution of 500 nm. The contact sensor is part of a circuit that is completed upon contact with the microheater as shown in Figure 56. The sensor was fabricated by evaporating a layer of 100 Angstrom of Ti and 1000 Angstrom Au layer onto the printing substrate. Once the contact sensor are manually aligned under a microscope and brought into contact with the conductive leads of the microheaters, the circuit is complete and the continuity can be measured. A schematic of this operation is shown below in Figure 56.

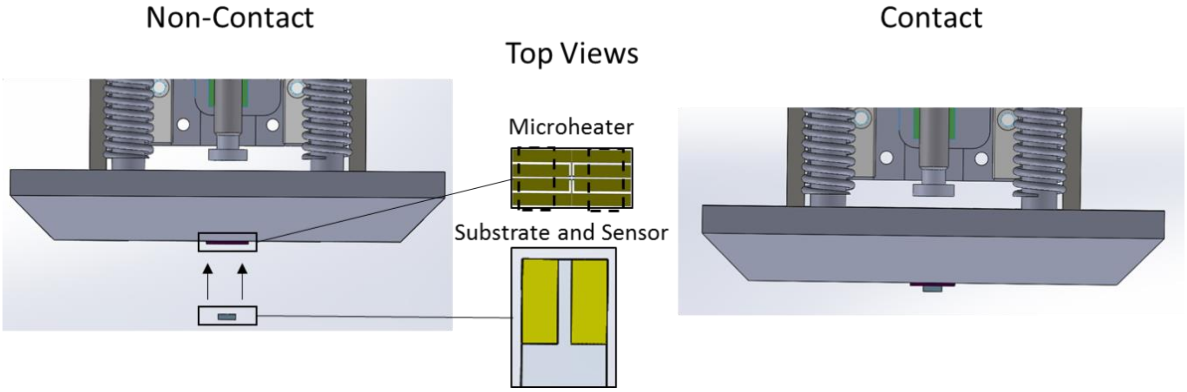

Figure 56-Contact Sensor Operation

Fabrication of this high precision system did not require high tolerances. The method of using the linear sliders and a surface mount heater in the system alleviated much of the margin of errors. This made fabrication of 3D printing of the parts possible. The idea behind this system was to mount the device to a smooth surface which would not deviate more than a few nanometers, and the linear sliders would then ensure that the platform that the heater traveled on was always level. A tolerance analysis was performed to evaluate the tolerances for the critical parts of the system. The final tolerance would be associated with the assembly. The attachment to the linear sliders in combination with the screw attached PCB and heaters had a maximum tolerance of .4239mm of variance. This will ensure that the heater will not be allowed to deviate more than 1 um from the surface due to a tilt in the overall assembly. An example of the tolerance demanded with assembly is in Figure 57 and Figure 58 with the tolerance labeled as Tol. is found below.

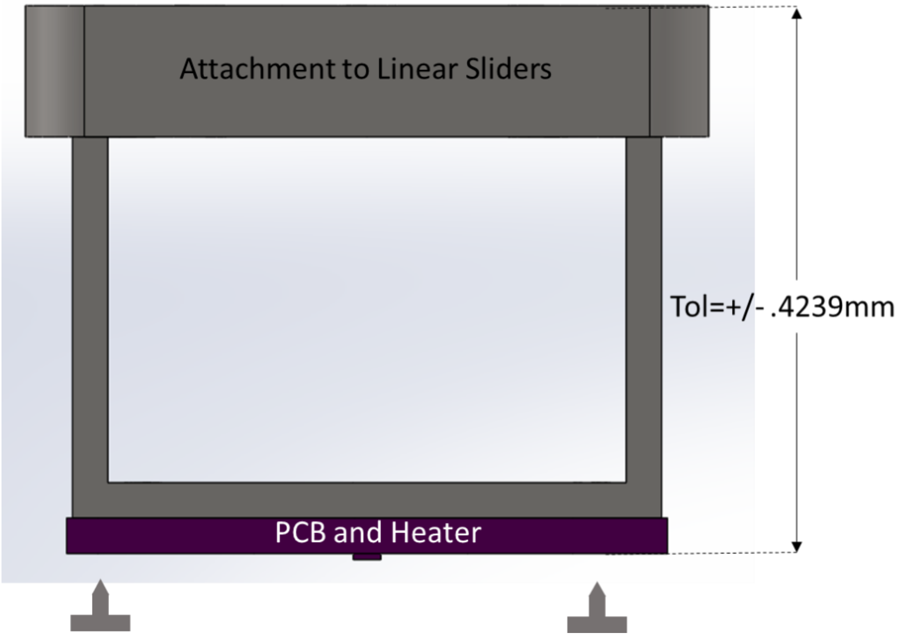

Figure 57-Tolerance for Final Assembly of Critical Parts

This tolerance was formulated by making sure the microheater could not deviate more than 1 µm from one edge of the microheater die to the other side. This can be seen in Figure 58 . From this assumption, an angle can be found and extrapolated out to the entire structure to determine the maximum angle or the maximum tolerance as shown in Figure 57.

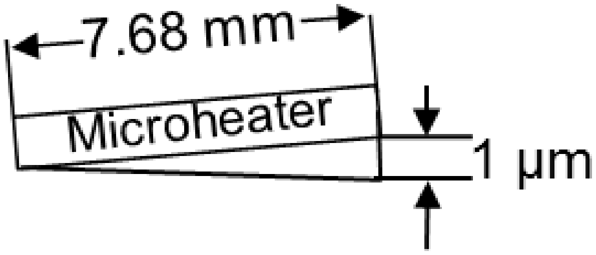

Figure 58-Tolerancing Determination from Heater Die Size and 1 µm Tolerance

Fabrication is an essential component to ensuring the proper operation of the SRS prototype. From the evaluation of the tolerance, the critical component this affected was the linear rail system. For this part, a tolerance was determined to ensure the micrometer could not be more than 1 µm higher on one side of the die from the other. A majority of the parts were ordered from commercially available vendors. Others were fabricated through 3D printing, machining, and manual assembly. Below is a list of the parts and how they were obtained or fabricated based on the parts listed in Figure 55.

Thorlabs Motor

Commercially available from Thorlabs.

Specifications

Resolution: 50 nm
Repeatability: 800 nm

Micrometer

WGP-13 R commercially available form OptoSigma

Specifications

Resolution: 500 nm

Assembly Attachment to Thorlabs/Heater to Assembly/Rail Limit

3D printed
Tolerance: +/- 100 um

Linear Rail System

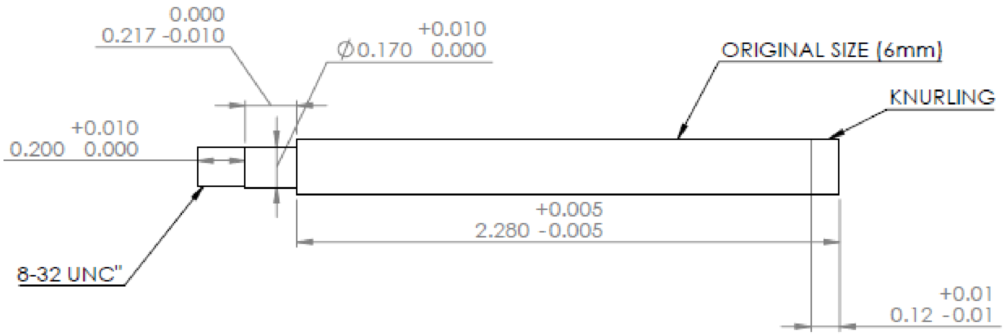

Sensor Substrate

E-beam Evaporated Ti: 100 Angstroms thick and Au: 1000 Angstroms thick on top of Ti. Ti acts as the adhesive layer for bonding to a glass substrate.

Miscellaneous Parts

Parts such as rail guides, nuts, screws, etc. were all ordered from commercial vendors and have not been included due to the extent of the list of each individual part. The PCB and Microheater are part of another study not included as part of the precision motion system.

Assembly is the final step in fabrication. The rail system consisted of the most parts. In the rail system, the top side of the rails required a tight slip fit into holes connecting the rails to the Thorlabs connector and half an inch 6-32 screws where used to hold the rails in place. A press fit was used to hold the bottom side of the rails into the rail system limit. The linear bearings had to be press fit into the 3D printed structure connecting the heater to the rail system. Snap rings were then put in place to ensure the bearings did not slip. Due to limited funds and time, the final assembly did not consist of the Thorlabs motor. Instead, an additional setup stand was created to enable testing of the sensing system and motion using the micrometer. This system used the same connection features as were provided on the Thorlabs motor and a solid bottom surface that could be used to control the distance between the overall structure and the print area. This device was 3D printed. The final assembly is shown in Figure 59. In the final device shown in Figure 59, wires can be seen which provide connections to the microheaters. These wires were manually connected. This connection is vital to the operation of the high precision contact sensing device. The sensor was fabricated by electron beam evaporation using Kapton tape as a mask to create the pattern shown in Figure 59. This sensor which also serves as the substrate is then manually placed in the overall system. The sensor is shown in the right side of Figure 59 and the overall system of how it will be used is on the left in Figure 59.

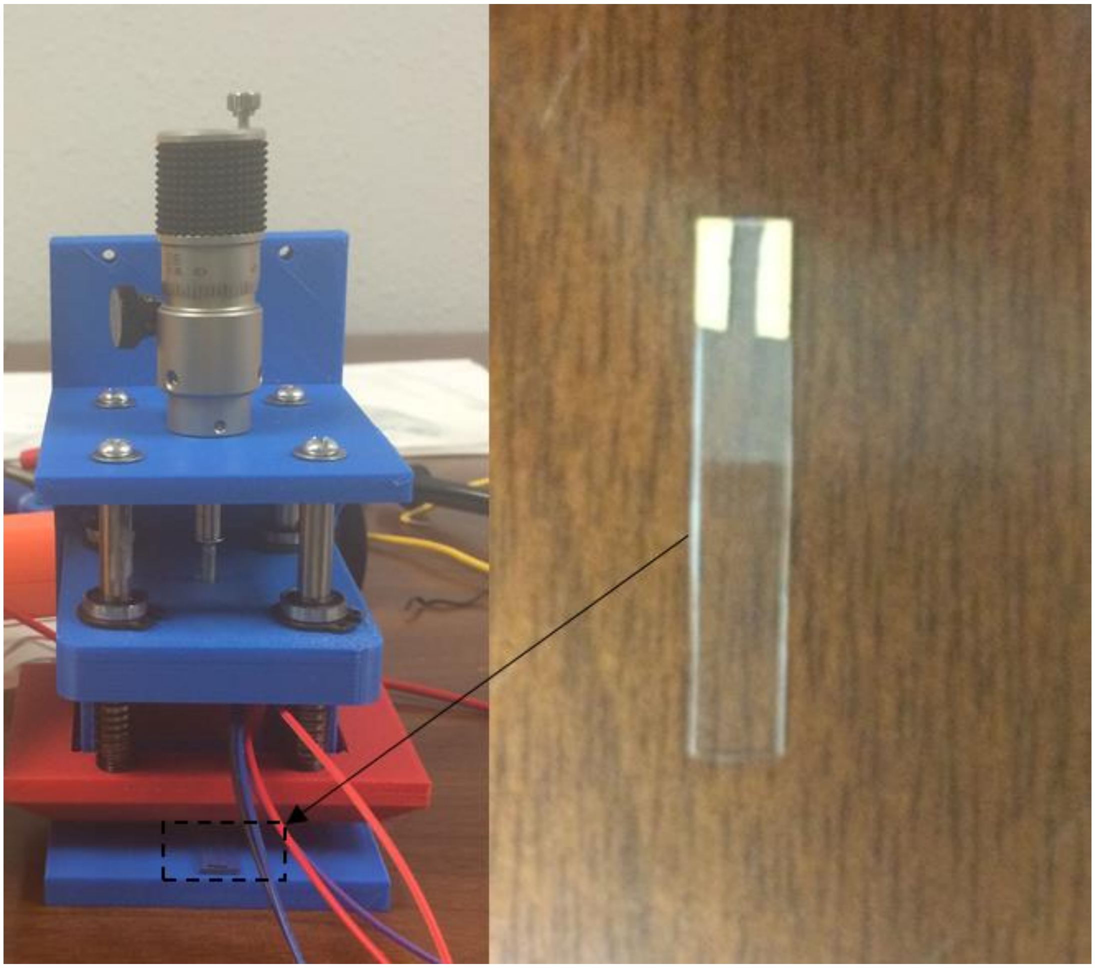

Figure 59-Sensor and Sensor System Setup

With a final product fabricated the device can now be tested. Testing was limited to a system with only a micrometer and an attachment to a stationary fixation system as was previously mentioned. The system was tested by manually placing the sensor and its metal conductive strips beneath the microheaters. The heaters were then lowered until the heaters made contact with the sensor. When the sensor was in contact with the heaters continuity could be measured. The position of the sensors will be as shown in the digital image in Figure 60.

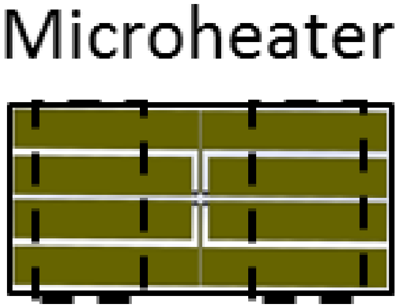

Figure 60-Showing the Placement of the Sensors Relative to the Heaters When in Contact

In Figure 60, the conductive metal strips will be laying across two separate heaters on both sides of the microheater array as shown by the dashed lines. This enables continuity to be measured between each of the heaters. A test setup is shown in Figure 61. In Figure 61 you can also see the resistance being measured from making this connection.

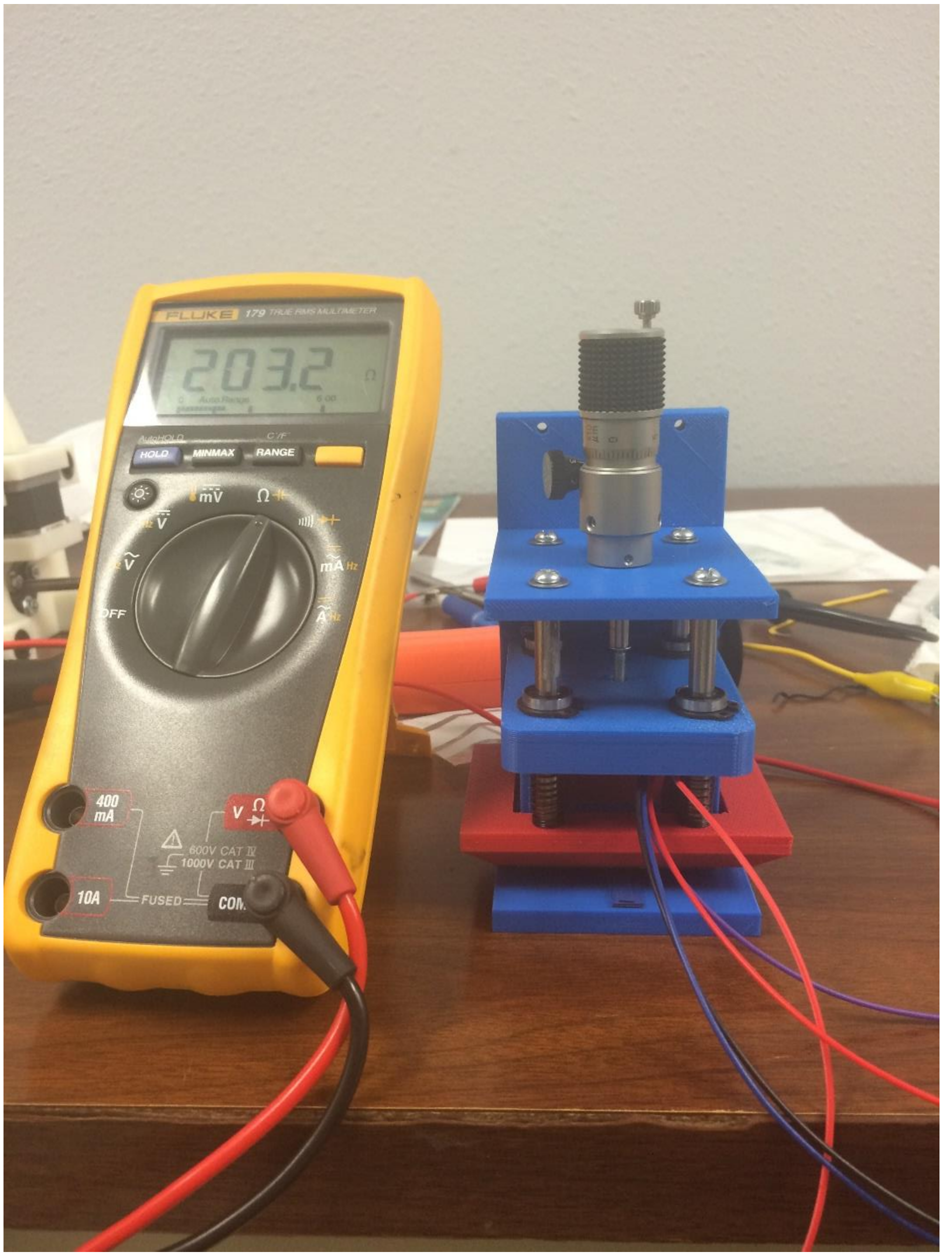

Figure 61-Testing of Continuity between Heaters Due to Sensor Contact

The resistance measurement proves that a conductive path between heaters can be measured between heaters. This test is also confirms that the system is functional and a viable solution for detecting the contact between the microheater and the printing substrate. By using this contact sensor, a reference position of the microheater to the substrate is known. The micrometer can then be used to adjust the heater to the position desired relative to the previously found reference.

4.3 Testing of SRS Concept

With the developed printhead and the precision motion system for air gap control, the concept of SRS is put to test experimentally in this section. To avoid the complications of sintering real powder particles, which would require additional powder spreading system, two alternative materials (thermal paper and a photoresist) were tested in an attempt to demonstrate experimentally that the SRS concept can be used to pattern heat.

4.3.1 Testing with Thermal Paper

The first test was on a piece of 10 µm thick thermal paper, which was placed on the substrate as shown in Figure 62. The objective is to test whether it is possible to transfer a pattern onto the thermal paper from the microheater array without contact. When heat is applied at temperatures greater than 60°C, the heat should transfer ink onto the substrate below the tape. This would provide a preliminary proof of concept for the SRS process. The experimental setup is shown in Figure 63.

Figure 62-Testing Setup of Thermal Tape to be Heated on the Sensing Substrate

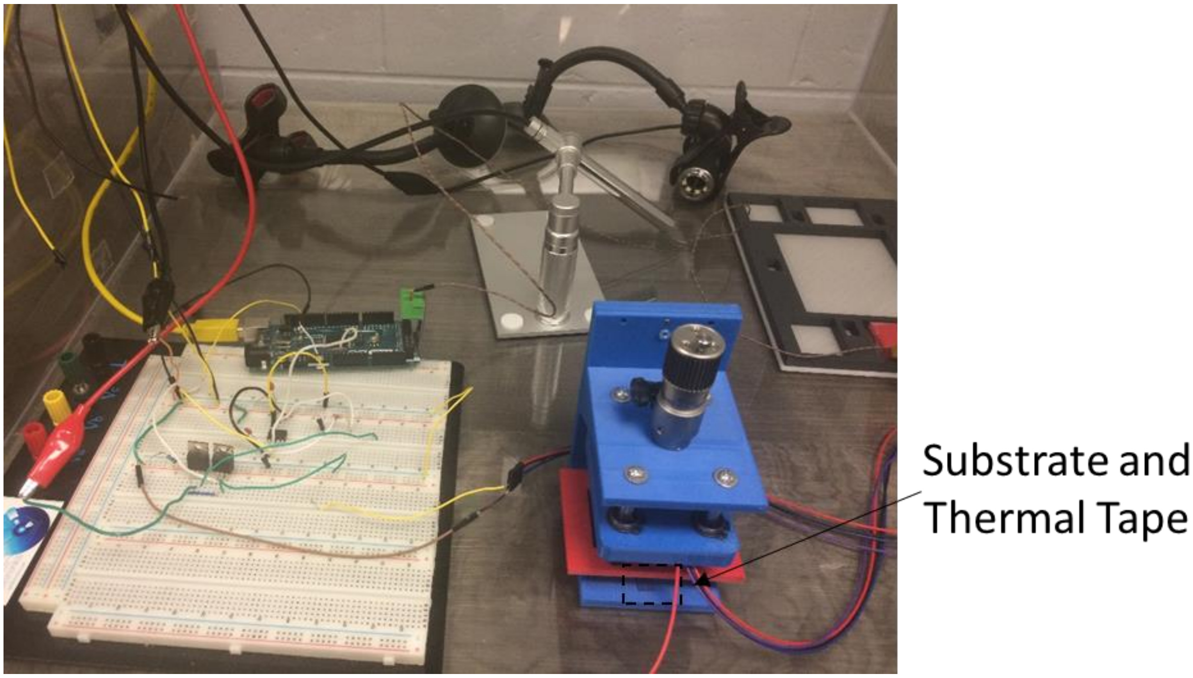

Figure 63-Full SRS Setup for Test of SRS Concept using a Thermal Paper

The testing results were inconclusive. The temperature ramped up to 600^0C as was shown by the resistance feedback system. Once this temperature measurement was made, the heater was programmed to turn off. The thermal tape was inspected after the test with no conclusive results to show any pattern transfer. This is likely due to the possibility of not being able to accurately position the heater with a micrometer and contact sensor or due to inadequate heat transfer from the heater to the thermal tape.

4.3.2 Testing with Photoresist

In a second test, the sintering process was tested by using a thin layer of AZ series 4110 photoresist. This material was chosen due to its low thermal conductivity being similar to that of the silver nanoparticles used in the modeling, and ease in manufacturing a 1 µm thick layer. The idea of using photoresist is that when exposed to the heat of the microheater, a blemish would be left in the photoresist.

To create this setup the 4110 photoresist was spun onto the substrate with the contact sensors. The photoresist was spun at 6000 rpms for 45 seconds, which was a recipe proven to have been successfully create a 1 µm thickness of photoresist. Once the layer of photoresist was spun on, the heater was placed by using the contact sensor as a zero reference after contact was made. It was then slightly raised to 5um height above the substrate and manually moved to where the photoresist would be directly below the heater. The heater was tested multiple times by applying 5V to the heater for ~10 seconds, in which the heater was recorded to reach temperatures greater than 600°C by the internal circuitry feedback. The photoresist was then evaluated underneath a microscope. There was no visual evidence of any heat having reached the photoresist. It is possible that the system is not being accurately positioned, and this is likely the reason for inconclusive results. This may also be due to distortion from the heat that is not visible. There are no results as to the appearance change that would occur when heating photoresist.

Chapter 5 HEATER DESIGN IMPROVEMENTS BASED ON SRS PRINTING PARAMETERS

5.1 Introduction

From literature, it is known that the previously evaluated design of a Ti heater on a glass substrate is not optimal for our purposes, which was kept due to its ease of fabrication to provide a proof of concept. In this chapter, a new design of the microheater is presented, which is demonstrated to perform better base on numerical simulations.

5.2 New Design

There are a few issues with the current design of the Ti microheater. First, the heat generated by the microheater can dissipate through the backside of the heater, which leads to a waste of energy and high power consumption. Second, titanium can oxide at high temperature, which may fail the microheater. One popular method of insulating the backside of the microheater is to use a suspended membrane, that is, to etch the backside of the microheater and use air as an insulator as illustrated in Figure 9 or Figure 11, because air has a lower thermal conductivity (.0257 W/m*K) than most of the substrate materials. To prevent the microheater from oxidation at high temperature, platinum is chosen as the resistive material to replace titanium. In addition, a protective layer will also be used to protect the microheater from oxidation.

There are a number of considerations for choosing the material for the suspended membrane. First, it needs to have a moderate thermal conductivity, which should not be too high to increase power consumption and should not be too low to cause non-uniformity of temperature in the microheater region. In addition, it needs to be able to stand the stress from the operation of the microheater. Silicon nitride has been a popular choice for the suspended membrane for these considerations [48].

Based on previous studies from literature, a design of an 800 µm x 800 µm suspended membrane with materials and geometric dimensions are illustrated in Figure 64 and Figure 65. In this design, a PECVD silicon nitride layer is used on the front side to conduct heat outward to the printing substrate and protect platinum from oxidation and a LPCVD silicon nitride layer is used on the backside for insulation. This is not ideal because the thermal conductivity of LPCVD silicon nitride (~8W/m*K) [48] is higher than that of the PECVD silicon nitride (~4.5 W/m*K) [128]. The reason for this choice is because the front side silicon nitride has to be deposited after the platinum, titanium, and gold layers, which requires a low process temperature to avoid agglomeration and failure of the metals. PECVD has a lower process temperature than LPCVD, making it compatible with the fabrication process.

In addition, suspended membranes of this nature are susceptible to early failure due to stresses. Stresses are observed in the form of residual stresses from fabrication methods as well as from thermal stresses. Experimental studies [49] have previously performed optimization of suspended membranes for microheaters. In literature, stresses from thermal expansion were accounted for and residual stresses were offset to obtain longer life out of the membrane. For a square membrane with a side length of 800 µm, a maximum deflection of 20 µm was observed before rupturing. In our design, LPCVD silicon nitride with the low tensile stress of ~177MPa and a thickness of 3000 angstroms was used as a base layer of the suspended membrane. Then a platinum microheater was patterned on the LPCVD silicon nitride layer, and followed by an enclosing layer of PECVD silicon nitride with a thickness of 3500 angstrom and a compressive stresses of -1GPa.

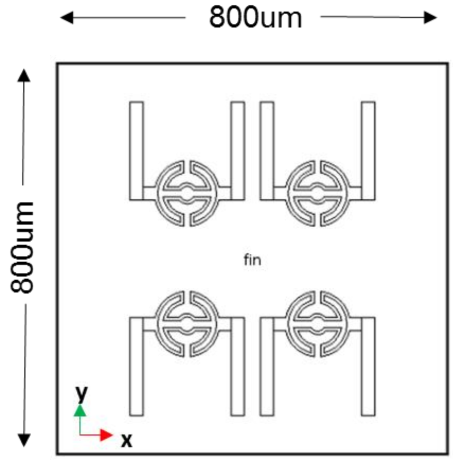

Figure 64-Suspended Silicon Nitride Membrane

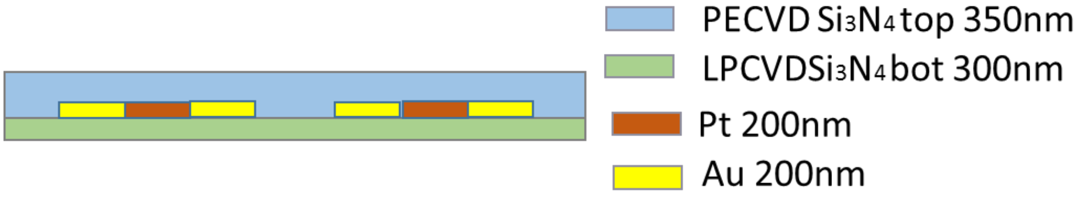

Figure 65-Cross Sectional View of the Suspended Membrane Microheater

5.3 Numerical Modeling

To evaluate the performance of the new microheater design, the previous numerical model was used to simulate the SRS process with a few minor changes. The configuration of the numerical model is shown in Figure 66.

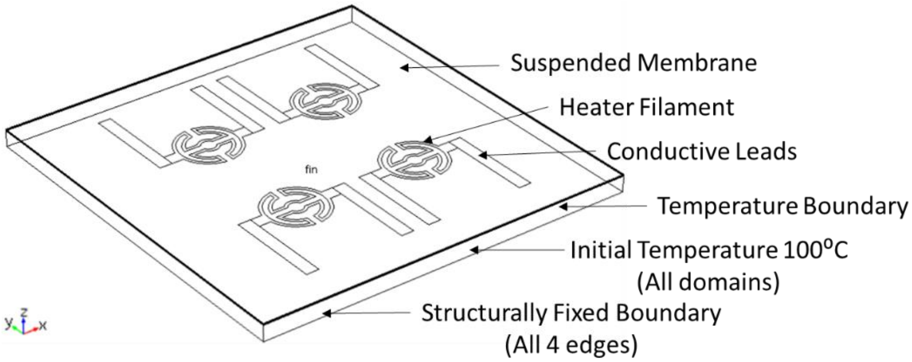

Figure 66-Initial and Boundary Conditions

First, the open boundary condition was replaced with a temperature boundary, which resembles a common practice in some of the SLS printers to maintain a constant powder bed temperature to avoid the side effects from rapid cooling of materials. Structural mechanics were accounted for in this modeling by fixing all four edges to simulate the fixed edges of a suspended silicon membrane. Each layer was also fixed to its adjacent layer as a rigid connection.

This model includes the glass printing substrate, the silver nanoparticles, the microheater array, the suspended membrane, air on both front side and backside of the membrane, and the silicon substrate used to support the suspended membrane. Figure 67 displays a zoomed in view of the configuration. The silicon substrate used as the base for the heater was later considered negligible. The final geometries used for modeling are in Figure 21, Figure 65, and Figure 69. A list of the materials used for the modeling and their corresponding properties are given in Table .

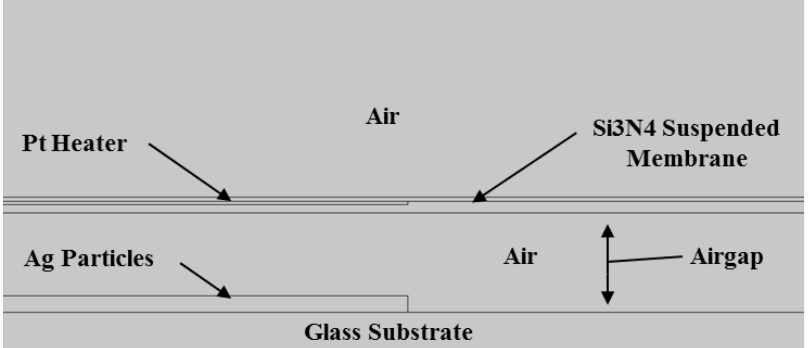

Figure 67-Zoomed in View of Modeling Configuration

Table 20-Material Properties used for Heater Design

Materials for Heater Design

	Titanium (Ti)	**Silicon**	**Gold(Au)**	**Si3N4**	**Pyrex-7740**
Electrical Resistivity (ohm*m) @ 20°C	1.54E-06	-	2.77E-08	-	-
Temperature Coefficient of Resistance (1/°C)	3.50E-03	-	0.0034	-	-
Thermal Expansion Coefficient (1/K)	8.60E-06	3.25E-06	1.42E-05	2.30E-06	5.50E-07
Thermal Conductivity (W/m*K)	21.9	130	3.17E+02	8	1.18
Specific Heat (J/kg*K)	522	700	129	700	753.12
Density (kg/m^3)	4507	2329	19300	3100	2230
Young's Modulus (Pa)	1.16E+11	1.70E+11	7.00E+10	2.50E+11	7.31E+10
Poisson's ratio (1)	0.321	0.28	0.44	0.23	0.17
Thickness (µm)	0.2	500	0.2	.3 &.35	inf
Purpose	Adhesive	Substrate	Conductor	Membrane	Printing Substrate

5.4 Evaluation of the New Design

This section is to evaluate some of the critical aspects to improve the operation of the microheater for the SRS printing system. The membrane size, electro thermal response, heat transfer through air, heat uniformity, and structural integrity are discussed.

5.4.1 Membrane Size

Membrane size has been shown to be a critical aspect of design for power consumption [129, 130]. The substrate used as a base for the microheater in this design is silicon which has a thermal conductivity of 130 W/m*K. This is a relatively high thermal conductivity when compared to other materials in the design. To ensure heat transfers onto the substrate being printed on, the suspended silicon nitride membrane needs to be designed large enough that heat from the microheater does not reach the silicon substrate. To make sure no heat was lost through the substrate an axisymmetric model was used to survey the effects of heat transfer on the size of the membrane. Only heat transfer was accounted for in this model. A temperature boundary condition of 600ºC was used to simulate the heater instead of incorporating all electrical characterization and Joule heating phenomenon. This was assumed an accurate assumption. An initial design of a membrane 800 µm by 800 µm was used initially and iteratively reduced in size. Using this simulation, the membrane was iteratively reduced from the square 800 µm membrane to a square 600 µm membrane. Figure 68 shows a square 600 µm membrane with a heater at the center and heat is back to its initial operational temperature of 100 °C before reaching the silicon substrate. This new design and its dimensions are also shown in Figure 69.

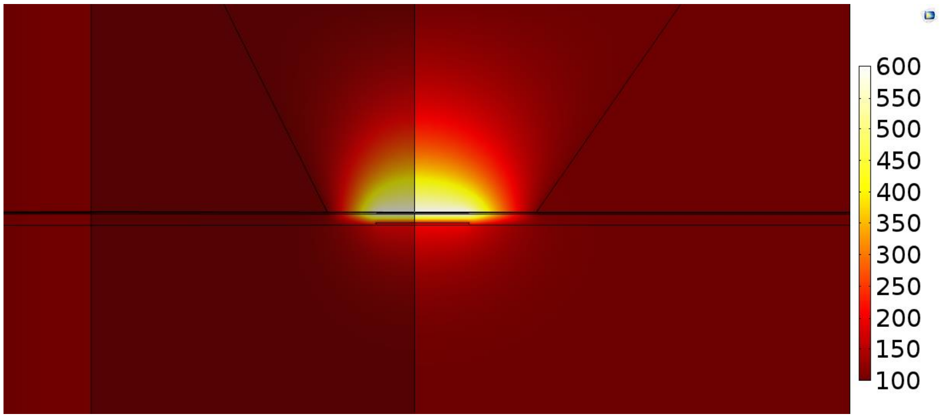

Figure 68-Axisymmetrical Modeling Results of Heat Distribution on Membrane Size

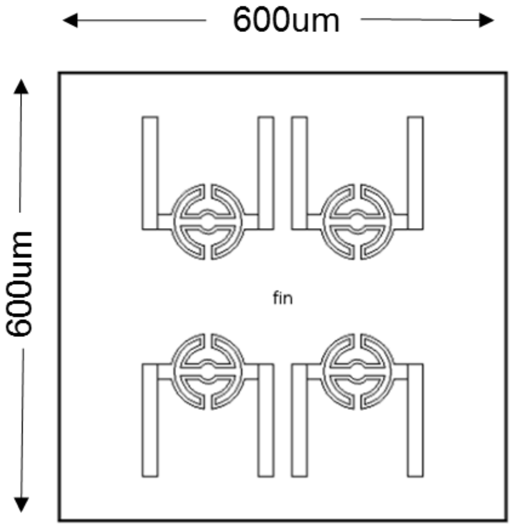

Figure 69-New Dimensions of Suspended Membrane

5.4.2 Electro-thermal Design

Analytical solutions, presented in Table 5, provided an initial guess for the amount of power required to heat the microheater to 600 ºC. An important factor in this calculation was the initial process temperature of the printing process. (6 displays that the temperature difference has a significant impact on the amount of power input into the microheater. By increasing the printing process temperature to 100 ºC less power is required to heat the microheater. This change in process temperature was accounted for in modeling by assuming an initial condition of 100 °C in the simulation. The goal of reaching 600ºC in 2*ms* was accomplished by an iterative search for the amount of power supply would be required to accomplish this goal. From numerical simulations, it was found that using a 2W power terminal could provide the heating in ~1.5 *ms*. Using (6 again, it was found that a .259 voltage supply would be required to accomplish this goal. The results of the temperature, thermal response time, and the voltage applied are listed below.

Table 21-Electro-thermal response Results Based on Numerical and Analytical Modeling

Temperature	**Time**	**Voltage**
600 ºC	1.5 *ms*	.259 V

5.4.3 Heat Transfer through a Medium

Modeling was used to prove that a microheater could provide heat to a substrate through a medium that would selectively sinter the desired areas. The design was specifically focused towards this goal. Evaluation of (5) and (12) reveal the parameters governing the magnitude of the heat flux in and out of a material. Thermal conductivity and distance between the heat source and the target, and are two variables that can be changed in favor of design needs. The area was determined by the size of the print and the temperature difference was also a design parameter. From those same equations, we can also observe that a low heat flux is needed on the surface of the printing substrate. This enables heat to be concentrated on the area being sintered. The Pyrex glass chosen achieves this objective.

Using the dimensions from Figure 64 and Figure 65, simulations were performed to see the impact of heat transfer on the distance between the heater and the substrate. To monitor the temperature versus the distance between the heater and substrate, a point was monitored at the center of the array on the bottom side of the silver nano-particles. This was the coolest point in the simulation, which corresponds to the last point to be sintered in a real time print scenario. A plot of temperature of the silver nanoparticles versus airgap is shown from a 1.5 ms transient evaluation in Figure 70. It can be seen that the NovaCentrix silver nano-particles can be sintered using this microheater and up to a 23 µm gap.

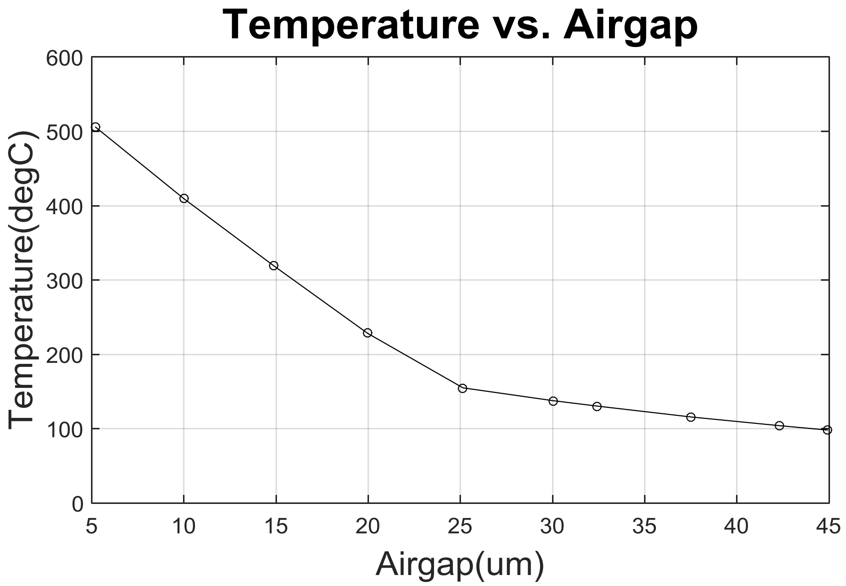

Figure 70-Temperature on Printing Substrate vs. Airgap

Another parameter in printing is the feasibility of being able to selectively sinter the desired areas of material. To observe the uniformity of heat, the temperature was measured for a single transient solution evaluated at 1.5 *ms.* The temperature distribution of the nano-particles on the printing substrate along the line shown in Figure 71 is plotted in Figure 72. It can be observed that there is a steep decline in temperature outside the area of the heaters, which is a good indicator that the sintering process can be performed selectively so that only the desired areas are sintered.

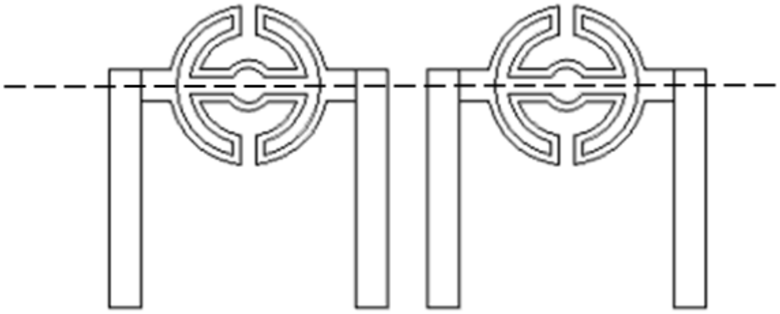

Figure 71-Line of Sample Points to Determine Selectivity of Printing

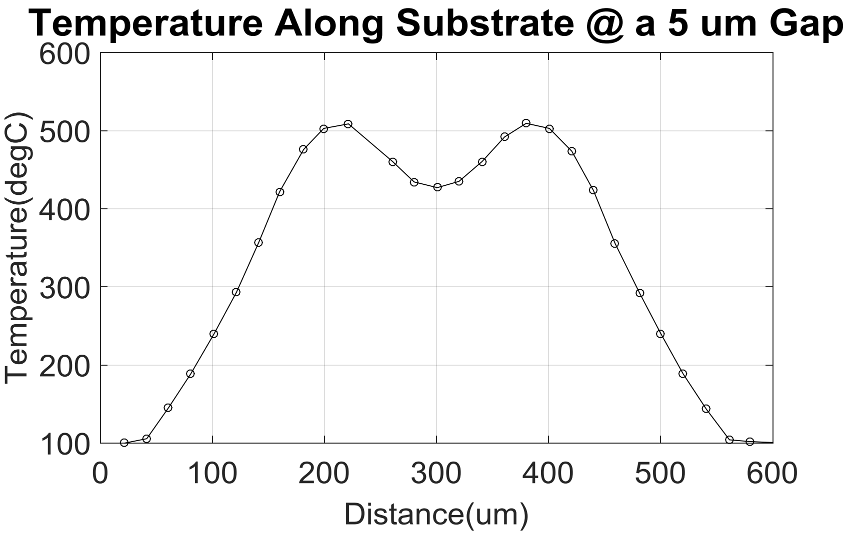

Figure 72-Heat Distribution of Microheater with a 5 um Airgap

From the results shown in Figure 72, two things can be determined. One, adequate heat can be supplied to sinter the materials upon close proximity operation between the heat source and the materials being sintered. Two, the selectivity of materials to be printed can be achieved.

5.4.4 Temperature Uniformity

To ensure the same quality of sintering throughout a print, the temperature must be as uniform as possible. Uniformity can be optimized by use of a particle swarm optimization algorithm. The design objective was to have a maximum temperature difference of 50ºC over the sample space. To optimize the uniformity, a sample space of 400 µm x 400 µm was used. The design parameters used were L and L_1 and the objective was to minimize the standard deviation of temperatures taken from 4000 evenly distributed points within the sample space. Figure 73 shows the sample space and design parameters to be solved.

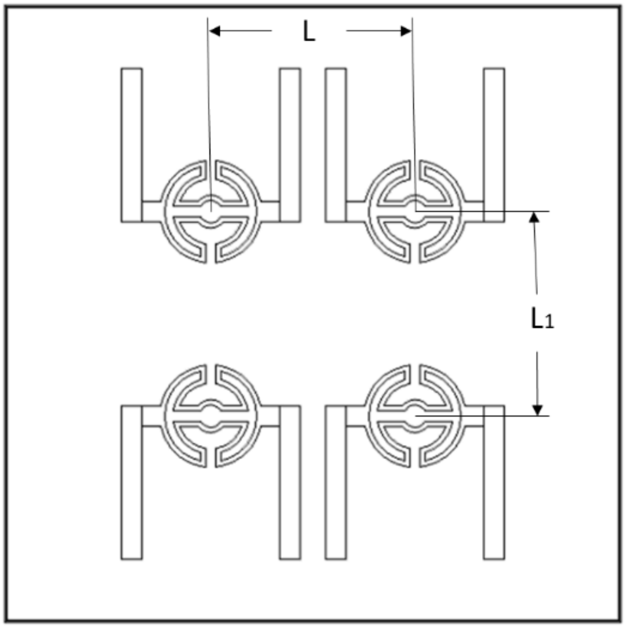

Figure 73-Design Space and Parameters for Optimization

The results of this optimization were not successful in achieving the intended objective. The optimal solution resulted in the heaters being too close together to print conductive leads in-between the heaters. As shown from Figure 72, this could have also been a trivial assumption when analyzation of the impact of membrane size on the distance the heat would transfer through the membrane to the substrate was made. The final temperature difference over the heaters was found by taking the standard deviation and the maximum and minimum temperature difference of the temperatures of the 4000 points. The results show a standard deviation of 89.1 ºC and a maximum temperature difference of 187 ºC from the final design used with 200 µm spacing from center to center of the microheaters. These results were found from a 5 µm airgap between the heater and substrate. A larger airgap leaves more opportunity for heat uniformity, but has a significant impact on the maximum achievable temperature as seen in Figure 70. These results show that more research is needed in improving the uniformity of temperature distribution on the printing substrate.

5.4.5 Structural Integrity

A MEMS microheater is subject to many structural integrity issues. The main structural focal point of this design is the suspended membrane and its resultant stresses and deflection from thermal expansion. The design must not exceed the yield strength of silicon nitride of ~430 MPa [131] in thin film PECVD silicon nitride. There must also not be enough displacement of the membrane that it could interfere with the print. Thermal stresses can result in up to 300MPa which can be calculated analytically from (7 and the corresponding material properties of Si_3N_4. Stress concentrations were found in this design near the center of the design of the drivewheels. This is likely due to the smaller geometry of the heaters in this section and heat concentration. This new design resulted in a .16 µm deflection downward in the direction of the substrate being printed on, which is not significant enough to impact the printing based on simulation results. The results of the stress and deflection are shown in Figure 74 and Figure 75. These numerical results were found using (8) through (17).

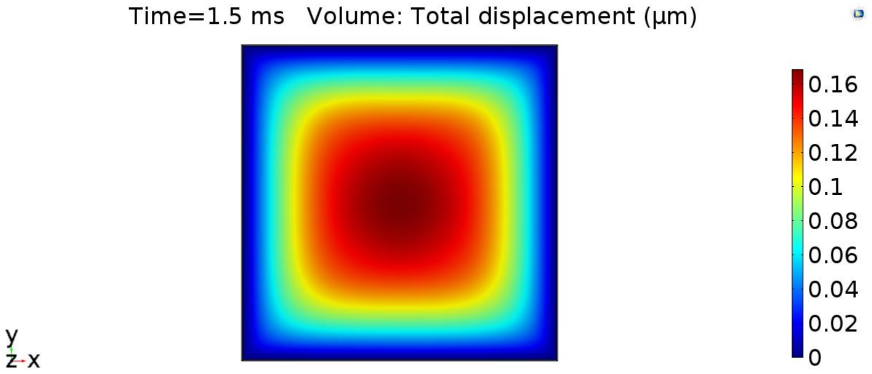

Figure 74-Total Displacement from Numerical Simulation

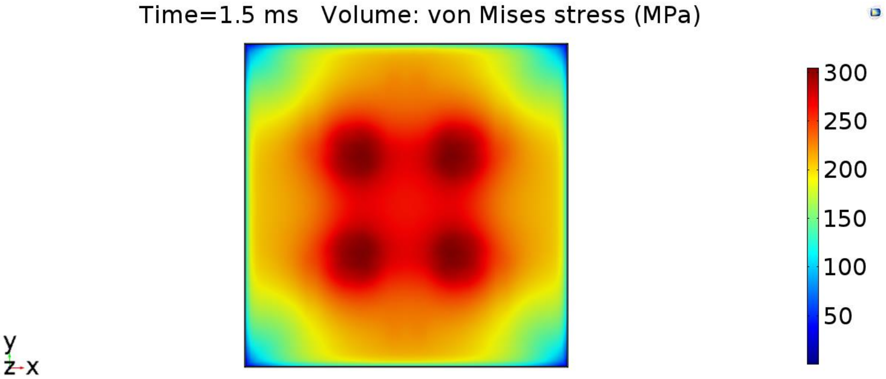

Figure 75-Stress in Silicon Nitride Membrane from Thermal Expansion

5.4.6 Proposed Fabrication of New Design

Fabrication has been proposed for the previous microheater design. This design can be fully fabricated in HiDEC by ordering silicon wafers with LPCVD silicon nitride to start fabrication. A list of the necessary steps are shown below:

1. Start with Silicon wafer (100) –
    a. 100mm P(100) 1-10 ohm-cm SSP 500um
    b. Two sides coated (Si_3N_4 3000 angstroms LPCVD 200MPa +/- 50 MPa tensile)
2. RCA cleans
3. Spin on HMDS to promote adhesion of resist to the wafer

4. Spin on photoresist 4110
   Speed: 2500 rpm
   Time: 30 seconds
   Ramp: 1000 rpm/s
5. Bake Photoresist
   Temp: 100C
   Time: 1 minute
6. Exposure using backside etch mask

   Energy= constant of material/thickness;

   Time(s) =energy/intensity

   Align Backside Etch mask with wafer flat

7. Develop

   Developer: AZ400K developer 1:3 DI water dilution

   Time: 1min immersion with mild agitation

8. Rinse wafer with DI water
9. Post bake-bake for 30 min at 120C

---

10. Reactive Ion Etch (RIE)

    Depth: 3000

    Etchant Gas: CF4/O2

    Rate: ~.1um/min

    Time: 3 min

11. Strip Resist
    Temp: 85C
    Solution: PRS1000
    Time: 10-20 min
12. followed with a dump rinse in DI water and spin rinse dry

---

13. KOH etch

    Rate: ~1.4um/min
    Temp: 85C with agitation
    Time: 6-8 hrs
14. Piranha clean and dry in oven for 5-10 min

---

15. Spin on Acetone to promote adhesion

    Speed: 500 rpm

    Time: 10s

16. Spin on photoresist 5214-E
    Speed: 4000 rpm (Spread: 1000 rpm)

Time: 30s (Spread: 10s)
Ramp: 1000 rpm/s

17. Exposure
    Mask: Heater mask aligns w/ backside etch
    Time: 6s
18. Bake
    Temp: 88C
    Time: 45s
19. Exposure
    Mask: none
    Time: 45s
20. Bake
    Temp: 106C
    Time: 45s
21. Develop- AZ 300 MIF
    Time: 1 min 30s immersion with mild agitation
22. Rinse-Rinse wafer with DI water
23. E-beam evaporation
    Material: Pt/Ti
    Thickness: 50 Angstroms Ti; 1500 Angstroms Pt
24. Lift off
    Material: Fully immerse in acetone until removed completely
25. Repeat Steps 15-24 with leads mask
26. PECVD
    Material: Silicon Nitride
    Thickness: 3500 Angstroms
27. 1hr-dice wafer into 16 microheater arrays

5.4.7 Summary of Model Based Design

This section provides modeling of a microheater which was designed specifically for the SRS system. The previously optimized heater geometry, was kept for this design, and focus was centered towards parameters such as material optimization of the heater to improve the heat transfer. As was shown in the modeling, temperatures on the particle surface of 200^0C up to 500^0C could be maintained with airgaps of 1 μm - 25 μm. Heating was provided solely during the ramp up for a duration time of 1.5 *ms*. The power consumed by this heater was significantly less, at 2 W of power. Overall, this design is better than the Ti microheater on the glass substrate design. To continue this work, a fabrication method has been proposed at the end of this chapter.

Chapter 6 CONCLUSIONS AND RECOMMENDATIONS FOR FUTURE WORK

6.1.1 Summary of Thesis

3D printing technology is a quickly evolving field of technological innovation. The technological development has been progressing rapidly in this field, but it doesn't compete with traditional mass manufacturing methods. 3D printing is still widely known for its ability to create low-volume customized products and prototypes. In this thesis, a novel method of printing, selective resistive sintering has been evaluated to show its feasibility based on numerical modeling and experimental validation. This was an innovative concept based on non-contact, millisecond sintering process using a MEMS microheater array as its heat source for rapid sintering.

Critical components of the SRS system were designed and prototyped for evaluation of this novel process. Based on previous research in the literature, a heater was successfully designed to ramp up to 600^0C in 1 *ms*. Optimization was performed on a single microheater geometry with objectives to minimize the non-uniformity of temperature distribution and the thermal stress respectively using a constrained particle swarm optimization algorithm. It was found that optimizations with respect to both objectives resulted in similar designs. This is because heat uniformity generally leads to smaller temperature gradient and thus lower thermal stress. From the results of the optimization for a single heater, the heaters were then placed into a 4-heater array. The array was prototyped to demonstrate the scalability of the microheater array.

To operate the microheater array, packaging and electrical connections were designed and prototyped. A printed circuit board offers a cheap solution for packaging of MEMS microheater array. In this design, one was chosen for the low resistance in connections, affordability, and ease of implementation. PCB design files were created in KiCad and then the design was sent out to be fabricated in two weeks by OSH Park, enabling the project to quickly continue. Electrical connections were designed for non-conventional fabrication methods. This fabrication was manually intensive, but for small production proved to be quick and affordable. Creating these leads showed some variation in the resistances. Conductive epoxies and wire bonding were used to connect the conductive leads of the microheater array to the PCB board. The conductive epoxy measured less than 1 Ω of resistance on test samples. Some of the microheater samples showed a large variation in electrical resistance, which was due to bad connections of wire bonds to the heater leads by the epoxy. Overall, three successful microheater packagings were created with 5 successful heaters. The microheaters were tested and evidences suggest temperature was able to reach over 600^{o}C.

The proof of concept proved to be an extensive part of the modeling. Multiple parameters define the operation of this new printing system. The temperatures were evaluated on the surface of the particles to show whether the materials would sinter during the few milliseconds of heating time. Two materials were used to prove the capabilities of sintering. The first was an Ag nano-particle paste and the second was Nylon 12 which reached adequate temperatures of 450^{o}C and 180^{o}C which would provide enough heat to either sinter the materials or melt the materials to form a solid object. Different parameters can be used in this system as previously mentioned. A few of those parameters were reviewed and characterized in this thesis. The overall heat flux, temperature gradient, initial temperature, and material properties have all been identified as significantly contributing factors to the feasibility of a print. Different parameters were modeled to show the improved printing system in this work. The printing system was successfully improved from a max temperature of 27^{o}C with a 5 µm airgap to 422^{o}C by changing 4 different parameters evaluated in cases 1-4 in section 4.1.4 to test the overall concept of selective resistive sintering, a high precision linear motion system and sensor were designed to be able to locate the printing substrate and accurately position the microheater within 500 *nm* of the printing substrate. The system was combined with the circuitry and heating system that had been previously tested, to test whether heat could be conducted through a medium to the particles. Thermal tape and photoresist 4110 were used in the preliminary experimentation, but the results were inconclusive. It appears there may not have been accurate enough control of the airgap through which the heat was conducted. Future research is needed.

In Chapter 5, a new microheater design was proposed to overcome some recognized issues with the previous microheater design. In this new design, the initial geometry of the optimized resistive element was kept due to its ability to maintain uniform heating. A glass substrate which was previously used for design was switched to a silicon substrate. Silicon enables a vast amount of fabrication techniques to enable unique designs. A suspended membrane was used as the microheater base for better insulation and power savings. This design was improved so that the thermal response time improved to 1.5 *ms*. The heat could be conducted to the particles to be sintered on the initial ramp up instead of the heater having to be maintained for several milliseconds. The power consumption was reduced in this design to 2 W, and temperatures of slightly greater than 500^{o}C could be achieved at airgaps of 1 µm. This new design was found to have significant improvements over the previous design.

6.1.2 Evaluation of Hypothesis

The main hypothesis of this work was that 1 *ms* sintering could occur with a 600 ˚C microheater. This method was only partially proven numerically and lacks experimental validation. A microheater capable of ramping up to 600 ˚C in 1 *ms* was successfully designed and optimized. It was tested up to 600 ˚C, but the thermal response time has not been experimentally validated.

Temperatures adequate to provide millisecond sintering of materials modeled in this thesis were partially proven numerically. The 1 *ms* ramp time was shown capable, but the heat could not reach the substrate being printed on from just the ramp up. In this study, the heat was maintained for 10 *ms* at 600 ˚C. This provided adequate heating to reach the substrate so that the process could be proven valid based on a surface temperature measurement. A new design was created which enabled 1.5 *ms* of total thermal response time. In this design, the operational parameters were significantly improved but could not achieve the thermal response of 1 *ms* desired in this paper.

6.1.3 Contributions

Much work has been put into improving the speeds of 3D printing while remaining an economical option of manufacturing. Though much research has been done, there has not been wide spread adoption of 3D printing as a viable manufacturing method for mass production. This thesis strives to help progress this larger vision. To accomplish the task, a novel SRS 3D printing method was proposed. To evaluate this new method, a microheater array, serving as the printhead of the SRS method, was designed, optimized, fabricated, packaged, and tested. In addition, another critical component, i.e., the Z-stage for precision airgap control, was designed and prototyped. Although an experimental proof of concept was not successful, numerical simulations have been performed to evaluate the SRS printing process and different printing parameters, which shows the SRS to be a viable printing method. In comparison to existing SLS method, the new method was shown that it could be potentially at least 10x better than SLS in terms of power consumption, cost, and speed.

6.1.4 Future Work Recommendations

Much work is still to be continued on this project. Control systems which can accurately provide heat in the thermal response desired is required. A rastering system which can CNC navigate the surface of a substrate through all three axes is required to prove it can be an actual 3D printing system.

The heater used in this research is adequate for proof of concept, but it still needs to be improved. Higher temperature operations of 1000C have been shown possible in SnO_2:Sb heaters [21]. A new higher temperature heater needs to be used in this printing process to have more control over the heating process. This can also reduce thermal response time and enables higher temperature to sinter the materials which are an interrelated behavior. The overall geometry of the heater needs to be redesigned for close proximity operations with more geometric freedom. Fabrication was limited in this experiment by equipment available by HiDEC. It is recommended that a packaging and external lead device be created from thin film manufacturing that can enable micron or nano meter tolerances. This could also be accomplished by using backside connections from through vias provided by DRIE.

The heater needs to be optimized for operations in a large scale array. The heaters need to be used to provide uniform heating that can be controlled digitally. The entire digitalization of the heating array is one area of research that needs to be investigated.

6.1.5 Closing Remarks

Creating a completely new printing system involves numerous aspects of pushing technological limits and unique implementations of existing engineering principles. The characterizing physics in the system have been well defined, with the exception of the sintering process. The inability to efficiently prove sintering could occur at the speeds is the primary concern for the feasibility of this new method. Sintering by use of a MEMS microheater is an efficient method of printing if proven viable. This could possibly enable greater adoption of sintering technology for consumers as well as being applicable to mass production manufacturing. There are many aspects of the printing system which have been evaluated numerically, but there are still many obstacles to achieving the large impact that the new printing system could have. This solution is an innovation due to the application of existing technology. In these efforts, foundation and innovation have been paved for a promising technology.

References

[1] I. ASTM, "ASTM52915-13, Standard specification for additive manufacturing file format (AMF) Version 1.1," *ASTM International, West Conshohocken, PA,* 2013.

[2] (). *iota Sigma*. Available: http://www.iotasigma.co.uk/sls.html.

[3] M. Baumers, C. Tuck and R. Hague, "SELECTIVE HEAT SINTERING VERSUS LASER SINTERING: COMPARISON OF DEPOSITION RATE, PROCESS ENERGY CONSUMPTION AND COST PERFORMANCE," .

[4] G. Marshall, W. Young II, N. Shamsaei, J. Craig, T. Wakeman and S. Thompson, "DUAL THERMOGRAPHIC MONITORING OF Ti-6AL-4V CYLINDERS DURING DIRECT LASER DEPOSITION," .

[5] (). *Image-Based Quality Indices of Aerosol Jet Printed Conductive Lines*. Available: https://www.researchgate.net/publication/276847866_Image-Based_Quality_Indices_of_Aerosol_Jet_Printed_Conductive_Lines.

[6] A. Mette, P. Richter, M. Hörteis and S. Glunz, "Metal aerosol jet printing for solar cell metallization," *Prog Photovoltaics Res Appl,* vol. 15, pp. 621-627, 2007.

[7] (). *AEROSOL JET 200 SERIES SYSTEMS* [Printed Electronics Exploration and Development]. Available: http://www.optomec.com/wp-content/uploads/2014/08/AJ_200_WEB_0216.pdf.

[8] (2/2/2016). *AEROSOL JET 5X SYSTEM* [For 3D Printed Electronics Applications]. Available: http://www.optomec.com/wp-content/uploads/2014/08/AJ5X-System-WEB-0216.pdf.

[9] (). *Blue Printer Brochure*. Available: http://blueprinter-powder-3dprinter.co.uk/sites/default/files/BluePrinter_maj_2015_tryk_pages.pdf.

[10] P. Thiel and B. Masters, *Zero to One.* Crown Business, Sept. 16, 2014.

[11] (). *MEMS Packaging*. Available: http://www.seas.upenn.edu/~meam550/PackagingJPL.pdf.

[12] K. K. Tan, T. H. Lee and S. Huang, *Precision Motion Control: Design and Implementation.* Springer Science & Business Media, 2007.

[13] R. Mistler and R. Coble, "Grain-boundary diffusion and boundary widths in metals and ceramics," *J. Appl. Phys.,* vol. 45, pp. 1507-1509, 1974.

[14] (). *James Prescoot Joule* [James Prescott Joule]. Available: http://www.sciencemuseum.org.uk/onlinestuff/people/james%20prescott%20joule.aspx.

[15] L. Setti, C. Piana, S. Bonazzi, B. Ballarin, D. Frascaro, A. Fraleoni-Morgera and S. Giuliani, "Thermal inkjet technology for the microdeposition of biological molecules as a viable route for the realization of biosensors," *Anal. Lett.*, vol. 37, pp. 1559-1570, 2004.

[16] K. Zhang, S. Chou and S. Ang, "Fabrication, modeling and testing of a thin film Au/Ti microheater," *International Journal of Thermal Sciences,* vol. 46, pp. 580-588, 2007.

[17] (). *Timeline of Our History* [HP Timeline]. Available: http://www8.hp.com/us/en/hp-information/about-hp/history/hp-timeline/timeline.html.

[18] X. Cui and T. Boland, "Human microvasculature fabrication using thermal inkjet printing technology," *Biomaterials,* vol. 30, pp. 6221-6227, 2009.

[19] T. Mendum, E. Stoler, H. VanBenschoten and J. C. Warner, "Concentration of bisphenol A in thermal paper," *Green Chemistry Letters and Reviews,* vol. 4, pp. 81-86, 2011.

[20] J. Creemer, D. Briand, H. Zandbergen, W. Van der Vlist, C. de Boer, N. F. de Rooij and P. Sarro, "Microhotplates with TiN heaters," *Sensors and Actuators A: Physical,* vol. 148, pp. 416-421, 2008.

[21] J. Spannhake, A. Helwig, G. Müller, G. Faglia, G. Sberveglieri, T. Doll, T. Wassner and M. Eickhoff, "SnO 2: Sb–A new material for high-temperature MEMS heater applications: Performance and limitations," *Sensors Actuators B: Chem.,* vol. 124, pp. 421-428, 2007.

[22] S. Toskov, R. Glatz, G. Miskovic and G. Radosavljevic, "Modeling and fabrication of pt micro-heaters built on alumina substrate," in *Electronics Technology (ISSE), 2013 36th International Spring Seminar On,* 2013, pp. 47-52.

[23] R. M. Tiggelaar, "Silicon-technology based microreactors for high-temperature heterogeneous partial oxidation reactions," 2004.

[24] (). *ASM Material Data Sheet*. Available: http://asm.matweb.com/search/SpecificMaterial.asp?bassnum=MQ304A.

[25] O. Sidek, M. Ishak, M. Khalid, M. A. Bakar and M. Miskam, "Effect of heater geometry on the high temperature distribution on a MEMS micro-hotplate," in *Quality Electronic Design (ASQED), 2011 3rd Asia Symposium On,* 2011, pp. 100-104.

[26] (). *Silicon Carbide, SiC Ceramic Properties*. Available: http://accuratus.com/silicar.html.

[27] (). *DuPont GreenTape
-Low Temperature Co-fired Ceramic System*. Available: http://www.dupont.com/content/dam/dupont/products-and-services/electronic-and-electrical-materials/documents/prodlib/GreenTape_Design_Layout_Guidelines.pdf.

[28] T. Maeder, L. Sagalowicz and P. Muralt, "Stabilized platinum electrodes for ferroelectric film deposition using Ti, Ta and Zr adhesion layers," *Japanese Journal of Applied Physics,* vol. 37, pp. 2007-2012, 1998.

[29] D. Bradley and A. Entwistle, "Determination of the emissivity, for total radiation, of small diameter Platinum-10% Rhodium wires in the temperature range 600-1450 C," *British Journal of Applied Physics,* vol. 12, pp. 708, 1961.

[30] S. Z. Ali, F. Udrea, W. I. Milne and J. W. Gardner, "Tungsten-based SOI microhotplates for smart gas sensors," *Microelectromechanical Systems, Journal Of,* vol. 17, pp. 1408-1417, 2008.

[31] G. Gordillo, F. Mesa and C. Calderón, "Electrical and morphological properties of low resistivity Mo thin films prepared by magnetron sputtering," *Brazilian Journal of Physics,* vol. 36, pp. 982-985, 2006.

[32] L. Mele, F. Santagata, E. Iervolino, M. Mihailovic, T. Rossi, A. Tran, H. Schellevis, J. Creemer and P. Sarro, "A molybdenum MEMS microhotplate for high-temperature operation," *Sensors and Actuators A: Physical,* vol. 188, pp. 173-180, 2012.

[33] F. Lacy, "Investigating thin films for use as temperature sensors," in *Proceedings of the World Congress on Engineering & Computer Science: October 24-26,* 2007, pp. 441-444.

[34] S. Lee, D. Dyer and J. Gardner, "Design and optimisation of a high-temperature silicon micro-hotplate for nanoporous palladium pellistors," *Microelectron. J.,* vol. 34, pp. 115-126, 2003.

[35] F. Trigui, E. Velu and C. Dupas, "Fuchs-Sondheimer theory as explanation of the magnetoresistance effects in multilayers Au/Co," *J Magn Magn Mater,* vol. 93, pp. 421-424, 1991.

[36] K. L. Chopra, "Thin film phenomena," 1969.

[37] R. B. Belser and W. H. Hicklin, "Temperature coefficients of resistance of metallic films in the temperature range 25 to 600 C," *J. Appl. Phys.,* vol. 30, pp. 313-322, 1959.

[38] (July 30, 2013). *Platinum (PT) - Properties, Applications*. Available: http://www.azom.com/article.aspx?ArticleID=9235.

[39] (). *Material: Tinanium Nitride (bulk)*. Available: https://www.memsnet.org/material/titaniumnitridetinbulk/.

[40] (). *ASM Aerospae Specification Metals Inc.* Available: http://asm.matweb.com/search/SpecificMaterial.asp?bassnum=MTP641.

[41] (). *Tin Oxide (SnO2) Nanoparticles-Properties Applications*. Available: http://www.azonano.com/article.aspx?ArticleID=3381.

[42] (). *Midwest Tungsten Service*. Available: http://www.tungsten.com/materials/tungsten/.

[43] F. Hochberg, H. K. Seitz and A. V. Brown, "A thin-film integrated incandescent display," *Electron Devices, IEEE Transactions On,* vol. 20, pp. 1002-1005, 1973.

[44] (). *Molybdenum - Mechanical Properties and Material Application

 .* Available: http://www.azom.com/article.aspx?ArticleID=7637.

[45] Y. Zhao, L. Wang and T. Yu, "Mechanics of adhesion in MEMS—a review," *J. Adhes. Sci. Technol.,* vol. 17, pp. 519-546, 2003.

[46] R. Srinivasan, I. Hsing, P. E. Berger, K. F. Jensen, S. L. Firebaugh, M. A. Schmidt, M. P. Harold, J. J. Lerou and J. F. Ryley, "Micromachined reactors for catalytic partial oxidation reactions," *AIChE J.,* vol. 43, pp. 3059-3069, 1997.

[47] G. Bernhardt, C. Silvestre, N. LeCursi, S. Moulzolf, D. Frankel and R. Lad, "Performance of Zr and Ti adhesion layers for bonding of platinum metallization to sapphire substrates," *Sensors Actuators B: Chem.,* vol. 77, pp. 368-374, 2001.

[48] X. Zhang and C. P. Grigoropoulos, "Thermal conductivity and diffusivity of free-standing silicon nitride thin films," *Rev. Sci. Instrum.,* vol. 66, pp. 1115-1120, 1995.

[49] N. Sabaté, I. Gracia, J. Santander, L. Fonseca, E. Figueras, C. Cane and J. Morante, "Mechanical characterization of thermal flow sensors membranes," *Sensors and Actuators A: Physical,* vol. 125, pp. 260-266, 2006.

[50] C. Rossi, P. Temple-Boyer and D. Estève, "Realization and performance of thin SiO 2/SiN x membrane for microheater applications," *Sensors and Actuators A: Physical,* vol. 64, pp. 241-245, 1998.

[51] K. Zhang, C. Rossi, M. Petrantoni and N. Mauran, "A nano initiator realized by integrating Al/CuO-based nanoenergetic materials with a Au/Pt/Cr microheater," *Microelectromechanical Systems, Journal Of,* vol. 17, pp. 832-836, 2008.

[52] J. W. Judy, "Microelectromechanical systems (MEMS): fabrication, design and applications," *Smart Mater. Struct.,* vol. 10, pp. 1115, 2001.

[53] A. Stoffel, A. Kovacs, W. Kronast and B. Müller, "LPCVD against PECVD for micromechanical applications," *J Micromech Microengineering,* vol. 6, pp. 1, 1996.

[54] G. Kotzar, M. Freas, P. Abel, A. Fleischman, S. Roy, C. Zorman, J. M. Moran and J. Melzak, "Evaluation of MEMS materials of construction for implantable medical devices," *Biomaterials,* vol. 23, pp. 2737-2750, 2002.

[55] A. Tarraf, J. Daleiden, S. Irmer, D. Prasai and H. Hillmer, "Stress investigation of PECVD dielectric layers for advanced optical MEMS," *J Micromech Microengineering,* vol. 14, pp. 317, 2003.

[56] R. L. Puurunen, J. Saarilahti and H. Kattelus, "Implementing ALD layers in MEMS processing," *ECS Transactions,* vol. 11, pp. 3-14, 2007.

[57] K. Mackenzie, D. Johnson, M. DeVre, R. Westerman and B. Reelfs, "Stress control of si-based PECVD dielectrics," in *Proceedings of the 207th Electrochemical Society Meeting,* 2005, pp. 148-159.

[58] H. Huang, K. Winchester, A. Suvorova, B. Lawn, Y. Liu, X. Hu, J. Dell and L. Faraone, "Effect of deposition conditions on mechanical properties of low-temperature PECVD silicon nitride films," *Materials Science and Engineering: A,* vol. 435, pp. 453-459, 2006.

[59] G. Velmathi, N. Ramshanker and S. Mohan, "Design, electro-thermal simulation and geometrical optimization of double spiral shaped microheater on a suspended membrane for gas sensing," in *IECON 2010-36th Annual Conference on IEEE Industrial Electronics Society,* 2010, pp. 1258-1262.

[60] J. Kuntner, A. Jachimowicz, F. Kohl and B. Jakoby, *Determining the Thin-Film Thermal Conductivity of Low Temperature PECVD Silicon Nitride.* na, 2006.

[61] (). *LPCVD silicon dioxide material database*. Available: http://www.mit.edu/~6.777/matprops/lpcvd_sio2.htm.

[62] (). *Silicon Dioxide Properties*. Available: http://www.iue.tuwien.ac.at/phd/filipovic/node26.html.

[63] S. D. Senturia, *Microsystem Design.* Springer Science & Business Media, 2007.

[64] A. Pike and J. W. Gardner, "Thermal modelling and characterisation of micropower chemoresistive silicon sensors," *Sensors Actuators B: Chem.,* vol. 45, pp. 19-26, 1997.

[65] B. Kantha and S. K. Sarkar, "Comparative Study of Particle Swarm Optimization and Genetic Algorithm for the Optimization of System Parameters of MEMS Based Micro-Heater," *Journal of Computational and Theoretical Nanoscience,* vol. 12, pp. 1641-1646, 2015.

[66] S. Joy and J. K. Antony, "Design and simulation of a micro hotplate using COMSOL multiphysics for MEMS based gas sensor," in *2015 Fifth International Conference on Advances in Computing and Communications (ICACC),* 2015, pp. 465-468.

[67] S. Astie, A. Gue, E. Scheid, L. Lescouzeres and A. Cassagnes, "Optimization of an integrated SnO 2 gas sensor using a FEM simulator," *Sensors and Actuators A: Physical,* vol. 69, pp. 205-211, 1998.

[68] T. Neda, K. Nakamura and T. Takumi, "A polysilicon flow sensor for gas flow meters," *Sensors and Actuators A: Physical,* vol. 54, pp. 626-631, 1996.

[69] U. Dibbern, "A substrate for thin-film gas sensors in microelectronic technology," *Sensors Actuators B: Chem.,* vol. 2, pp. 63-70, 1990.

[70] Y. Mo, Y. Okawa, K. Inoue and K. Natukawa, "Low-voltage and low-power optimization of micro-heater and its on-chip drive circuitry for gas sensor array," *Sensors and Actuators A: Physical,* vol. 100, pp. 94-101, 2002.

[71] (). *MEMS Fabrication I : Process Flows and Bulk Micromachining*. Available: http://www-bsac.eecs.berkeley.edu/projects/ee245/Lectures/lecturepdfs/Lecture2.BulkMicromachining.pdf.

[72] Y. Mo, Y. Okawa, K. Inoue and K. Natukawa, "Low-voltage and low-power optimization of micro-heater and its on-chip drive circuitry for gas sensor array," *Sensors and Actuators A: Physical,* vol. 100, pp. 94-101, 2002.

[73] S. B. Crary, "Thermal management of integrated microsensors," *Sensors and Actuators,* vol. 12, pp. 303-312, 1987.

[74] K. Westra, "KOH and TMAH Etching of Bulk Silicon," February 10, 2010.

[75] P. Pal and K. Sato, "Fabrication methods based on wet etching process for the realization of silicon MEMS structures with new shapes," *Microsystem Technologies,* vol. 16, pp. 1165-1174, 2010.

[76] M. J. Madou, *Fundamentals of Microfabrication: The Science of Miniaturization.* CRC press, 2002.

[77] B. D. Gates, Q. Xu, M. Stewart, D. Ryan, C. G. Willson and G. M. Whitesides, "New approaches to nanofabrication: molding, printing, and other techniques," *Chem. Rev.,* vol. 105, pp. 1171-1196, 2005.

[78] M. Esashi, "Wafer level packaging of MEMS," *J Micromech Microengineering,* vol. 18, pp. 073001, 2008.

[79] H. Reichl and V. Grosser, "Overview and development trends in the field of MEMS packaging," in *Micro Electro Mechanical Systems, 2001. MEMS 2001. the 14th IEEE International Conference On,* 2001, pp. 1-5.

[80] (). *Micro Heater-NMH200*. Available: http://nanosniff.com/products/mems-sensors/micro-heater-nmh200/.

[81] J. Köhler, K. Jonsson, M. Jönsson, L. Stenmark and Y. Bäcklund, "Space qualification of direct bonded silicon microsystems," in *Micro Nano Technology for Space Applications, Pasadena, CA, USA,* 2000, .

[82] J. Connelly, A. Kourepenis, D. Larsen and T. Marinis, "Inertial MEMS Development for Space," *The,* vol. 2, pp. 11-15, 1999.

[83] N. Maluf and K. Williams, *Introduction to Microelectromechanical Systems Engineering.* Artech House, 2004.

[84] J. Kita, A. Dziedzic, L. J. Golonka and A. Bochenek, "Properties of laser cut LTCC heaters," *Microelectronics Reliability,* vol. 40, pp. 1005-1010, 2000.

[85] M. Heckele and W. Schomburg, "Review on micro molding of thermoplastic polymers," *J Micromech Microengineering,* vol. 14, pp. R1, 2003.

[86] D. J. Hayes, W. R. Cox and D. B. Wallace, "Printing systems for MEMS packaging," in *Micromachining and Microfabrication,* 2001, pp. 206-214.

[87] R. Ramesham and R. Ghaffarian, "Challenges in interconnection and packaging of microelectromechanical systems (MEMS)," in *Electronic Components & Technology Conference, 2000. 2000 Proceedings. 50th,* 2000, pp. 666-675.

[88] S. B. Fuller, E. J. Wilhelm and J. M. Jacobson, "Ink-jet printed nanoparticle microelectromechanical systems," *Microelectromechanical Systems, Journal Of,* vol. 11, pp. 54-60, 2002.

[89] S. Glod, D. Poulikakos, Z. Zhao and G. Yadigaroglu, "An investigation of microscale explosive vaporization of water on an ultrathin Pt wire," *Int. J. Heat Mass Transfer,* vol. 45, pp. 367-379, 2002.

[90] S. D. Senturia, "Packaging, testing, and calibration," in *Microsystem Design,* 6th ed.Anonymous Norwell, Massachusetts: Kluwer Academic Publishers, 2001, pp. 454.

[91] C. B. O'Neal, A. P. Malshe, S. B. Singh, W. Brown and W. P. Eaton, "Challenges in the packaging of MEMS," in *Advanced Packaging Materials: Processes, Properties and Interfaces, 1999. Proceedings. International Symposium On,* 1999, pp. 41-47.

[92] H. Chuang and S. Wereley, "Design, fabrication and characterization of a conducting PDMS for microheaters and temperature sensors," *J Micromech Microengineering,* vol. 19, pp. 045010, 2009.

[93] W. Sripumkhai, A. Lekwichai, W. Bunjongpru, S. Porntheeraphat, B. Tunhoo, E. Ratanaudomphisut, T. Kamsri, C. Hruanun, A. Poyai and J. Nukeaw, "On-chip platinum micro-heater with platinum temperature sensor for A fully integrated disposable PCR module," in *Advanced Materials Research,* 2010, pp. 129-132.

[94] W. Dong, J. Tang and Y. ElDeeb, "Design of a linear-motion dual-stage actuation system for precision control," *Smart Mater. Struct.,* vol. 18, pp. 095035, 2009.

[95] J. Tzen, S. Jeng and W. Chieng, "Modeling of piezoelectric actuator for compensation and controller design," *Precis Eng,* vol. 27, pp. 70-86, 2003.

[96] P. Ouyang, R. Tjiptoprodjo, W. Zhang and G. Yang, "Micro-motion devices technology: The state of arts review," *The International Journal of Advanced Manufacturing Technology,* vol. 38, pp. 463-478, 2008.

[97] H. J. Adriaens, W. L. De Koning and R. Banning, "Modeling piezoelectric actuators," *Mechatronics, IEEE/ASME Transactions On,* vol. 5, pp. 331-341, 2000.

[98] (). *Eppendorf Corp.* Available: https://www.eppendorf.com/US-en/.

[99] N. Nguyen, S. Ho and C. L. Low, "A polymeric microgripper with integrated thermal actuators," *J Micromech Microengineering,* vol. 14, pp. 969, 2004.

[100] C. Ku, Y. Tan and S. Panda, "High-precision position control of linear permanent magnet bldc servo motor for pick and place application," in *Industrial Technology, 2006. ICIT 2006. IEEE International Conference On,* 2006, pp. 2919-2924.

[101] (). *Linear Motor Basics*. Available: http://www.parkermotion.com/whitepages/linearmotorarticle.pdf.

[102] A. J. Fleming, "A review of nanometer resolution position sensors: operation and performance," *Sensors and Actuators A: Physical,* vol. 190, pp. 106-126, 2013.

[103] J. Sirohi and I. Chopra, "Fundamental understanding of piezoelectric strain sensors," *J Intell Mater Syst Struct,* vol. 11, pp. 246-257, 2000.

[104] S. Devasia, E. Eleftheriou and S. R. Moheimani, "A survey of control issues in nanopositioning," *Control Systems Technology, IEEE Transactions On,* vol. 15, pp. 802-823, 2007.

[105] S. Fericean and R. Droxler, "New noncontacting inductive analog proximity and inductive linear displacement sensors for industrial automation," *Sensors Journal, IEEE,* vol. 7, pp. 1538-1545, 2007.

[106] S. D. Roach, "Designing and building an eddy current position sensor," *Sensors-the Journal of Applied Sensing Technology,* vol. 15, pp. 56-74, 1998.

[107] K. Ara, "A differential transformer with temperature-and excitation-independent output," *Instrumentation and Measurement, IEEE Transactions On,* vol. 21, pp. 249-255, 1972.

[108] M. Amann, T. Bosch, M. Lescure, R. Myllyla and M. Rioux, "Laser ranging: a critical review of usual techniques for distance measurement," *Optical Engineering,* vol. 40, pp. 10-19, 2001.

[109] P. Hariharan, *Basics of Interferometry.* Academic Press, 2010.

[110] J. R. Groza, "Nanosintering," *Nanostructured Materials*, vol. 12, pp. 987-992, 1999.

[111] (). *Innovative Technologies Conductive and Resistive Inks*. Available: http://www.methode.com/sensors-and-switches/conductive-and-resistive-inks.html#.V2wjwPkrKUk.

[112] K. Moon, H. Dong, R. Maric, S. Pothukuchi, A. Hunt, Y. Li and C. Wong, "Thermal behavior of silver nanoparticles for low-temperature interconnect applications," *J Electron Mater*, vol. 34, pp. 168-175, 2005.

[113] S. Farnsworth and K. Schroder, "Photonic curing for millisecond-drying of thin films," *Specialist Printing Worldwide*, vol. 3436, 2012.

[114] K. A. Schroder, "Mechanisms of Photonic Curing™: Processing High Temperature Films on Low Temperature Substrates," *Nanotech; CRC Press: Boca Raton, FL, USA,* vol. 2, pp. 220-223, 2011.

[115] Martin J. Guillot, Kurt A. Schroder and Steve. C. McCool, "SIMULATING THE THERMAL RESPONSE OF THIN FILMS DURING PHOTONIC CURING," *ASME,* IMECE2012-87674, 2013.

[116] L. Ma, J. Fong, B. Lane, S. Moylan, J. Filliben, A. Heckert and L. Levine, "Using design of experiments in finite element modeling to identify critical variables for laser powder bed fusion," in *International Solid Freeform Fabrication Symposium*, 2015, .

[117] P. Zehner and E. U. Schlünder, "Die effektive Wärmeleitfähigkeit durchströmter Kugelschüttungen bei mäßigen und hohen Temperaturen," *Chemie Ingenieur Technik,* vol. 45, pp. 272-276, 1973.

[118] S. S. Sib, J. W. Barlow and T. Austin, "MEASUREMENT AND PREDICTION OF THE THERMAL CONDUCTIVITY OF POWDERS ATIDOHTEMPERATURES," .

[119] S. Chol, "Enhancing thermal conductivity of fluids with nanoparticles," *ASME-Publications-Fed,* vol. 231, pp. 99-106, 1995.

[120] M. R. Alkahari, T. Furumoto, T. Ueda, A. Hosokawa, R. Tanaka, A. Aziz and M. Sanusi, "Thermal conductivity of metal powder and consolidated material fabricated via selective laser melting," in *Key Engineering Materials,* 2012, pp. 244-249.

[121] R. C. Eberhart and J. Kennedy, "A new optimizer using particle swarm theory," in *Proceedings of the Sixth International Symposium on Micro Machine and Human Science,* 1995, pp. 39-43.

[122] R. Poli, "An analysis of publications on particle swarm optimization applications," 2007.

[123] G. Venter and J. Sobieszczanski-Sobieski, "Particle swarm optimization," *AIAA J.*, vol. 41, pp. 1583-1589, 2003.

[124] I. C. Trelea, "The particle swarm optimization algorithm: convergence analysis and parameter selection," *Information Processing Letters,* vol. 85, pp. 317-325, 2003.

[125] M. J. Guillot, S. C. McCool and K. A. Schroder, "Simulating the thermal response of thin films during photonic curing," in *ASME 2012 International Mechanical Engineering Congress and Exposition,* 2012, pp. 19-27.

[126] H. Zarringhalam, N. Hopkinson, N. Kamperman and J. De Vlieger, "Effects of processing on microstructure and properties of SLS Nylon 12," *Materials Science and Engineering: A,* vol. 435, pp. 172-180, 2006.

[127] (). *ProMaker P1000 Preliminary Specifiications* . Available: http://www.prodways.com/en/printer/promaker-p1000/.

[128] J. Kuntner, A. Jachimowicz, F. Kohl and B. Jakoby, *Determining the Thin-Film Thermal Conductivity of Low Temperature PECVD Silicon Nitride.* na, 2006.

[129] U. Dibbern, "A substrate for thin-film gas sensors in microelectronic technology," *Sensors Actuators B: Chem.*, vol. 2, pp. 63-70, 1990.

[130] T. Neda, K. Nakamura and T. Takumi, "A polysilicon flow sensor for gas flow meters," *Sensors and Actuators A: Physical,* vol. 54, pp. 626-631, 1996.

[131] H. Liu and S. M. Hsu, "Fracture behavior of multilayer silicon nitride/boron nitride ceramics," *J Am Ceram Soc,* vol. 79, pp. 2452-2457, 1996.